INVESTIGATION OF FIBER-REINFORCED CONCRETE CRACK WIDTH MEASUREMENT BY FINITE ELEMENT METHOD

by

SINA ABHAEE

Presented to the Faculty of the Graduate School of

The University of Texas at Arlington in Partial Fulfillment

of the Requirements

for the Degree of

MASTER OF SCIENCE IN CIVIL ENGINEERING

THE UNIVERSITY OF TEXAS AT ARLINGTON

December 2016

Acknowledgements

I would like to express my sincerest gratitude to my advisor, Dr. Ali Abolmaali for his continuous support, guidance and trust throughout my Master of Science studies. In addition, I would like to give my warm appreciation to my thesis committee members, Dr. Mohsen Shahandashti and Dr. Raad Azzawi for their insightful comments and advices.

I would like to give special thanks to all my friends and colleague in the Center for Structural Engineering Research/Simulation (CSERS) group who offered me their help and support throughout my research.

Last but not least, I would like to thank my family for their unconditional and continues love and support at every stage of my life.

December 20, 2016

Abstract

INVESTIGATION OF FIBER-REINFORCED CONCRETE

CRACK WIDTH MEASUREMENT BY

FINITE ELEMENT METHOD

SINA ABHAEE, MS

The University of Texas at Arlington, 2016

Supervising Professor: Ali Abolmaali

This study presents numerical and experimental investigations of crack width measurement of the dry-cast synthetic fiber reinforced concrete (FRC). Notched and un-notched beams for two fiber volume fractions were tested under flexural loading based on the recommendations of RILEM TC 162-TDF and ASTM C1609. The crack profile in terms of crack propagation and crack width, was assessed, using the two-dimensional digital image correlation (2D DIC) technique. Images of the specimen's surface were captured during the test, and, surface deformation field was obtained by means of 2D DIC analysis.

The nonlinear, 3D finite element method (FEM) modeling of the flexural tests was performed, using a concrete damage plasticity (CDP) model for concrete. An indirect numerical method was utilized to obtain the tensile softening behavior of the synthetic FRC. The post-cracking stress-crack width relationship was obtained using the CDP model and a numerical inverse analysis

procedure. For this purpose, a piecewise function for the stress-crack width relationship was assumed to simulate the tensile softening behavior of the synthetic FRC. Experimental load–deflection curves were fitted through a numerical fitting procedure and post-crack tensile softening was obtained.

Numerical load-crack width responses were calculated and compared with experimental curves. Finally, the average fracture energy was calculated based on the obtained softening laws. Comparison of experimental data and numerical results suggest that the addition of synthetic fibers to the dry-cast concrete mixture increases the ductility, fracture energy and post-cracking strength of the concrete and provide crack width control. Integration of the tensile softening law and the CDP model can simulate the flexural behavior of the synthetic FRC. In addition, the numerical result can also provide the crack width data.

Table of Contents

Table of Figures

1 Introduction

1.1 Overview

Fiber reinforcement for cementitious material has become a source of great interest for researchers and the concrete industry. Extensive research has proved that it is possible to significantly improve the concrete material property by adding fibers into the matrix [1], [2] . Typically, fiber reinforced concrete (FRC) members demonstrate more ductile post-cracking behavior than normal concrete and provide a residual capacity after initiation of the first cracks. A decrease in the crack width, which results in enhancing the structural strength; freeze and thaw resistance; and impact resistance are other advantages of FRC members.

Fibers are typically short, closely spaced, and randomly distributed throughout the concrete mix. Uniform distribution of fibers is in contrast to the conventional reinforcement, which is used only in the required areas. Since concrete is strong in compression but fairly weak in tension, uniform distribution of fibers helps to increase the tensile strength of the whole section.

Fibers for use in the FRC members are made of different materials and geometry. Steel fibers are the most commonly used fiber materials; their extensive tensile strength makes them an effective material for use as fiber reinforcement. In recent years, some of the limitations of steel fibers, such as durability issues, due to low corrosion resistance, and finishability problems, have led to the introduction of synthetic fibers as an alternative fiber material.

Currently, most applications of steel fibers are in the field of tunnel construction, such as industrial floor [3], and concrete pipes [4], with typical dosages ranging from 0.26 to 0.78% in volume fraction. Other applications are the use of steel fibers as partial shear reinforcement in reinforced concrete beams and plates [5], or as a primary reinforcement in flat slabs [6]–[8]. Synthetic fibers are relatively new materials, and since their introduction, they have been used in applications such as slab-on-ground construction and, more recently, in concrete pipe production.

Wilson and Abolmaali [9] compared the behavior of steel fibers and polypropylene synthetic fibers for dry-cast concrete used in pipe production. They concluded that fibers, in general, improve the ductility and crack-width control.

Compared to normal concrete, the tensile behavior of fiber-reinforced concrete (FRC) is enhanced, creating a vast interest in studying tensile behavior of FRC members. Bridging the crack surface by fibers provides a post-cracking strength for the FRC members, which subsequently controls the crack width opening and increases the overall tensile strength and ductility of the material [10]. Therefore, understanding and simulation of the post-cracking behavior of fiber-reinforced concrete is essential for the development of design methods.

Post-cracking behavior of fiber-reinforced materials can be assessed and simulated by obtaining the tension-softening curve of the material. The tension-softening curve is the relationship of the gradual stress drop and the crack opening displacement or strain. Simulation can be performed by stress-crack width (σ-w) or stress strain (σ-ε). In the case of low fiber dosage, when multiple cracking does not occur, σ-w and σ-ε can be correlated by introduction of a characteristic law [11]. It has been shown that the σ-w is most preferable for modeling low fiber dosages of steel fiber-reinforced concrete [12].

The tension-softening curve can be directly obtained from the uniaxial tensile test. Theoretically, the uniaxial tensile test can directly obtain the σ-w relationship, but performing this test is rather difficult and requires a special test setup and equipment to avoid errors, such as eccentricity of the load, which can lead to a cracking stress lower than the actual stress at the onset of the crack[13]. In order to avoid the problems associated with the uniaxial tensile test, it is generally preferred to use indirect methods, in the form of the splitting tensile test [14], three-point notched beam bending test [15]–[17], 4-point bending tests on non-notched beam specimens or a

round-panel test [18]. Subsequently, the σ-w relation can be obtained by means of the inverse analysis method [11], [19].

There have been many studies on the post-cracking behavior of steel-fibers-reinforced concrete (SFRC). It has been shown that higher fiber dosage has direct correlation with higher post-cracking strength [20]–[24]. Fiber orientation in the direction of applied stresses and random distribution in the SFRC are other factors that strongly impact the post-cracking behavior of the SFRC material [25].

Abrishambaf et al [11] used an indirect method by means of a splitting test and inverse analysis to obtain the stress-crack width law for self-compacting SFRC. They concluded that the inverse analysis can predict the uniaxial tensile post-cracking behavior with a satisfactory accuracy. Many researchers have also utilized the three-point bending test on notched beams (e.g.;[19]). Typically, inverse analysis, on both the 3-point notched beams and the splitting test, is based on fitting the experimentally obtained load-crack width response at the notch point. Michel et al [26] performed a series of four-point bending tests and round-plate tests on unnotched beams. By numerically modeling the assumption of a crack pattern for a static system, they performed an inverse analysis based on the load-deflection results obtained through the experiment.

A better understanding of the cracking process, crack geometry, crack propagation, and crack width of the FRC material is necessary in order to perform indirect methods and obtain the stress-crack width law. The splitting and notched beams under 3-point bending tests utilize the mechanical extensometers, such as clip gauge extensometer or LVDT, in order to measure the crack opening at the location of the notch; however, the classic measurement methods have several limitations and reaching a high degree of precision is problematic.

In recent years, several crack measurement techniques have been developed in the field of fracture mechanics. Holographic interferometry, dye penetration, scanning electron microscopy,

acoustic emission, and image processing are among the methods used for measuring the crack profile [27]. The image processing methods are less complicated and economically more viable than other methods. Among the available image processing methods, Digital Image Correlation has become very popular among researchers. Digital Image Correlation (DIC) is a non-contact, non-destructive, full field measurement system that can provide a full displacement field of an object subjected to forces. The analysis is based on the comparison of images taken at consecutive time intervals or under different loading conditions. Full field measurement is obtained [28] by dividing an image of the surface into subareas, also called subsets, and comparing the positions of the subareas of the consequent images and the reference image. Constant advancements in high resolution cameras and image processing methods have made the DIC method applicable in many areas of laboratory testing. Pan et al [29] considered the DIC as an optical measurement technology with broad application prospects .

Continuous advancements and applications of the polypropylene synthetic fibers as an alternative reinforcement for dry-cast concrete members have suggested the need for a more thorough investigation of their behavior as a FRC material. The present study aims to investigate the post-cracking behavior of dry-cast synthetic fiber-reinforced concrete under flexural loading. In the first stage, experimental studies were conducted, including the 3-point bending test on notched specimens and 4-point bending test on non-notched specimens. The validity of the 2D DIC method for crack measurement was assessed by comparing the crack width data obtained with the extensometer and DIC technique in a simple 3-point bending test. Crack width and crack propagation were investigated. Numerical investigation of flexural cracking was performed by the 3D nonlinear finite element method. A post-cracking constitutive law (stress-crack width) in tension was assumed, using a piecewise function and considering the decreasing stress with growing crack displacement. An inverse analysis procedure was performed, using a numerical fitting procedure with 3D nonlinear finite element method and concrete damage plasticity (CDP). Crack width data

obtained from the FEM method was compared with the DIC result. Finally, the fracture energy was calculated based on the obtained stress-crack width curves.

Overview summary

- Verification of the accuracy of the Digital Image Correlation (DIC) method for crack width measurement by means of comparison with the experimental result obtained from the clip gauge extensometer in a simple 3-point notched beam test;
- Performing flexural tests, including 3-point bending on notched beams and 4-point bending test on unnotched beams for two volume fraction of dry-cast synthetic fiber-reinforced concrete;
- Crack assessment by means of crack width and crack propagation, using DIC method;
- Finite element modeling of 3-point and 4-point bending tests;
- Obtaining the tension-softening curve by means of inverse analysis;
- Calculation of crack width based on the numerical results of FEM modeling;
- Calculation of fracture energy based on tension softening curves.

1.2 Literature Review and Concepts

1.2.1 Synthetic Fiber

Advantages of steel fibers as an alternative form of reinforcement have led the industry and researchers to consider the possibility of fibers with different types of materials. Alternative types of fiber materials have both advantages and limitations. Although steel fibers have been around for many years in different types and shapes. Low corrosion resistance and finishability problems have prompted both industry and researchers to incorporate nonmetallic materials as an alternative to steel fibers. Various types of synthetic and natural materials, such as glass, nylon,

acrylic, polyester, carbon, aramid, polyethylene, and polypropylene have been used in FRC. In recent decades, studies on synthetic fiber materials have resulted in enhancing concrete toughness, impact resistance, crack width control, and shrinkage control [9], [30]–[33].

Studies of synthetic fibers are limited and even contradictory in some respects, e.g., whether the fibers enhance or decrease the structural strength of the concrete members. Alhozaimy et al [30] used synthetic fibers at low volume fraction of 3% or less for normal concrete. Research was performed on flexural, compressive, and impact strengths. The compressive strength showed an increase of 21-23%, the flexural strength did not show any significant change due to fiber percentage and the flexural toughness was found to be affected. The study concluded that the polypropylene fibers had no significant effect on compressive or flexural strength and that the fibers increase flexural toughness and resistance to failure impact.

Song, Hwang, and Sheu [31] investigated the compressive strength, splitting tensile strength, impact resistance, and modulus of rupture for polypropylene and nylon fiber-reinforced concrete and compared it with plain concrete. Their study showed a 5.8% increase in compressive strength for polypropylene fibers and an increase of 12.4% for nylon fibers. Splitting tests were performed and resulted in an increase of 9.7% for polypropylene and 17.1% for nylon FRC compared with plain concrete. During the splitting tests, fibers bridged the split and continued to carry load. Modulus of rupture was found to increase by 1.5% in polypropylene FRC and 5.6% in nylon FRC in comparison with plain concrete. An 11.9% increase of impact resistance and 17% increase of failure strength for polypropylene, and an increase of 19% and 30.5% for the first crack and failure strength, respectively, were observed for nylon FRC. The study concluded that both fibers enhanced the material property of concrete compared to plain concrete.

Investigation of post-cracking strength and creep behavior of polypropylene and nylon FRC was part of the study conducted by Kurtz and Balaguru [32]. Polypropylene and nylon FRC,

with dosage of 1.5 lb. /yd3, was evaluated for post-crack strength, time-dependent post-crack strength behavior, and compressive strength. Both polypropylene and nylon FRC showed a small post-cracking load bearing capacity. Although nylon FRC showed a faster rate of creep than polypropylene, it was found that the net deformation due to creep was not significantly different.

Comparing the material behavior of steel FRC with synthetic FRC was investigated in the works of Atis et al. [33] and Wilson and Abolmaali [9]. Atis et al. [33] studied the compressive strength, flexural strength, and abrasion resistance for various types of steel and synthetic fibers with varying fly ash quantities in FRC. Volume fractions of 0.05%, 1%, and 0.2% for synthetic fibers and 0.25, 0.5, 1, and 1.5% of steel fibers were used in the study. They found that the addition of steel fibers increases the abrasion resistance and flexural strength, but does not affect the compression behavior. No increase was found in the abrasion resistance of synthetic fibers (polypropylene).

Wilson and Abolmaali [9] compared the material properties of dry-cast concrete reinforced with steel and synthetic polypropylene fibers. Fiber dosages of 4, 8, 12, 16, and 18 lb./yd3 of polypropylene fibers and steel fiber dosages of 22, 33, 44, 66, and 88 lb. /yd3 were used for the investigation of compressive strength, first peak load, modulus of rupture, and flexural toughness. Steel FRC and synthetic FRC with higher dosages were found to show a hardening behavior after the initiation of the first crack. Overall, the study concluded that both steel and synthetic fibers enhance the ductility of concrete members and can be used as an alternative reinforcement for dry-cast applications.

Roesler et al. [34] conducted a study on the monotonic loading of fiber-reinforced slabs, using two volume fractions of fibers and various types of steel and synthetic fibers. A flexural test of the slabs showed no change in comparison with plain concrete when the volume fraction was less

than 1%. On the other hand, a flexural strength increase of 30% for hooked-end steel FRC and synthetic FRCs, and 55% for the crimped steel FRCs was found.

Most of the studies concluded that adding steel and synthetic fibers to the concrete mix causes ductile post-cracking behavior and an increase of toughness, and provides a secondary after-crack tensile resistance. Fibers that span the interface of the crack hold the crack surface together by means of a bridging effect and provide a residual load-carrying capacity. More toughness represents a larger area under the stress-strain curve, which subsequently leads to a greater capacity for energy absorption. Figure 1-1 shows the effect of fiber volume fraction on the toughness of the material.

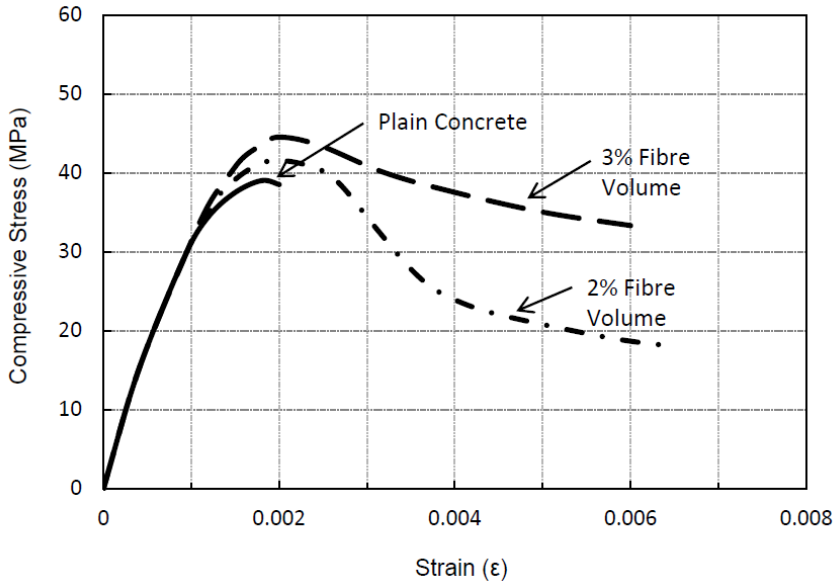

Figure 1-1 Toughness of Steel FRC with Various Volume Fractions [35]

1.2.2 Tension Softening

One of the main advantages of fiber-reinforced concrete is its stable post-crack tensile behavior. Post-crack tensile behavior of FRC is dependent on fiber distribution and orientation through the matrix. Fiber orientation and distribution is also governed by the casting procedure, concrete mix design, and specimen geometry and size [36]. Stable tensile behavior of FRC guarantees a more ductile behavior than plain concrete, and stress-strain (stress –crack width) presents a residual tensile strength for the material after crack. Fibers across the crack act as a stitching element, and a residual tensile strength can be obtained by controlling the crack width opening [37].

Tension softening, or the strain-softening curve, is the relation of the gradual stress drop to the crack opening displacement or strain after concrete reaches its tensile strength. Fiber-reinforced concrete members show a pattern of softening, different from normal concrete, after reaching their tensile strength. Due to the phenomenon of fiber bridging, a residual tensile strength continues to carry load, and a relative strain-hardening can be obtained with a sufficient fiber dosage. In the case of high dosage of fibers or high-performance-fiber-reinforced concrete, this behavior can present a clear strain hardening behavior, and residual strength exceeds the tensile strength. Strain hardening in high dosages of fibers primarily presents multiple cracks, and tensile capacity continues to grow until failure. Figure 1-2 presents a schematic comparison of tensile behavior for three types of fiber-reinforced concrete.

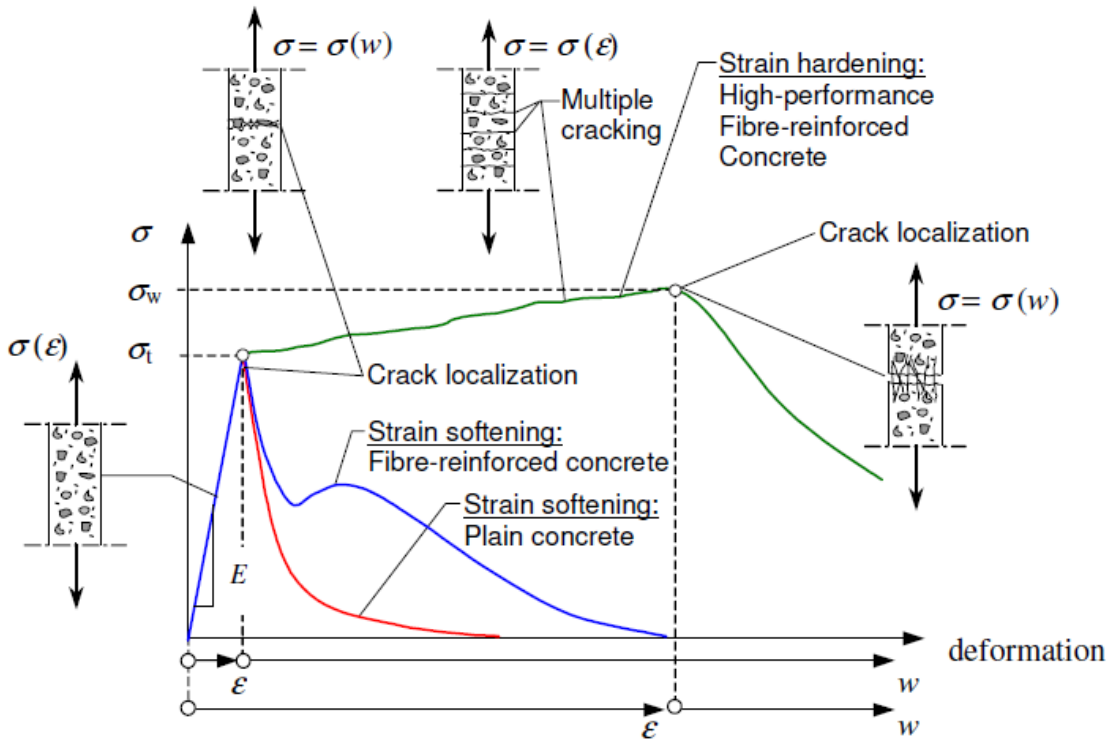

Figure 1-2 Tensile Behavior by Löfgren [38]

Studying the cracking process and tensile fracture in FRC members requires a comprehensive understanding of tensile behavior of the material in the post-cracking region. The tension-softening curve can provide a detailed view of the behavior of concrete in the tensile zone and is essential for numerical modeling of fiber-reinforced concrete.

1.2.3 Flexural Stress Block Diagram for Steel Fiber Reinforced Concrete

The structural design of a concrete member requires the location and magnitude of forces acting on the cross section. A simplified stress block diagram, showing the tensile and compressive stresses acting on the concrete element, has been used widely in the design process. Studies on the specific stress behavior of synthetic FRC are scarce, but there have been several studies that considered the behavior of steel FRC materials. Tlemat et al [39] defined four phases for flexural cracking and their respective stresses for steel FRC beams (Figure 1-3).

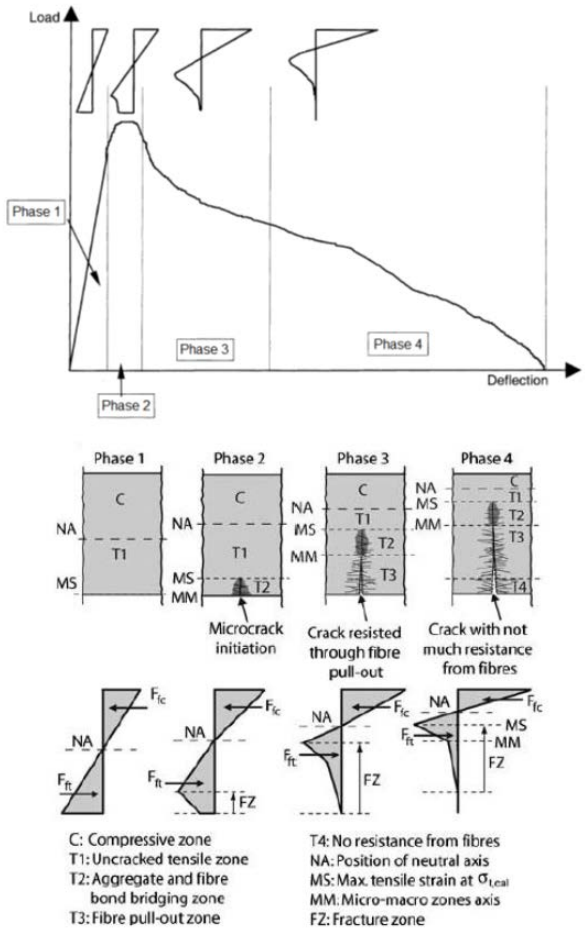

Figure 1-3 Schematic Flexural Cracking Phases and Their Respective Stress-softening Curve of Steel-Fiber-Reinforced Concrete (Tlemat et al.,[39]*)*

Phase 1: There is no crack in the tensile region, and the stress-displacement relationship can be considered as linear elastic. During this phase, the fiber geometry has no effect on the load bearing capacity, and the tensile strength is only related to the concrete matrix and fiber ratio.

Phase 2 begins with the initiation of the first crack in the tensile zone. The concrete has reached its tensile strength. There is a sharp drop in stress capacity, and tension softening starts in the fracture zone (FZ). As the crack starts to open from a crack width of around 0.1 to 0.2 mm (0.0039 to 0.0079 in.), fiber with sufficient embedment starts to carry extra load, but shorter fibers

begin to pull out. Phase 2 ends by the complete establishment of the crack, and more fibers reach their peak strength and start to pull out from the concrete matrix. In phase 2, stress-deformation behavior changes from elastic to more of an elastic-plastic behavior.

Phase 3 begins after the complete initiation of the crack, and the only resistance is through the fiber pull-out. Most pull-out resistance occurs by the fibers perpendicularly crossing the crack. At this point, the fiber orientation has a significant effect on pull-out resistance against the crack opening. By the increase of the crack width, the neutral axis moves toward the compression zone, causing more fibers to lose their resistance due to pull out. As the crack width increases, most fibers pull out without presenting more residual strength.

Eventually, at phase 4, no tensile strength remains in the concrete, and the only resistance comes from the areas in which the fibers are still engaged.

1.2.4 Experimental Crack Measurement

Plain concrete is a weak material in tension and undergoes a brittle and sudden failure after the initiation of the crack. But as mentioned earlier, the addition of fibers can greatly improve the tensile behavior of the concrete material and render a more ductile and stable post-cracking behavior. Experimental investigation of the tensile and post-cracking behavior of solid materials requires a reliable and precise method of measurement for material deformation and fracture geometry, including the crack width and crack propagation.

Conventional methods of crack inspection can be divided into manual and automatic methods. Manual methods require the researcher or technician to monitor the crack opening by means of measurement tools, such as a graduated scale (cracks' comparator) (Figure 1-4).

Figure 1-4 graduated scale (cracks' comparator)

Manual methods suffer from multiple problems, including difficulty of use during the test, subjectivity of measurement, and low precision and traceability, all of which can lead to unreliable and inaccurate measurements. Manual methods do not allow for continuous crack measurement during the test; therefore, a full load-crack width relationship or stress-crack displacement relationship cannot be obtained. The most common method being used for automated and continuous crack monitoring is extensometers, such as clip gauge or LVDT (Figure 1-5).

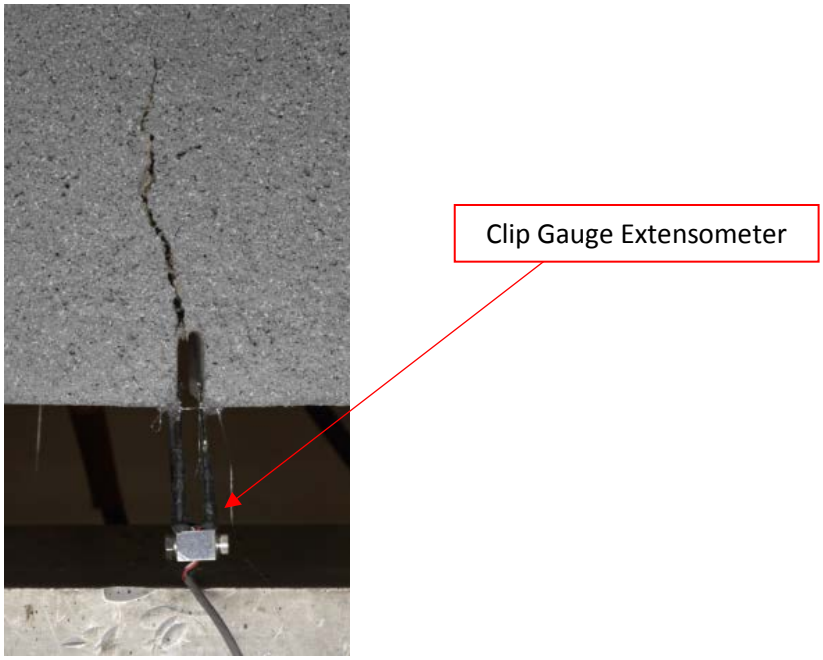

Figure 1-5 Clip Gauge Extensometer

Limitations of extensometers, including the pointwise assessment, limited range, and scaling difficulties have led researchers to look for more advanced and comprehensive methods of deformation measurements.

In recent years, several crack measurement techniques have been developed in the field of fracture mechanics. Holographic interferometry, dye penetration, scanning electron microscopy, and acoustic emission and image processing are among the methods used for measuring the crack profile [27]. Image processing methods are less complicated and economically more viable compared to other methods. Digital Image Correlation (DIC), as an image-based metrology method, has proved to be one of the most reliable methods for full field measurement [29]. In the current study, the DIC method was utilized for experimental measurement of crack width and crack geometry.

1.2.5 Digital Image Correlation

1.2.5.1 Introduction

Digital Image Correlation (DIC) is an image processing metrology method based on analyzing successive images taken during different stages of loading to obtain full displacement field of the test specimen.

Digital image correlation has been widely used in the field of civil engineering laboratory testing. Applications in the field of geotechnics include investigating asphalt-aggregate mixtures [40], evaluating shear banding in dilative sands [41] and evaluating visco-elastoplastic damage of asphalt-aggregate mixtures [42]. Applications of the DIC method have become very popular in the field of structural engineering research in recent years [27], [43]–[45]. Some of the applications are investigation of concrete fracture properties [43], [46], investigation of strain localization in concrete [47]–[49] and bond behavior between concrete and FRP sheets [45], [50], and evaluation of the concrete module of elasticity [51].

1.2.5.2 Digital Image Correlation (DIC) Applications in Crack Measurement

The DIC method for crack width measurement has been utilized by many researchers in the fields of fracture mechanics and structural testing. Fayyad et al [52] used 2D DIC to investigate the crack displacement of small-scale-reinforced beams under 3-point bending. The study then compared the result of the DIC measurement with crack mouth opening displacement (CMOD), obtained through a clip gauge extensometer. It was concluded that the DIC method is an effective method of crack measurement that can be used to monitor the crack profile in small-scale-reinforced concrete.

Destrebecq et al. [53] utilized the DIC method to analyze cracks and deformation in a full-scale reinforced concrete beam. Images of five loading cycles were analyzed, and displacement fields were calculated. By analyzing the displacement field, researchers calculated the crack widths, as the displacement jumps in a horizontal direction. Comparison of crack width results with theoretical values in the design codes were performed, and the existence of a compressive force due to moisture swelling was proved.

Ferreira et al [54] used DIC coupled with the boundary element method. Their research calculated Young modulus and fracture parameters associated with cohesive models. They concluded that the measurement with DIC is trustworthy due to numerous measurement points that can be used as input in the identification formulations.

1.2.5.3 Digital Image Correlation Concepts and History

Experimental fracture studies require an accurate surface deformation measurement of materials subjected to different types of loading (mechanical, thermal, etc.) at various time intervals. Many non-contact optical methods of full field measurement have been developed and applied for this purpose [55]: interferometric methods, such as holography interferometry, speckle

interferometry, and moir´e interferometry; and non-interferometric methods, including the grid method [56], [57] and digital image correlation (DIC).

Deformation measurements in interferometric methods are based on analysis of the phase difference of reflected light waves from the surface, before and after the deformation. Low vibration environment and coherent light are two of the main requirements of the interferometric methods. Results are in the form of fringe patterns and require a fringe processing in addition to phase analysis techniques. Non-interferometric methods consider the gray scale intensity of the specimen's surface and calculate the deformation field by analyzing the changes in the gray intensity at different stages of deformation. Non-interferometric methods have fewer requirements and complications, making them more convenient and economical than interferometric methods.

Digital image correlation (DIC) is a non-interferometric image processing method that has been widely used and advanced in the field of optical measurement. It is based on the comparison of a series of images with a reference or un-deformed stage. Images can be captured over different stages of loading or timescales, from microseconds to years. The DIC method was first developed at the University of South Carolina in the 1980s [58]–[61]. Pan et al [29] presented an extensive review of the history and principles of the DIC method.

In the last two decades, the DIC technique has become popular in the field of structural engineering research. It can be used for most of structural tests, including both the static and dynamics applications. The DIC technique can provide surface deformation data far into the range of plastic deformation. All of the analysis is done in post-processing, and 2D (in-plane) and 3D measurements (in and out of plain) can be performed by this technique.

The two-dimensional DIC method (2D DIC) can obtain planar deformation of a surface in applications where there is little or no out-of-plane movement. The 2D method uses a single camera to capture surface images. In cases of curved surfaces or three dimensional deformations, the 2D

DIC is not applicable. The three-dimensional DIC method (3D), based on the binocular stereo vision, was developed to overcome the limitation of 2D and can obtain deformation in any direction and on any surface [62]–[65]. Due to planar deformation, the 2D DIC method was used in the current study.

The digital image correlation method, as a non-interferometric method, relies on the gray intensity of surface. Surface preparation is necessary if the surface does not have sufficient gray intensity. Two methods of laser speckle patterns [66]–[69] and artificial white-light speckle patterns (random gray intensity patterns of the object surface) have been used to obtain the required gray intensity level. The laser speckle pattern is produced by use of a laser beam projected to the surface of the specimen (Figure 1-6). However, in cases of rigid body motion, large strains, or out-of-plane deformations, a decorrelation effect will occur, which leads to inaccurate measurements [70]. On the other hand, the white-light speckle patterns only require a white light source or natural light and are more popular among the researchers because of the ease of application.

Some of the advantages of the 2D DIC method compared to the interferometric optical techniques for 2D deformation measurement are as follows

:

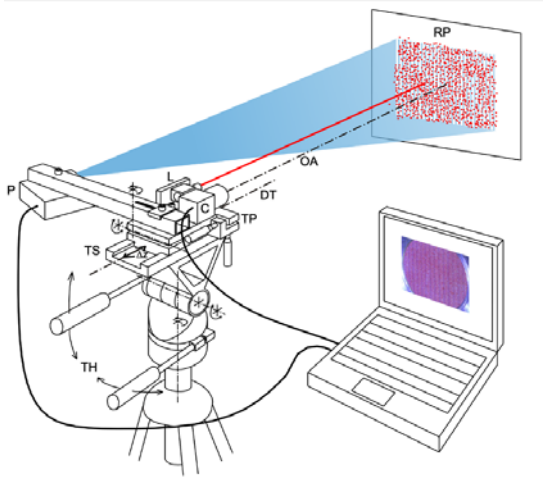

Figure 1-6 Laser Speckle Pattern and Fringe Projection [71]

- **Simple experimental setup and specimen preparation**

An easier experimental setup, compared to the other methods, makes the 2D DIC method very attractive for researchers. Digital images of the specimen surface are captured with only one fixed CCD camera. In cases where the natural surface of the specimen has sufficient random gray intensity distribution, surface preparation is unnecessary, but can be easily done by preparing the surface with a random speckle pattern by means of spraying black and white paint (Figure 1-7).

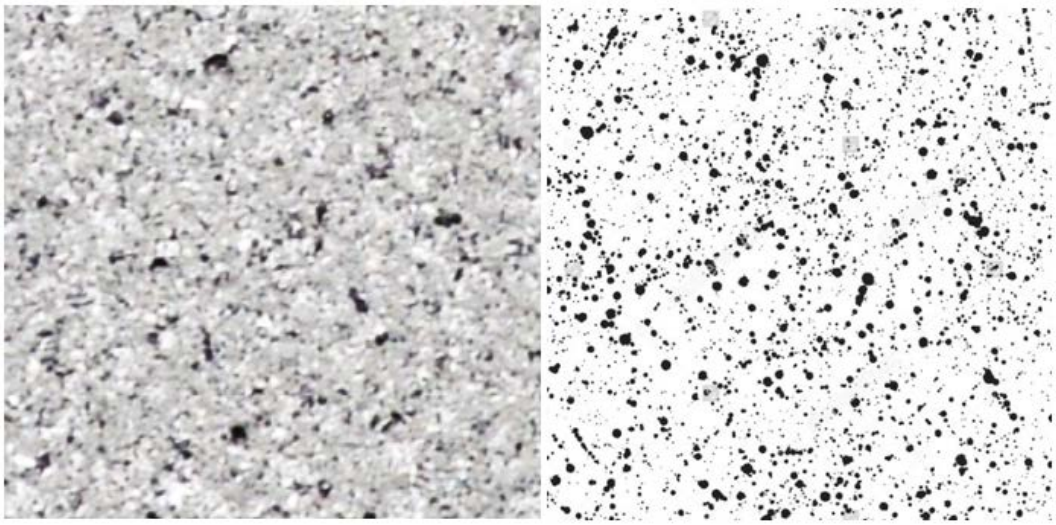

Figure 1-7 Speckle Pattern

Two-dimensional DIC does not require a coherent light source, and any white light, or natural light, in cases where there is not much change in the light intensity, can be used for illuminating the specimen surface. This makes the 2D DIC method applicable for both laboratory and in-field testing.

- **Wide measurement ranges of sensitivity and resolution**

The two-dimensional DIC method utilizes digital images and can process images captured by various types of digital image acquisition, including high-speed digital cameras. For micro and nanoscale measurement accuracy, 2D DIC can be used, along with optical methods such as optical

microscopy [72]–[74], laser scanning confocal microscope (LSCM) [75], [76], scanning electron microscopy (SEM) [77], [78], atomic force microscopy (AFM) [79], [80], and scanning tunneling microscope (STM) [81]–[83]. The main disadvantages that limit the 2D DIC method are as follows:

- The test specimen surface must have a random gray intensity distribution (speckle pattern).
- Image quality and resolutions have a direct effect on the accuracy of measurement results.
- Currently, the strain measurement with the 2D DIC method does not have the accuracy of interferometric techniques and is not recommended for non-homogenous materials with little deformation.

1.2.5.4 Basic concepts of 2D DIC

1.2.5.4.1 Experimental Setup

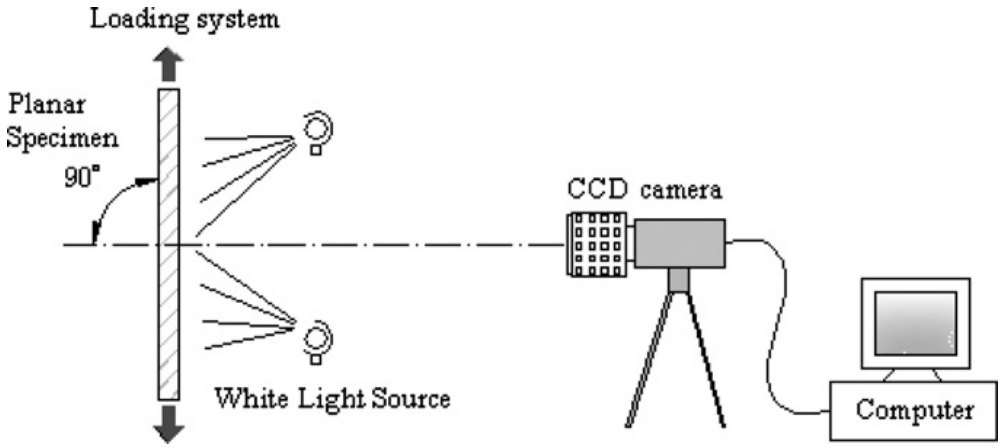

Figure 1-8 Schematic Illustration of a Typical Experimental Setup for the 2D DIC Method [29]

The two-dimensional DIC method requires a single CCD or CMOS camera. The camera needs to be fixed at a point with its optical field of view capturing the area of interest on the specimen surface. The camera's optical axis must be perpendicular to the surface of the specimen. The specimen's surface needs to be flat, and there must be no or insignificant out-of-plane displacement.

The specimen surface should have a random gray intensity distribution or speckle pattern. Speckle patterns can be made with black and white spray paints. An image of the surface must be taken before and after loading (Figure 1-8).

1.2.5.4.2 Basics principles of 2D DIC image processing

The first step in performing 2D DIC processing is specifying the area of interest or region of interest (ROI) in the reference image. The region of interest is divided into a square grid of smaller areas. A single rectangular patch, called subsets, is used at the intersection of the grid to track the deformation of intersection points. Displacement vectors are calculated at each grid point, and then a full field deformation contour can be obtained by implementing a proper shape function (Figure 1-9).

Processing in DIC is based on the comparison of consecutive images recorded during the test at various loading stages. Displacements are calculated by tracking a point on the recorded images and comparing the point location on a reference image of the specimen, recorded before the deformation.

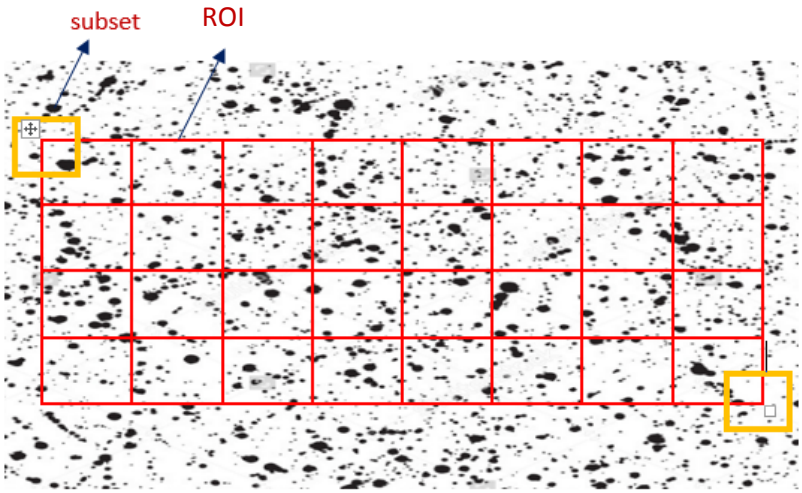

Figure 1-9 Reference Image: The yellow square is the subset used for tracking the motion of its center point; red grid intersections are the points to be calculated.

Displacement for point P (x_0, y_0) is calculated by choosing a reference subset of (2M + 1) × (2M + 1) with center point of P. The square subset is more optimal than a single pixel due to a higher probability of wide variation of the gray intensity level. A higher variation of gray intensity leads to better identification of the same subset in all images (Figure 1-10) [29].

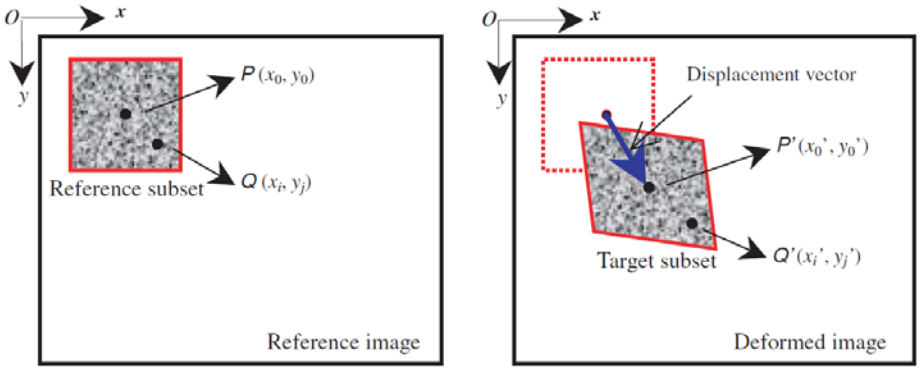

Figure 1-10 Schematic Illustration of Reference Subset and Deformed Subset [29]

To track a subset in images recorded during the test, it needs to be verified that each subset in all the images is similar to the reference subset. For this purpose, a cross correlation (CC) or sum-squared difference (SSD) correlation criterion must be identified, and a correlation coefficient should be calculated. A subset can be matched with the reference subset by searching for the peak value of the correlation coefficient. Maximum correlation values lead to identifying the location of the target subset. Comparing the target subset's center with the reference subset's center leads to the in-plane displacement vector of point P (Figure 1-10).

1- Displacement Shape Function

The square shape of the reference subset is changed in the deformed image. By assuming the deformation continuity of a solid object, a set of neighboring points remains as neighboring points from the reference subset to the deformed subset. Thus the point Q (xi , yi) on the reference

subset can be mapped to the point Q' (x'i , y'i) according to the following shape function [84] or displacement function [85]:

$$x'_i = x_i + \xi(x_i, y_i)$$
$$y'_j = y_j + \eta(x_i, y_i) \qquad (i,j = -M : M)$$

Equation 1-1

In the of case of only rigid body motion between the reference subset and the target subset, each point in the subset would have the same displacement, thus a zero shape function can be used:

$$\xi(x_i, y_i)=u \qquad \eta(x_i, y_i)=v$$

Equation 1-2

To sufficiently define the in-plane deformation of a subset, including translation, rotation, shear, normal strain, and any combination thereof, a first-order shape function is most commonly used:

$$\xi(x_i, y_i)=u + u_x \Delta_x + u_y \Delta_y$$
$$\eta(x_i, y_i)= v + v_x \Delta_x + v_y \Delta_y$$

Equation 1-3

Lu et al [85] proposed a second-order shape function that can depict more complicated deformation states of the target subset.

$$\xi_2(x_i, y_i) = u + u_x \Delta_x + u_y \Delta_y + \frac{1}{2} u_x \Delta_x^2 + \frac{1}{2} u_y \Delta_y^2 + u_{xy} \Delta_x \Delta_y$$
$$\eta_2(x_i, y_i) = v + v_x \Delta_x + v_y \Delta_y + \frac{1}{2} v_x \Delta_x^2 + \frac{1}{2} v_y \Delta_y^2 + v_{xy} \Delta_x \Delta_y$$

Equation 1-4

In the above equations 3-3 and 3-4, $\Delta_x = x_i - x_0$, $\Delta_y = y_i - y_0$

Where u, v are displacements components along the x and y direction of the reference subset center, P (x_0, y_0), u_x, u_y, v_x, v_y are the first order displacement gradients, and u_{xx}, u_{xy}, u_{yy}, v_{xx}, v_{xy}, v_{yy} are the second order displacement gradients of the reference subset center.

2- Correlation coefficient

The value of the correlation coefficient determines the level of similarity with the reference subset, during the process of searching for the target subset. The searching process stops when the peak value of the correlation coefficient is found in each image. There are several correlation criteria in the literature, but all of them can be put in two main categories: cross correlation (CC) or sum-squared difference (SSD) correlation criterion [86]. Tables 1-1 and 1-2 summarize these two categories of criteria for the correlation coefficient [29].

Table 1-1 Common Cross Correlation (CC) Criteria [29]

CC correlation criterion	**Definition**
Cross Correlation	$C_{CC} = \sum_{i=-M}^{M} \sum_{j=-M}^{M} [f(x'_i, y'_i) g(x'_i, y'_i)]$
Normalized Cross Correlation (NCC)	$C_{NCC} = \sum_{i=-M}^{M} \sum_{j=-M}^{M} [\frac{f(x'_i, y'_i) g(x'_i, y'_i)}{\bar{f}\bar{g}}]$
Zero Normalized Cross Correlation (ZNCC)	$C_{CC} = \sum_{i=-M}^{M} \sum_{j=-M}^{M} \left\{ \frac{[f(x'_i, y'_i) - f_m] \times [g(x'_i, y'_i) - g_m]}{\Delta f \Delta g} \right\}$

Table 1-2 Common sum-squared difference (SSD) Criteria [29]

SSD correlation criterion	**Definition**
Sum of Square Difference (SSD)	$C_{SSD} = \sum_{i=-M}^{M} \sum_{j=-M}^{M} [f(x'_i, y'_i) - g(x'_i, y'_i)]^2$
Normalized Sum of Square Difference (NSSD)	$C_{NCC} = \sum_{i=-M}^{M} \sum_{j=-M}^{M} \left[\frac{f(x'_i, y'_i)}{\bar{f}} - \frac{g(x'_i, y'_i)}{\bar{g}}\right]^2$
Zero Normalized Sum of Square Difference (ZNSSD)	$C_{CC} = \sum_{i=-M}^{M} \sum_{j=-M}^{M} \left[\frac{f(x'_i, y'_i) - f_m}{\Delta f} - \frac{g(x'_i, y'_i) - g_m}{\Delta g}\right]^2$

3- Sub pixel displacement

Digital images are made of discrete pixels; therefore, a full field displacement can only be obtained by means of a sub pixel displacement calculation [87]. Sub pixel displacement in a subset can be determined by an interpolation algorithm [29]. Different methods can be used for this purpose. Bilinear, bicubic, bicubic B-spline, or bicubic spline functions have been used in literature for interpolation. Detailed explanations of these methods can be found in various numerical computation books (e.g. [28]).

1.2.5.5 2D DIC Measurement Error Analysis

Although 2D DIC has fewer requirements than the other interferometric methods, it is still susceptible to various errors that can decrease the accuracy of measured data. Main sources of errors in a 2D DIC method application are as follows:

1. Errors due to specimen surface, imaging, and method of experiment;
2. Relative position of camera sensor and specimen surface;

3. Image distortions due to lens distortions.
4. Errors due to peripheral noises (e.g., shot noise, thermal noise, light intensity, etc.)
5. Errors due to correlation algorithm (subset size, correlation criteria, shape function, interpolation algorithm).

Pan et al. [29] provide a detailed review on the error sources and presented the following recommendations to improve the accuracy of the 2D DIC method:

Experimental conditions

- Use speckle pattern with high contrast;
- Make sure the camera sensor and specimen surface are parallel;
- Use a telecentric lens;
- Use a high quality camera, reduce the peripheral noise, and evenly illuminate the specimen surface.

Calculation Algorithm

- Use a large subset when the shape function matches the underlying deformation field;
- Use ZNSSD or ZNCC correlation criterion;
- Optimize the correlation with improved NR method;
- Use shape function with higher orders;
- Do the interpolation with a bicubic spline or biquintic B-Spline scheme.

1.2.6 Numerical Modeling and Inverse Analysis

Developing design methods and investigating the use of FRC materials in various types of structures can be significantly improved by implementation of numerical modeling methods, including the nonlinear finite element method (FEM). For accurate modeling of post-cracking

behavior of FRC in tension, the tensile behavior of the FRC needs to be introduced into the FEM model.

Most of the commercially available FEM packages (e.g., ABAQUS, ATENA, DIANA and ANSYS) describe tension softening of concrete by using a stress-strain (σ-ε) or stress-crack displacement (σ-w) relationship.

1.2.6.1 Tension Softening by means of Inverse Analysis

Obtaining the stress softening relationship of concrete in tension directly from an experiment requires an ideal uniaxial tensile test. As mentioned in the introduction, such test is not practical, and localization of stresses in response to cracks leads to an unreliable σ-ε or σ-w relationship. Thus, indirect methods must be utilized, in the form of the splitting tensile test [14], three-point notched beam bending test [15]–[17] or a round-panel test supported on a three point [18].

RILEM TC 162-TDF [88] proposed a simplified method to obtain the σ-ε for steel FRC based on the result of the 3-point bending test on a notched beam. The RILEM σ-ε model requires a set of parameters which can be obtained by using the experimental load deflection curves. These parameters are as follows: a) Load at the limit of proportionality (Fu), b) Flexural tensile strength at the limit of proportionality (ffct), and c) Equivalent flexural tensile strengths (feq2, feq3) [89].

The procedure for selecting the initial slope of load deflection curve is subjective. This subjectivity leads to an inaccurate selection of the Fu value, which subsequently leads to an inaccurate estimation of feq2, feq3. Thus, a 10% variation may be obtained in the result of ffct [90]. Another problem with the RILEM method is in the assumption used for calculation of stresses in the cracked section. Stresses are calculated by means of an equivalent elasto-plastic stress diagram. The stress diagram is obtained by assumption of specific values for neutral axis (0.66hsp and 0.9hsp, at feq2 and feq3, respectively). Tlemat et.al [91]and Hemmy [92] showed that the RILEM model

overestimates the load capacity of SFRC. Tlemat et.al [39] concluded that the RILEM stress strain model is a simplified design method for section analysis and is not intended to be used in general finite element modeling.

As was mentioned above, it is not easy to perform an ideal direct tensile test, and alternative indirect methods can be performed instead. Displacement-controlled flexural tests are simple alternatives to the direct tensile test. The stress-strain or stress-crack width law for use in FEM modeling can be developed by using the flexural test data.

Dupont and Vandewalle [93] used flexural experimental results to derive the σ-w law by using an iterative method called inverse analysis and FEM modeling, using ATENA software. They modeled the post-cracking part of σ-ε by a linear drop due to the restrictions of ATENA. Ostergaard et al [94] simulated the nonlinear behavior of a virtual hinge in the cracked area and used DIANA for inverse analysis by a bilinear-based σ-w law. Their method resulted in good agreement with experimental data. Hemmy [92] introduced fibers as 3D smeared reinforcements in ANSYS, but could not reach a satisfactory conclusion. Stang [95] defined a series of nonlinear springs between element nodes to simulate the crack and was in good agreement with the experimental results.

Michels et al [26] used the non-FEM numerical method for inverse analysis to obtain the tension-softening curve. Michel et al [26] performed a series of 4-point bending tests of non-notched beams and round-plate tests. Inverse analysis was carried out by a numerical modeling on assumption of a crack pattern for a static system. The load-deflection results obtained through the experiment were used in the inverse analysis procedure. Post-cracking behavior was obtained by assuming either exponential or tangent hyperbolic softening σ-ε law. The study concluded that exponential law is more accurate at small deflection levels, while the tangent hyperbolic law offers more accurate approximation.

2 Experimental study

2.1 Introduction

Investigation of the post-cracking behavior of synthetic FRC in flexure was part of this study's objectives. For this purpose, two series of ASTM beams and cylinder specimens were casted with a dry-cast mix design, using two volume fraction of synthetic fibers. Synthetic fibers with volume fractions of 0.54% (8.3 PCY) and 1.04% (16PCY) were used. A total of 12 beams and 6 cylinder were casted in the form of 6 beams and 3 cylinders for each fiber volume fraction.

The uniaxial compression test was performed based on an ASTM standard to obtain the maximum compressive capacity of the synthetic FRC specimens. Flexural beam tests were performed in the form of 3-point bending of notched beams and 4-point bending of unnotched beams. Test setup and loading conditions of the 3-point bending test were based on the recommendation of RILEM TC 162TDF [88] for fiber reinforced concrete. The 4-point bending tests were performed based on the test setup and loading conditions recommended by ASTM C1609/C 1609M – 12 [96]. Loading history and mid-span deflection were recorded during the flexural tests.

The two-dimensional DIC technique was utilized to obtain the surface deformation of the beam specimens. To verify the 2D DIC method, a preliminary verification study in the form of a simple 3-point bending test was performed on notched ASTM beams. Crack mouth opening displacement (CMOD) of the notched beam specimens was obtained with a clip gauge transducer during the tests. Result were compared with CMOD data calculated by using the 2D DIC method. Eventually, the crack width data was obtained for all the flexural tests (4-point and 3-point), using the 2D DIC method. Load- crack width curves were calculated based on the result of flexural tests and the DIC method.

2.2 Concrete Material

The ability to produce concrete with high strength, short curing time, and fast demolding, is one of the main interests of the precast concrete industry. Precast concrete production usually uses a small water-to-cement ratio and high compaction to obtain the desired concrete material. This type of concrete casting is generally referred to as dry-cast concrete. Dry-cast concrete is a common practice in pipe and box culvert production. Using a small water-to-cement ratio leads to a slump of zero and requires special methods of distributing and compacting the concrete. Compaction can be performed in the form of vibration, packing, spinning, or a combination of these methods to cast the concrete in the desired formwork.

This research investigated dry-cast concrete, reinforced with macro synthetic fiber. Fiber-reinforced beams and cylinders were produced, using two volume fraction of synthetic fibers. The concrete mix design was kept constant throughout the study, and the only varying factor was the fiber volume fraction. Coarse aggregate was a maximum size of 3/8 in, and the W/C ratio was 0.44. Two types of cementitious materials, including cement and fly ash, were used. Table 2-1 shows the details of the concrete mix design.

Table 2-1 Typical Mix Design (4000 psi)

Ingredient		**Amount**
Cement $\left(\frac{lb}{yd^3}\right)$		444
Fly Ash $\left(\frac{lb}{yd^3}\right)$		113
Water$\left(\frac{lb}{yd^3}\right)$		255
Sand$\left(\frac{lb}{yd^3}\right)$		1496
Aggregate 3/8” $\left(\frac{lb}{yd^3}\right)$		1774
W/C		0.44
Fiber Dosage	8.3 PCY (0.54 %) (lb.)	1.8
	16 PCY (1.04 %) (lb.)	3.6

MasterFiber MAC Matrix macro synthetic fibers, produced by BASF, were used as the fiber materials. This type of synthetic fiber is produced from a blend of polypropylene resins. The synthetic fibers used in the study all conformed to the ASTM C1116 ‘’Standard Specification for Fiber-Reinforced Concrete’’ [97]. Table 3-2 presents the specification of synthetic fibers.

Table 2-2 MasterFiber MAC Matrix Performance Characteristics [98]

Physical Properties	
Specific Gravity	0.91
Melting Point	320 °F (160 °C)
Ignition Point	1094 °F (590 °C)
Absorption	Nil
Alkali Resistance	Excellent
Tensile Strength	85 ksi (585 MPa)
Length	2.1 in. (54 mm)
Aspect Ratio	67
Fiber Type	Embossed
Material	100% virgin polypropylene
Chemical Resistance	Excellent

The manufacturer’s recommended fiber dosage is 3 to 12$\frac{lb}{yd^3}$. An earlier study performed by Wilson and Abolmaali ([4], [9]) used Master Fiber MAC Matrix Fibers in various dosages and showed material properties of synthetic FRC compared to steel fibers. The validity of using this type of fiber in pipe production was investigated and led to the development of the ASTM C1818 specification.

For this study two fiber dosage of 8.3 $\frac{lb}{yd^3}$ and 16 $\frac{lb}{yd^3}$ were used. Concrete mixture was produced using $\frac{lb}{yd^3}$ and then converted to volume fraction. Based on the Equation 2-1, volume fraction of 0.52 % and 1.04% was calculated for 8 $\frac{lb}{yd^3}$ and 16 $\frac{lb}{yd^3}$ respectably.

$$Fiber\ Volume\ (\%) = \frac{relative\ density}{mass\ per\ volume}$$

Equation 2-1

Figure 2-1 shows the shape of the synthetic fibers used in the study. Figure 2-1 shows that the fibers have small grooves to increase the bonding between the fiber and concrete matrix. This enhanced bonding can noticeably increase the bridging effect and pull out resistance of this type of fiber.

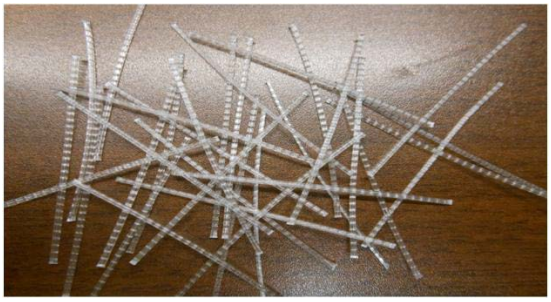

Figure 2-1 MasterFiber MAC Matrix Synthetic Fiber

A nine-gallon mixer was used to mix the concrete material. The manufacturer recommend adding the fiber at the beginning of the cycle, but not at the same time as the cement [98]. Fibers were measured by a digital scale and saturated by means of immersing them in water prior to adding them to the mixture.

Figure 2-2 Fiber Amount Measurement with High Accuracy Scale

Fibers were added gradually to the mix to prevent them from sticking together and to evenly distribute them throughout the mixture. Figure 2-3 depicts the mixture as the fibers are being added.

Figure 2-3 Fibers added to the Mixture

A total of 12 beams and 6 cylinders, 6 beams and 3 cylinders for each fiber dosage, was produced. Both steel beam and plastic cylinder molds were utilized. Molds were placed on the vibration table, and the concrete mixture was added in three equal thickness layers. Each layer was compacted by using a compaction hammer, the number of strokes kept constant for each layer so

that all of the beams and cylinders would have same level of compaction (Figure 2-4 and Figure 2-5).

Figure 2-4 Casting and Compaction of Concrete Cylinders

Figure 2-5 Beams after Casting

Molds were removed one day after casting. Specimens were kept in the curing room for 28 days before the test was performed (Figure 2-6).

Figure 2-6 Beams Kept in the Curing Room for 28 Days

2.3 Compression Test

Compression tests were performed to obtain the compressive strength of synthetic-fiber-reinforced concrete. Synthetic FRC cylinders were casted at the same time as the beam specimens. Three cylinders for each volume fraction of synthetic fibers, a total of 6 cylinders, were casted and cured for 28 days before the tests.

Cylinders were produced and tested based on ASTM C39 [99], with a 4-inch diameter. The test procedure was based on applying an axial force through the cylinder axis, up to failure in order obtain the compressive strength.

All the cylinders were capped to ensure a level surface of loading for the top and bottom and that none of the end surfaces of the cylinders were displaced more than 0.5 degrees (0.009 rad) from the perpendicular axis. Cylinders were put in molten silica, used as the capping material, until they cooled down and hardened to form the “cap.” This procedure was performed for both ends (Figure 2-7).

Figure 2-7 Capped Cylinder Specimen

A load-controlled compression machine, capable of inserting uniform load with a 400-kip capacity, was utilized to perform the compression tests. Tests were conducted with a loading rate of 35±7 psi/s (0.25±0.05 MPa/s). ASTM C39 allows the load rate to increase during the first half of the test, but it needs to be controlled so that the sudden increase of the load doesn't cause a premature failure. Experiment data was recorded, using a loading apparatus digital interface. By providing the base area of the cylinders to the system, the testing apparatus was able to report the ultimate force, break force, and ultimate stress of the specimens (Figure 2-8).

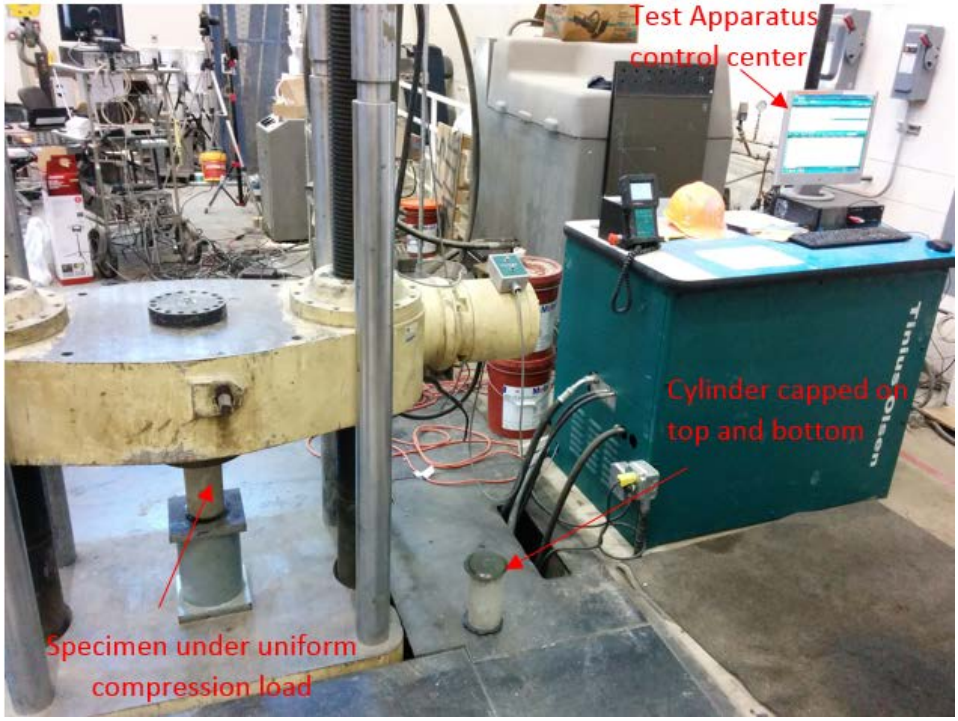

Figure 2-8 Compression Test setup

A compression test is complete when the specimen fails and the load is dropped to 5% of the maximum load

2.4 Flexural Experiment Test Setup

2.4.1 Three-Point Bending Test

Three-point bending tests were performed on 6 beams, 3 beams for each fiber volume fraction, with loading condition based on the recommendation of RILEM TC 162-TDF: Test and Design Methods for Steel Fiber Reinforced Concrete [88]. The existence of a notch on the tension side of the beams caused all the stresses to concentrate on the notched region and resulted in a single, controlled crack that began at the tip of the notch. A notch reduces the energy dissipation, concentrates all the energy on the opening of the crack, and makes it possible to control the cracking and crack mouth opening so that they can be measured by means of displacement transducers (e.g. clip gauge). For the above

reasons, most of the researchers prefer the three-point bending test for finding the tensile behavior and calculating the fracture energy of concrete members.

Three-point bending tests were performed on beams 6 inches wide and 6 inches deep, and 20 inches long (6x6x20 in). A notch with a depth of 1 inch and width of less than 0.2 inch was cut into the bottom surface of each beam, using a water-cooled concrete saw.

A MTS machine with the capability of producing a constant increase of deflection was utilized for the tests. This method of displacement control testing made it possible to obtain the post-crack flexural behavior of the beams.

The two supports and the device to impose the displacement were rollers that could easily rotate around their axis. The upper roller were capable of rotating around its axis and being inclined in a plain perpendicular to the specimen's longitudinal axis. A schematic view of the test arrangement is shown in Figure 2-9. The span length of the three-point loading was 18 in.

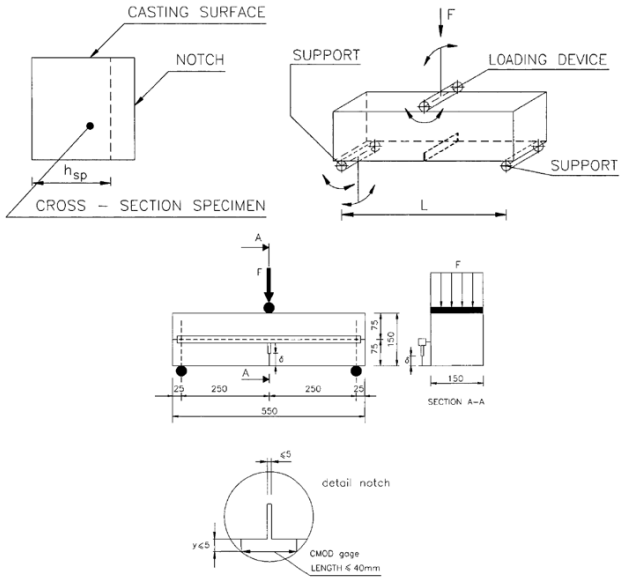

Figure 2-9 Schematic View of Test Setup based on RILEM TC 162-TDF [88]

Mid-span net deflection of the beams was recorded during the test, using a displacement transducer (LVDT) mounted to a rectangular jig. The rectangular jig ensured that the net deflection recorded at the mid-span was exclusive of the effects of seating or twisting the specimen on its supports (Figure 2-10).

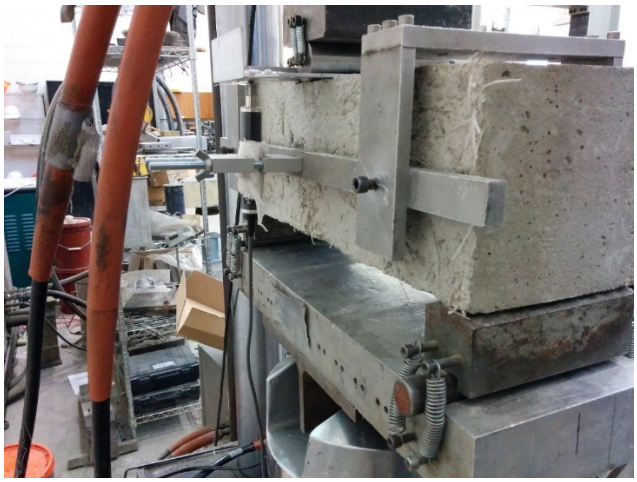

Figure 2-10 Arrangement for Obtaining the Net Deflection

A data acquisition system recorded loading and deflection data during the test. Data acquisition was performed using high-voltage channels connected to the MTS machine and LVDT, transferring data to a Vishay box. Test data then was recorded with StrainSmart data acquisition software (Figure 2-11).

Figure 2-11 Data Acquisition System and MTS Control Center

The digital image correlation method was used to obtain the displacement field and crack specifications. Images of the specimen were recorded during the test as an input for DIC analysis. A detailed explanation of the test setup for the DIC application, including surface preparation, camera type and position, and lighting device can be found in the “2D DIC Experimental Setup” section.

To decrease the DIC analysis time and simultaneously obtain sufficient deformation data, images were taken every 5 seconds during the test. As a reference stage, an image of the specimen was taken before the start of the test. Figure 2-12 presents the reference image taken for the DIC analysis and illustrates the test setup used for the three-point bending test.

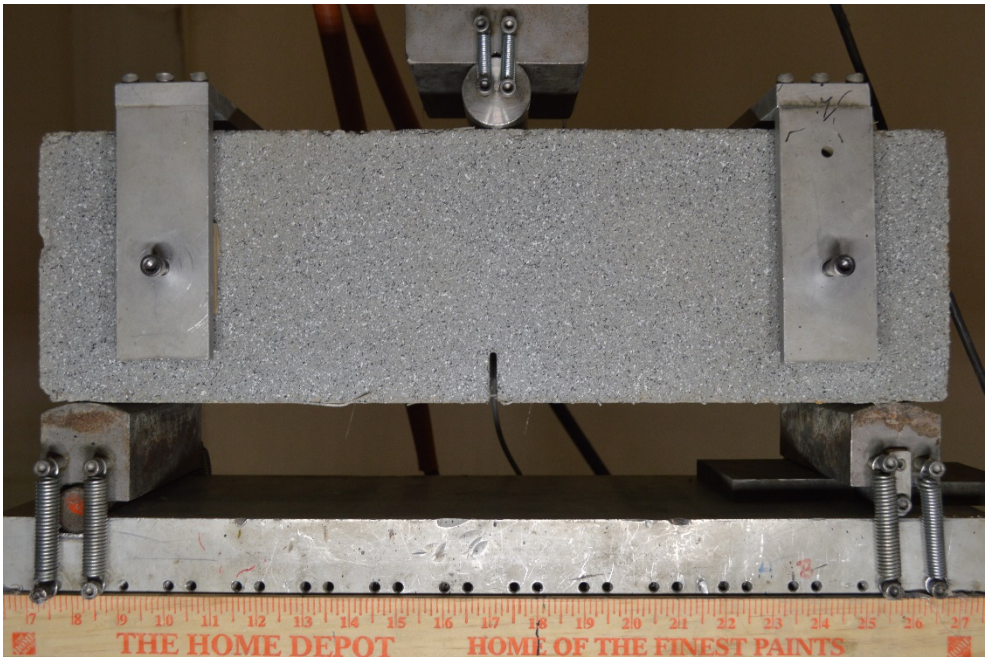

Figure 2-12 Three-Point Bending Test Setup

Based on the recommendation of RILEM TC 162-TDF [88], a displacement-controlled loading with a constant increase rate of 0.2 mm/min (0.0079 in/min) was inserted until the specific final deflection was reached. RILEM TC 162-TDF [88] recommends a final deflection of 2.65 mm (0.104 in), but to obtain more deformation data by means of the DIC method, the test was continued up to a mid-span deflection of 0.15 in.

2.4.2 Four-Point Bending Test:

Four-point bending tests were performed on 6 beams, 3 beams for each dosage of fiber. The 4-point bending tests were based on the recommendation of ASTM C1609/C 1609M – 12 [96]. Test method ASTM C 1609 is a standard flexural strength test for fiber-reinforced concrete. Tests were performed on unnotched beams. This test method provides the first peak strength, which characterizes the FRC behavior up to the initiation of the first crack.

Four-point bending tests were performed on the beams with 6 inch by 6 inch section dimensions and a length of 20 in (6x6x20 in).

A MTS machine with the capability of producing a constant rate of deflection increase was utilized to conduct the tests. Displacement control testing is essential to obtain the flexural behavior after the first peak.

Based on the recommendation of ASTM C1609, the beam testing arrangement was as described by ASTM C78-10 [100]. The specimen was arranged so that it was loaded at the third points. The two supports and the third points to impose the displacement were rollers that could easily rotate around their axis. The upper roller was capable of rotating around its axis and being inclined in a plain perpendicular to the specimen's longitudinal axis. A schematic view of the test arrangement is shown in Figure 2-13. The span length of the four-point bending test was 18 in.

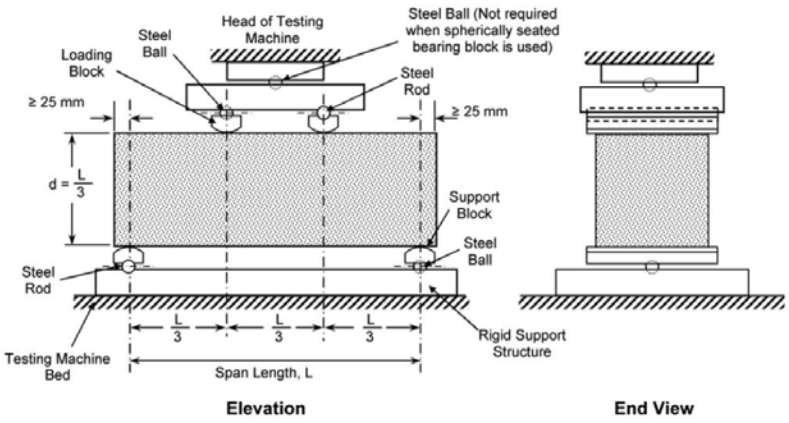

Figure 2-13 Schematic View of the Test Arrangement as per ASTM C78-10 [100]

Mid-span net deflection of the beams was recorded during the test, using a displacement transducer (LVDT) mounted to a rectangular jig (Figure 2-14). The rectangular jig ensured that the net deflection recorded at the mid-span was exclusive of the effects of seating or twisting of the specimen on its supports. ASTM C 1609 [96] recommends using two displacement transducers, but since the application of the DIC method required the images of the specimen surface, the second transducer was removed from the jig to clear the camera field of view (Figure 2-15).

Figure 2-14 Arrangement to Obtain the Net Deflection

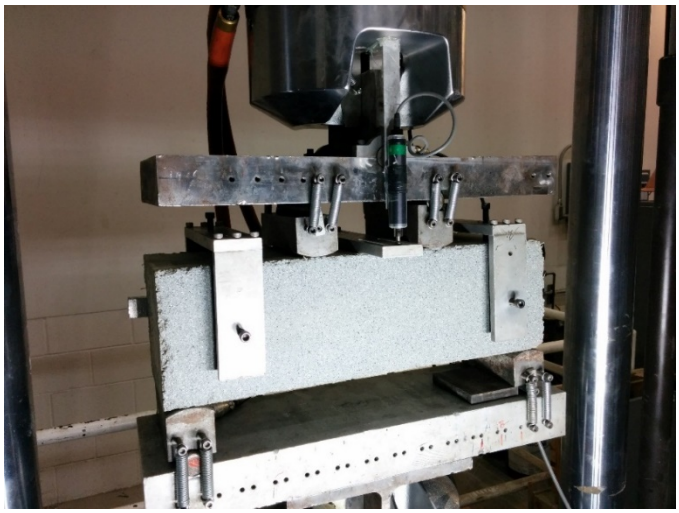

Figure 2-15 Test Setup for 4-Point Bending Test

A data acquisition system, as described in the 3-point bending setup, was used to collect loading and deflection data during the test (Figure 2-11).

The two-dimensional DIC method was used to obtain the displacement field and crack specifications. Images of the specimen were recorded during the test as an input for DIC analysis. A detailed explanation of the test setup for DIC application, including surface preparation, camera

type and position, and lighting device can be found in the “2D DIC Experimental Setup” section (Section 2.6).

To decrease the DIC analysis time and at the same time obtain sufficient deformation data, images were taken every 5 seconds during the test. As a reference stage, an image of the specimen was taken before the start of the test.

The ASTM C 1609 [96] recommends that the mid-span displacement increase with a constant rate of 0.035 to 0.1 mm/min (0.0015 to 0.004 in/min.), up to a net deflection of L/900. The rate then can be increased up to 0.3 mm/min (0.012 in/mm), up to the specified final deflection. Due to the application of the DIC method and to keep the deformation rate constant throughout the test, the entire test was conducted with a constant increase rate of 0.1 mm/min (0.004 in/min). The final deflection recommended by ASTM C 1609 [96] is L/150 or 0.12 in., but to obtain more deformation data by means of DIC method, the test was continued up to a mid-span deflection of 0.15 in.

2.5 Validation Test for DIC Crack Measurement

The validity of the 2D DIC measurement method was investigated by comparing the DIC results with the results of clip gauge extensometers on notched beams. For this purpose, various types of concrete materials were subjected to a 3-point bending test based on the RILEM [88] recommendation. Beams of steel FRC with 0.33% volume fraction, synthetic FRC with 0.54% volume fraction, and geopolymer concrete with 20% volume fraction were used. Beam specimens had a geometry of 6 in. width, 6 in depth, and 20 in. length (6x6x20 in).

The test setup was a single-point loading, with a span length of 18 in. and roller supports at the ends. A notch with a depth of 1 in. and width of 0.2 in. was cut into the bottom surface of each beam, using a water-cooled concrete saw (Figure 2-16).

Figure 2-16 Notched Beam Specimen

Figure 2-17 Test Setup of 3-Point Bending for DIC Validation

A displacement-control loading was inserted, using a MTS machine. The loading rate was kept constant for all the beam specimens at a rate of 0.2 mm/min (0.0079 in/min. A clip gauge

extensometer (Figure 2-17), type UB-5A with a capacity of 5 mm (0.2), was utilized to measure the crack mouth opening (CMOD) at the bottom of notch (Figure 2-18).

Figure 2-18 Clip Gauge Transducer (UB-5A)

Data acquisition was performed, using high-voltage channels connected to the MTS machine, with the clip gauge transferring data to a Vishay box. Test data then was recorded with StrainSmart data acquisition software (Figure 2-11). All tests were continued up to either total failure or CMOD value of 0.6 in. In order to perform DIC technique images of the specimen, the surface was captured before the test was started and every 5 seconds during the test. A special test setup for the 2D DIC technique was considered. (Section 2.6)

2.6 Two-Dimensional DIC Experimental setup

2.6.1 Surface preparation

As mentioned earlier in Chapter 1, a specimen's surface texture has a direct impact on the precision of the DIC technique. The digital image correlation method relies on the level of intensity of the gray region of interest, making surface preparation necessary. To provide an optimum surface texture, a random speckle pattern needs to be created on the specimen surface. The speckle pattern can be made by spraying black and white paint on the specimen's surface. In cases of smaller areas of interest and high precision, the speckle diameter needs to be relatively small and randomly distributed. As mentioned earlier, using large diameters for speckles, in the case of small ROIs, can

cause subsets to have insufficient gray intensity. Creating an ideal random pattern by means of spraying black and white paint separately requires several attempts. A common practice is to paint the entire interest surface with white paint spray, and then create black speckles by spraying black paint from a distance. This method usually requires several attempts to reach an ideal random pattern. Due to this difficulty, a paint spray with a stone textured finish, which contains small black and white pieces of stone, was used in this study (Figure 2-19). The final painted surface had a random distribution of black and white speckles on a gray background, which has the optimum grey intensity required to perform 2D DIC analysis. Figure 2-20 shows one of the notched beams after applying the stone texture spray, as well as a magnified view of the speckle pattern.

Figure 2-19 Spray Paint Used for Creating Speckle Pattern

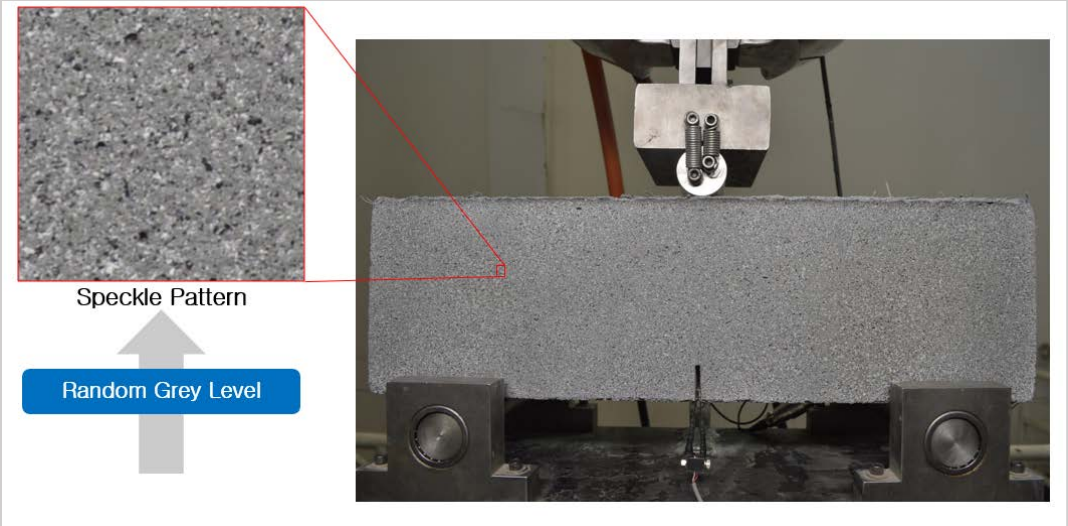

Figure 2-20 Test Setup and Surface Pattern

2.6.2 Image Acquisition System

The two-dimensional DIC technique requires a single camera with its optical axis perpendicular to the specimen's surface. A Nikon D3200 DSLR (Digital single-lens reflex) camera with a sensor resolution of 24.2 MPA was used for this study. It was mounted on a tripod and was carefully adjusted so that it was level and the optical axis was perpendicular to the specimen surface. Care was taken to ensure that there was minimal vibration and that the camera position was stable during the test. The distance from the specimen to the camera lens was adjusted so that the whole beam fit into the camera field of view (about 30 feet). Images were captured with a resolution of 6016x4000 pixels and were taken every five seconds throughout the test. All of the deformation analyses were performed after the test was completed.

2.6.3 Camera Settings

Camera focus, sensitivity of the image sensor (ISO), shutter speed, and focal point were adjusted manually and kept constant during the test. Although DSLR cameras offer auto adjustment, changes in the imaging system can lead to an inconsistency of the images and can reduce the precision of the DIC system. Adjustments were done based on the specification calculated by the

camera for the reference image (image taken before the test began), and then camera was set to the manual setting to keep the setting constant for the rest of the test (Figure 2-21).

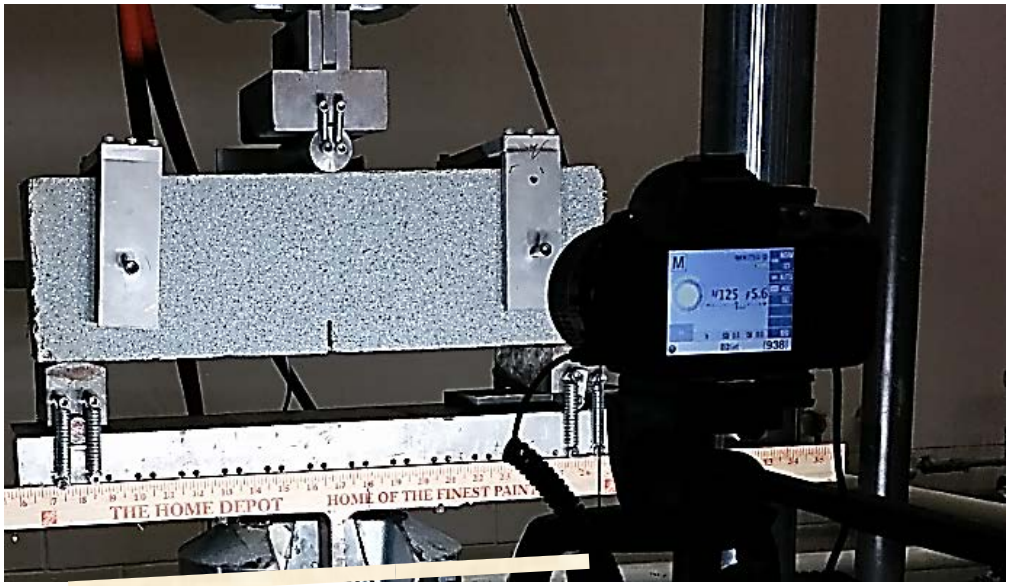

Figure 2-21 Manual Adjustment of Camera Settings

2.6.4 Lighting

The main source of peripheral noise in the DIC application is the light intensity of the specimen's surroundings. Providing a uniform lighting for the specimen's surface can eliminate the small changes in the light intensity of the surroundings. Because of this, care was taken to ensure that the laboratory lighting did not change drastically during the tests. In addition, a white 2500 Lumen LED lighting device was utilized to provide a uniform surface illumination (Figure 2-22).

Figures 2-22 to 2-24 show the complete test setups for the three types of flexural experimental studies performed.

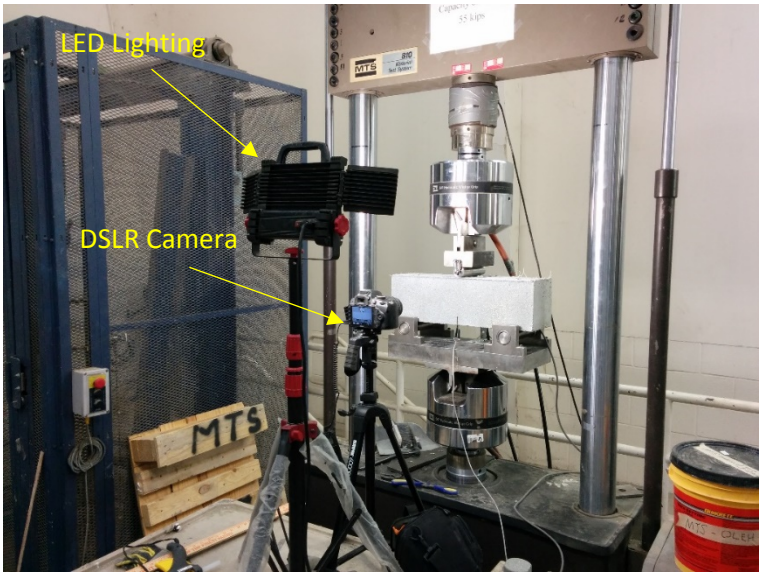

Figure 2-22 3-Point Bending Test Setup for DIC Validation - Camera and Lighting Device

Figure 2-23 3-Point Bending Test Setup and DIC System

Figure 2-24 4-Point Flexure Test Setup and Camera Setup

2.7 Test Results

2.7.1 Compression test results

Six cylinders, (three cylinders for each fiber volume fraction of 0.54% and 1.04%), were casted. Cylinders were casted from the same batch as the beam specimens and were tested at the same age as the beams. Figure 2-25 shows the results for the compression tests on cylindrical specimens.

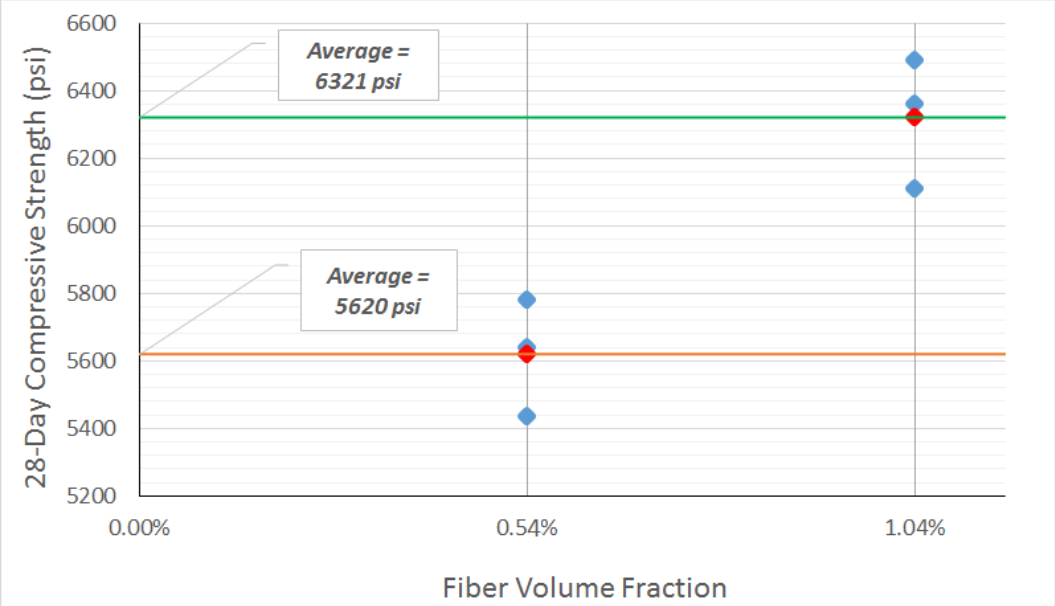

Figure 2-25 Compressive Strength after 28 Days (Fiber volume fraction of 0.54% and 1.04%)

As is presented in Figure 2-25, the addition of synthetic fiber to the concrete mixture increased the compressive strength of the concrete. It is worth mentioning that high compaction also contributes to the extra compressive strength of the synthetic FRC material.

2.7.2 Flexural Beam Test Results

2.7.2.1 Three-point Bending Test Results

Figures 2-26 and 2-27 shows the load-Deflection response of 3-point bending tests of notched beams with two fiber volume fraction.

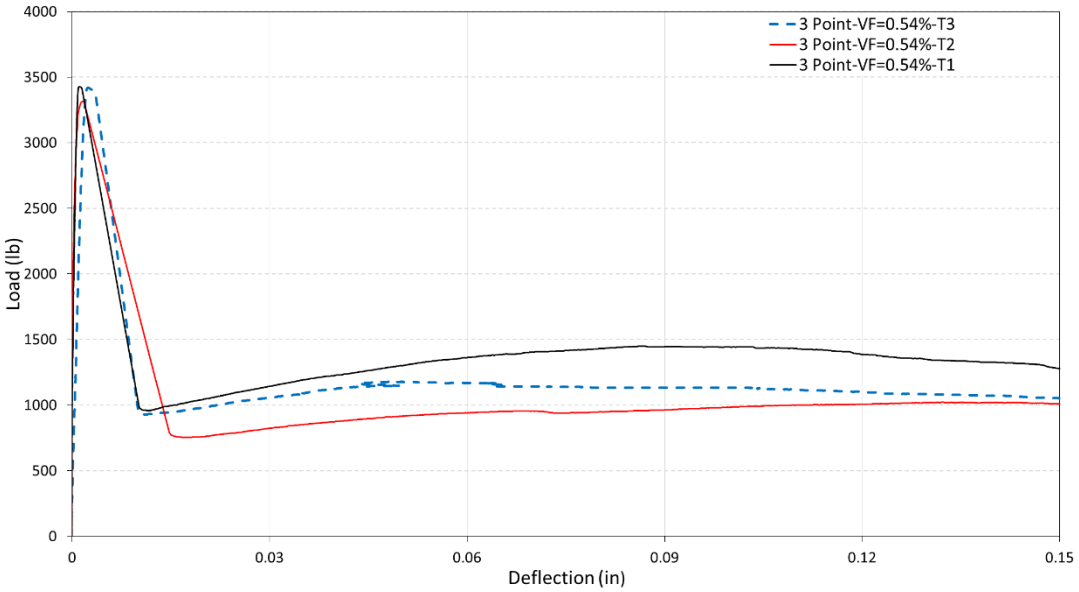

Figure 2-26 Load vs Deflection for 3-Point Bending Test – VF=0.54%

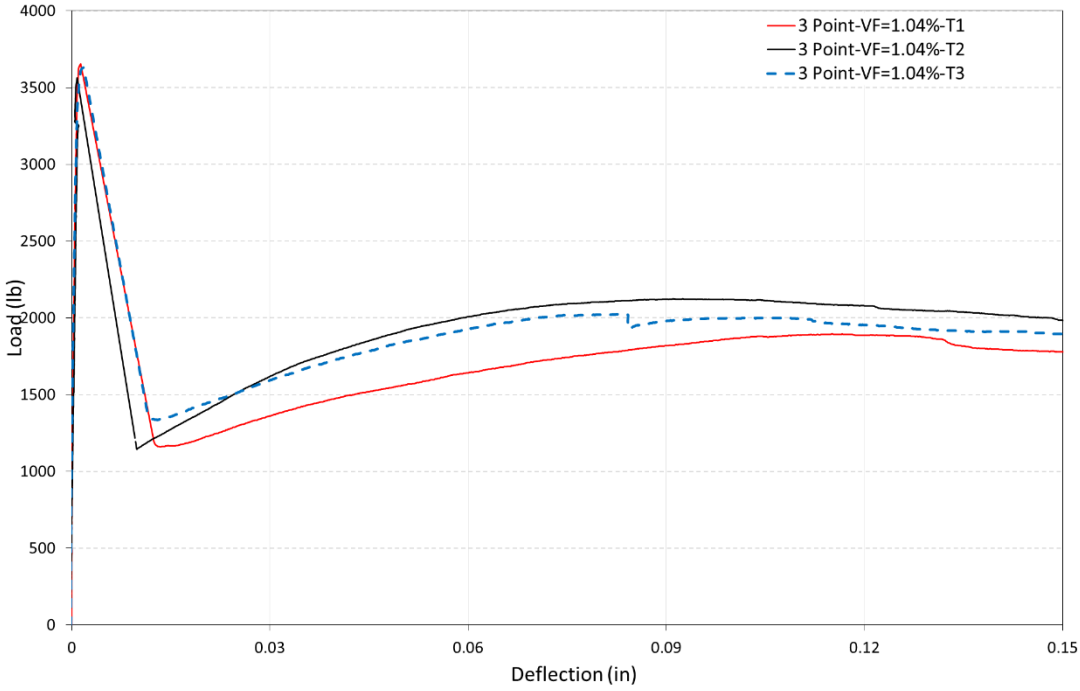

Figure 2-27 Load vs Deflection for 3-Point Bending Test – VF=1.04%

The existence of the notch causes cracking to start at top of the notch's location. This happens because stress is concentrated at a section on top of the notch. Consequently, in all the tests

performed for both fiber dosages, one macro crack started from top of the notch and propagated to the load point.

After the load reached its maximum value and the crack started, a jump in mid-span displacement occurred at the same time that a drop of the load bearing capacity occurred. This initial drop was less for the 1.04% fiber dosage than for the 0.54% dosage. This suggests earlier interaction of fibers in higher dosage of fibers. After the initiation of the crack and first drop, both fiber dosages presented a hardening state.

The result for the load capacity immediately after the crack was initiated, and the hardening state varied among the three tests for each fiber volume fraction. The same difference can be observed for the displacement jump after the crack initiated. This variation in the results can be seen for both fiber volume fractions and can be explained by the influence of fiber orientations on the post-crack behavior of the FRC materials.

Comparison of the load response of synthetic FRC with 0.54% and 1.04 fiber volume fraction does not show much difference between first peak loads. Although higher fiber volume fraction (VF=1.04%) shows a slightly higher peak load compared to the lower fiber volume fraction, the difference is not significant. This behavior suggests that in the elastic region and small level of deformations, it is just the concrete matrix that resists the loads. Fibers start to engage as soon as the concrete forms a macro crack, and the fibers are primarily acting in the form of a stitching behavior across the crack surface, known as bridging.

The bridging effect caused a residual load capacity and more ductile post-crack behavior for the synthetic FRC. This residual load bearing was more resonant in the beams with higher fiber volume fraction. There were some variations in the post-crack hardening state, which can be explained by the effect of the fibers' orientation. In the case of the 3-point bending test, the location

of crack was predefined due to the existence of the notch, but in random fiber orientation, the crack surface section leads to different levels of residual hardening.

Residual load bearing is more obvious in the case of 1.04% fiber volume fraction. The same mid-span deflection requires more force in the case of 1.04% volume fraction compared to the 0.54%. Considering the random distribution of fibers in the mixture, this phenomenon can be explained by the fact that the additional fibers increase the probability of the fibers orienting perpendicular to the crack surface, and the fiber bridging is more resonant.

The standard test method of RILEM TC 162-TDF [88] defines the stress corresponding to the first peak load of the load-deflection curve as the "Limit of Proportionality" (F_L). This stress can be calculated based on the Equation 2-2

$$f_{fct,L} = \frac{3F_L L}{2bh_{sp}^2}\left(\frac{lb}{in^2}\right)$$

Equation 2-2

Where:

b = width of the specimen (in)

h_{sp} =distance between tip of the notch and top of the cross section (in)

L= span length (in)

Table 2-3 shows the $f_{fct,L}$ stress for the 3 point bending test

Table 2-3 Limit of proportionality for 3-point bending tests

Fiber Volume Fraction	L(in)	b(in)	h_{sp}(in)	Test	F_L (lb.)	$f_{fct,L}$(psi)	Avg.$f_{fct,L}$(psi)
0.54%	18	6	5	T1	3409	613.6	604
				T2	3281	590.6	
				T3	3372	607	
1.04%	18	6	5	T1	3614	650	647
				T2	3638	655	
				T3	3528	635	

As it present in the table, limit of proportionality is slightly higher for the 1.04% fiber dosage compare to the 0.54% fiber volume fraction.

2.7.2.2 Four-point Bending Test Results

Figures 2-28 and 2-29 shows the load-deflection response of 4 point bending tests on unnotched beams with two volume fraction of fibers.

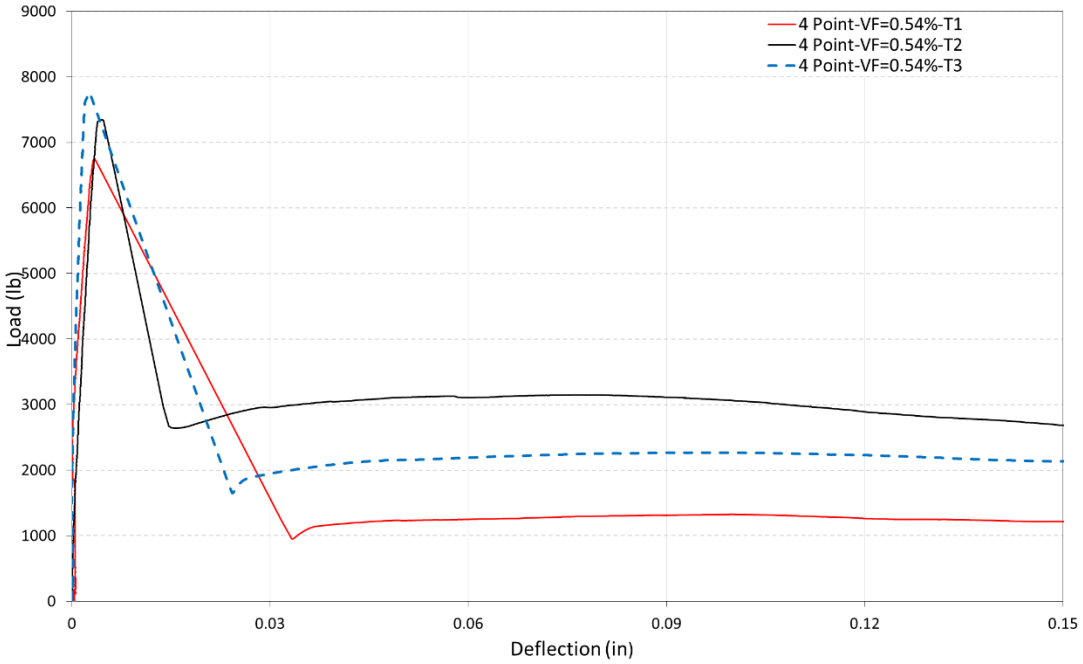

Figure 2-28 Load vs Deflection for 4-Point bending – VF=0.54%

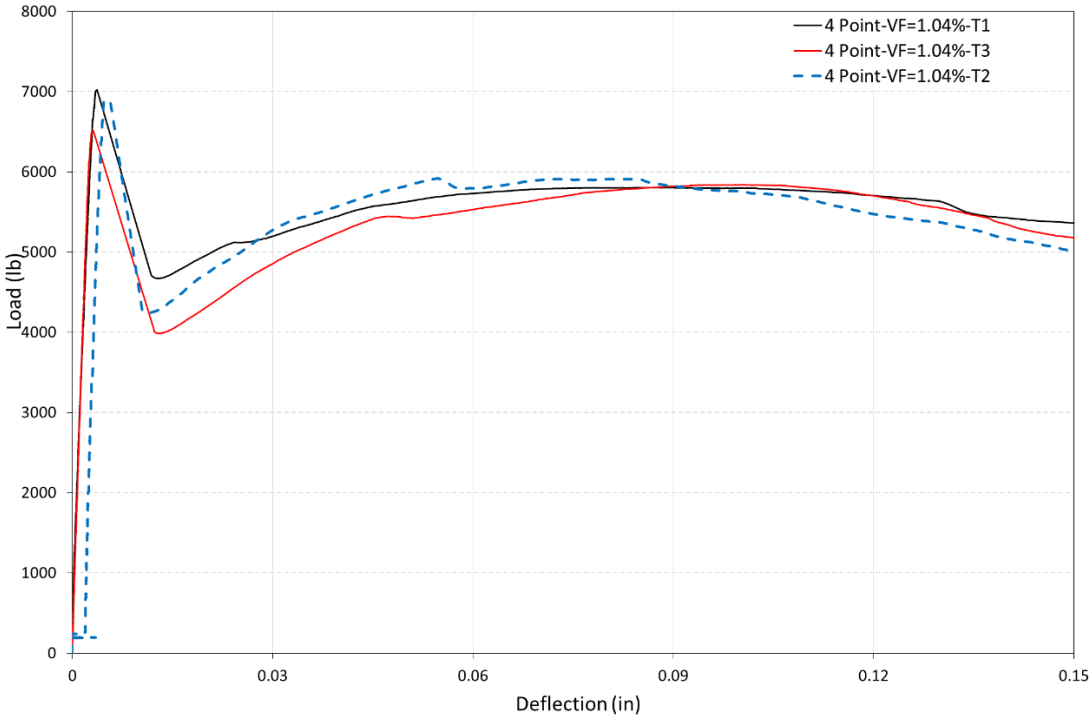

Figure 2-29 Load vs Deflection for 4-Point Bending – VF=1.04%

Synthetic FRC beams under 4-point bending showed the same trends as were seen for the 3-point bending tests. The load-deflection response consisted of three stages, including elastic, sudden jump, and drop of load bearing due to initiation of the crack, and a post-crack residual capacity or hardening state. However, since there was no notch in the case of the 4-point bending, there was no weak section. Therefore, the location of the crack was unknown.

The loading condition of the 4-point bending test caused the middle one-third of the beam to have a maximum value and uniform bending stress prior to crack initiation. These characteristics led to the peak load being much higher than in the case of the 3-point bending test for both fiber volume fractions.

Uniform stress distribution in the middle one-third of the beam led to crack initiation at the weakest section. In all the tests performed for 0.54% fiber volume fraction, one macro crack formed and propagated up to the top of the beam. Cracking was more complicated in case of 1.04% fiber volume fraction. Two of the tests presented one macro crack initiation, but in one test, it propagated into multiple cracks when moving toward the top of the beam.

Results for peak load of the beams under the 4-point bending test present more variation than those of the 3-point bending tests. However, the average maximum value between the two fiber volume fractions did not vary significantly.

As it was observed for 3-point bending test results, crack initiation led to an initial drop and displacement jump immediately after the crack. Fiber volume fraction of 1.04% presented significantly less initial drop of load bearing compared to the 0.54% fiber volume fraction. As was explained for the 3-point bending case, this variation was due to the earlier interaction of fibers because of their higher concentration for 1.04% volume fraction.

Initial drops also varied among the test results of the same fiber dosage. Different fiber orientations and fiber distributions throughout the cracked section were the main reasons for these variations. There was less variation among the test results for the fiber dosage of 1.04%. This can be explained by more uniform distribution of fibers in the beam section due to a larger amount of fibers added to the mixture. The same reasoning can be used to explain the fewer variations in the hardening behavior of the beams with higher fiber.

The hardening state was more resonant in the beams with higher fiber volume fraction (VF=1.04%). This state is controlled by the fibers' bridging effect, as explained earlier. Higher residual loads increased the area under the load-displacement curve. This can be translated as more energy absorption of the beams with higher fiber volume fraction, which results in more ductile behavior of the members.

Experimental tests suggest that the flexural post-crack behavior of the synthetic FRC beams are mainly controlled by the bridging effect. Investigation of the beam sections after total failure (Figure 2-30) suggests that the fibers' failure was mainly in the form of pull out. Therefore, fibers do not deform up to their yielding capacity. This emphasizes the importance and effect of synthetic fibers and their bonding with a concrete matrix.

Figure 2-30 Beam Section after Total Failure (VF=1.04 %)

Standard test method of ASTM C1609/C 1609M – 12 [96] propose the first peak strength to be calculated by the Equation 2-3:

$$f = \frac{PL}{bd^2}$$

Equation 2-3

Where:

f = the strength (psi)

P = the peak load (lb.)

b = the average width of the specimen at the fracture, as oriented for testing (in)

d = the average depth of the specimen at the fracture, as oriented for testing (in)

L= span length (in)

Table 2-4 shows the first peak strength for 4-point bending tests.

Table 2-4 First peak strength for 4-point bending tests

Volume Fraction	L (in)	b (in)	d (in)	Test	P (lb.)	f (psi)	Avg.f(psi)
0.54%	18	6	6	T1	6712	559	606
				T2	7340	612	
				T3	7765	647	
1.04%	18	6	6	T1	6501	541	567
				T2	6892	574	
				T3	7020	585	

2.8 Two-Dimensional DIC Analysis

The two-dimensional DIC method provides the capability to perform post-processing analysis. Two-dimensional DIC analysis provides the deformation field for the region of interest specified by user. The region of interest was chosen based on the location of the crack. Two-dimensional DIC analysis was performed using 2D GOM Correlate software [101]. In the validation study of the 2D DIC method 7D, software developed by Vacher et al [102] was also used to compare the results obtained with two different software. Default values of 19 pixels for facet size and 16 pixels for point distances were used. The pattern quality of the surface was checked to ensure that I had sufficient grey level intensity. Figure 2-31 shows the region of interest (surface component) and grey intensity level of the surface pattern for a typical 3-point bending test. It is desired to have a peak intensity in the green level.

Two-dimensional DIC analysis requires the user to introduce a reference image. All of the calculations are based on the comparison of each stage with the reference image, and the software requires the introduction of a reference scale. Calculated deformations are scaled based on the reference scale, which can be a known as a “real world” dimension of any object in the image field of view. For this purpose, a scale was introduced to the software. ($1\ pix\ \approx 0.09\ mm (0.0035\ in)$)

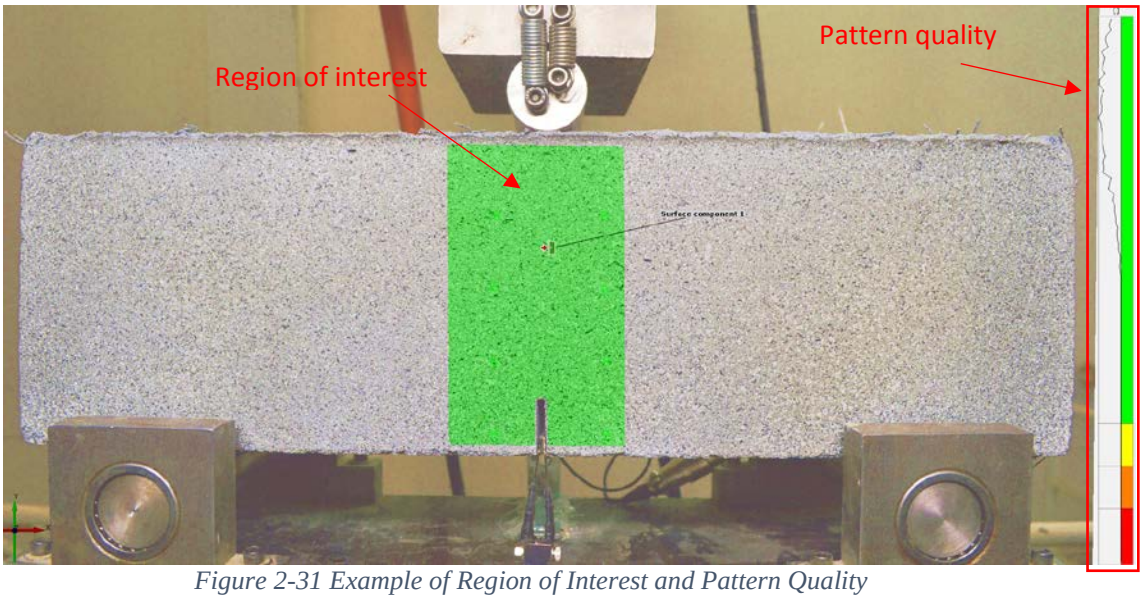

Figure 2-31 Example of Region of Interest and Pattern Quality

The deformation field of the horizontal displacement was calculated for the purpose of crack measurement. Figure 2-32 shows the deformation field at the onset of cracking for the 3-point bending test.

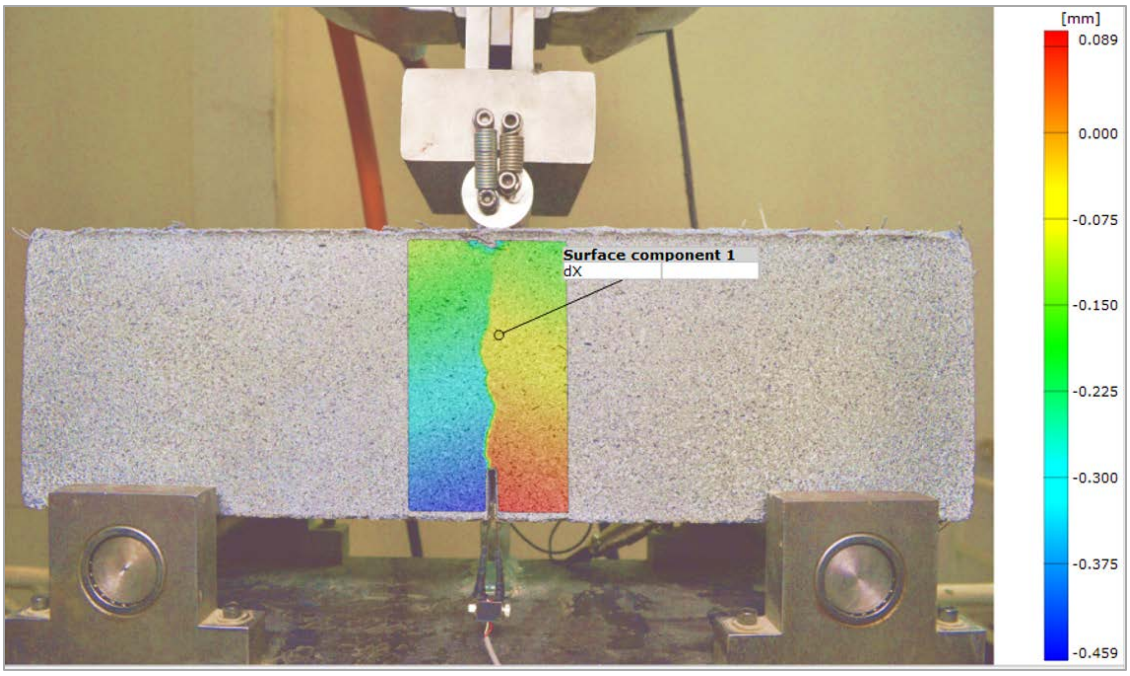

Figure 2-32 Deformation Field at the Onset of Cracking for 3-Point Bending Test

Based on the deformation field, crack width can be obtained by calculating the relative horizontal displacement of points across the crack surface. Since plastic strain in concrete material is significantly small, all of the post-crack deformation of points across the crack surface is due to the crack displacement. Therefore, relative displacement of the points across the crack surface can be translated as the crack width. By utilizing the 2D DIC method, crack specifications can be obtained at any stage of the experiment and along any point of the crack length (Figure 2-33 and 2-

34).

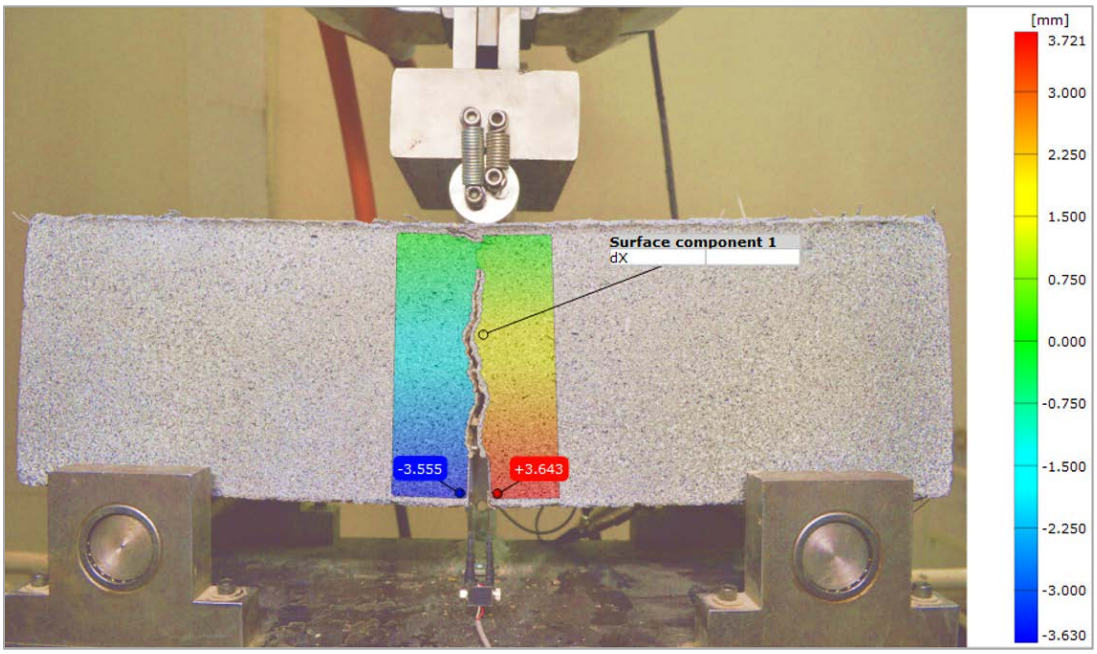

Figure 2-33 Horizontal Displacement of the Points across the Crack Surface

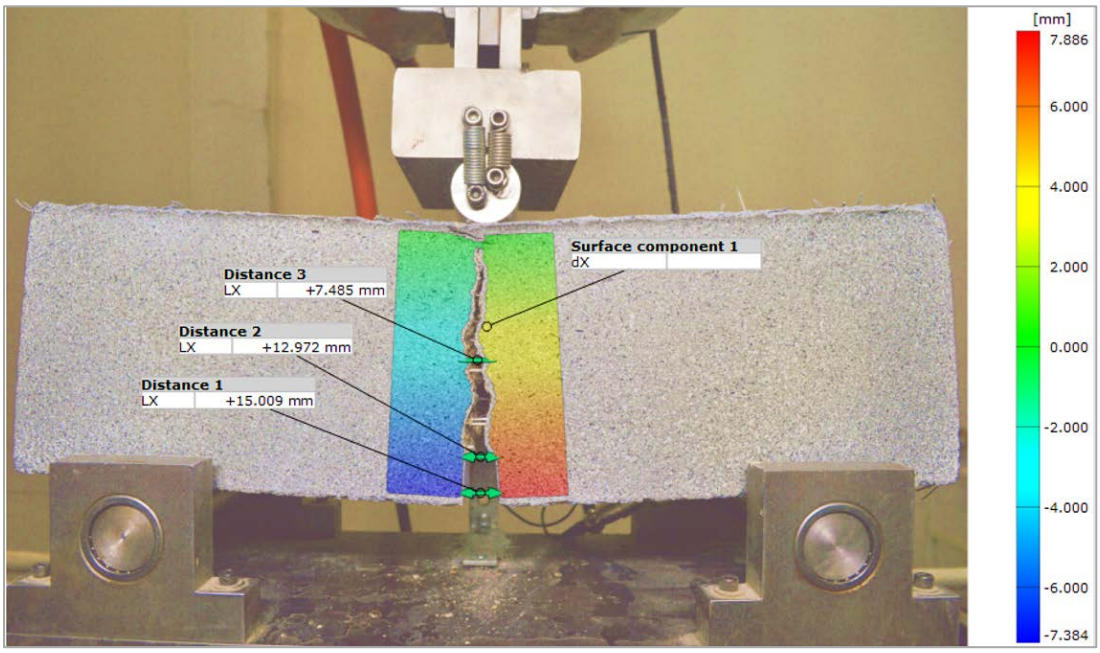

Figure 2-34 Crack Width Calculation based on the Relative Horizontal Displacement of Points across the Crack Surface (DIC validation test- synthetic FRC VF=0.54%)

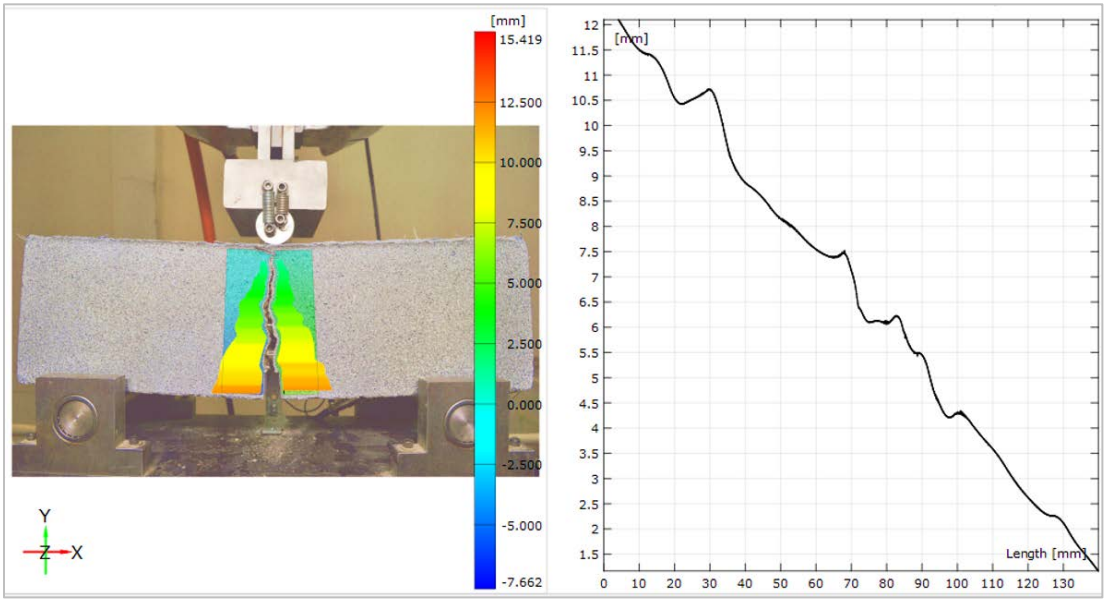

Figure 2-35 Crack Width Vs Specimens' Height at a Given Instance during the Test (DIC Validation Test - Synthetic FRC VF=0.54% - t=1950 s)

2.8.1 Two-dimensional DIC Crack Measurement Validation Test Results

Two-dimensional DIC analysis was performed on the three beams subjected to 3-point bending tests. During the test, crack mouth opening displacement (CMOD) was obtained with a clip gauge transducer. Crack widths at the bottom of the notch (clip gauge location) were calculated with the DIC method (Figures 2-37, 2-39 and 2-41).

Figures 2-36, 2-38 and 2-40 show DIC analysis of the crack width at end of each test. Crack widths were obtained using 2D DIC analysis. Two different software were utilized, and the results were compared with the results of the clip gauge transducers.

As is presented in the graph of Figure 2-41, the transducer was out of range and stopped working at a maximum CMOD value of 0.35 in. CMOD obtained through the 2D DIC method can measure values much higher than the transducer range. CMOD was obtained up to the end of the

test and at a value 0.61 in. for the synthetic FRC beams (Figure 2-40).

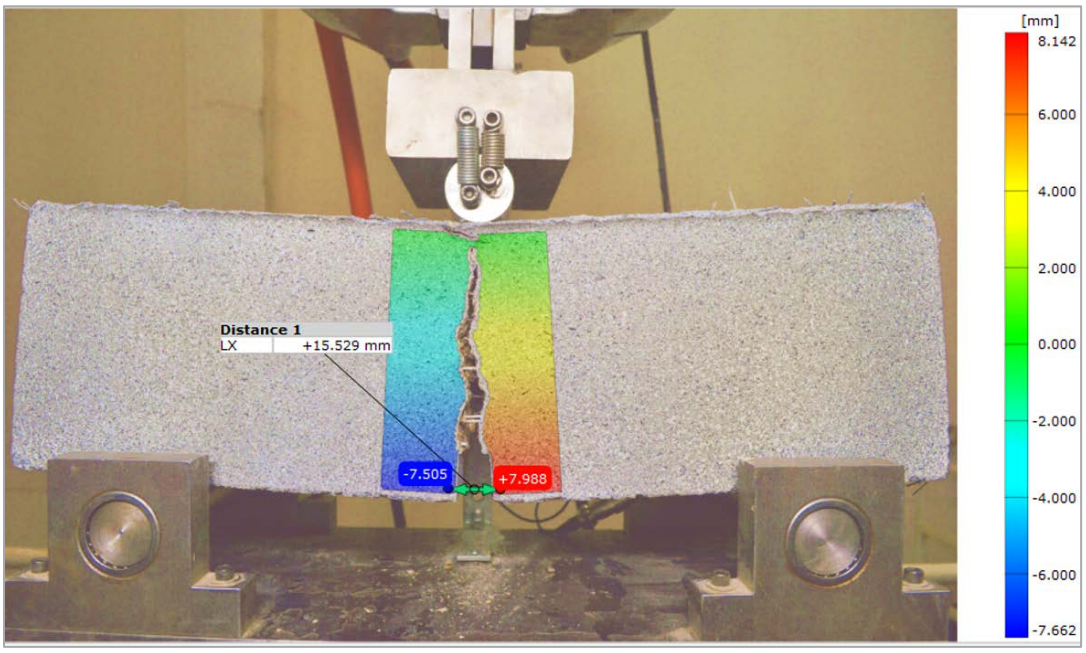

Figure 2-36 Crack Width Obtained by 2D DIC Analysis, Synthetic FRC VF=0.54%-CMOD= 0.61 in (t=2400s)

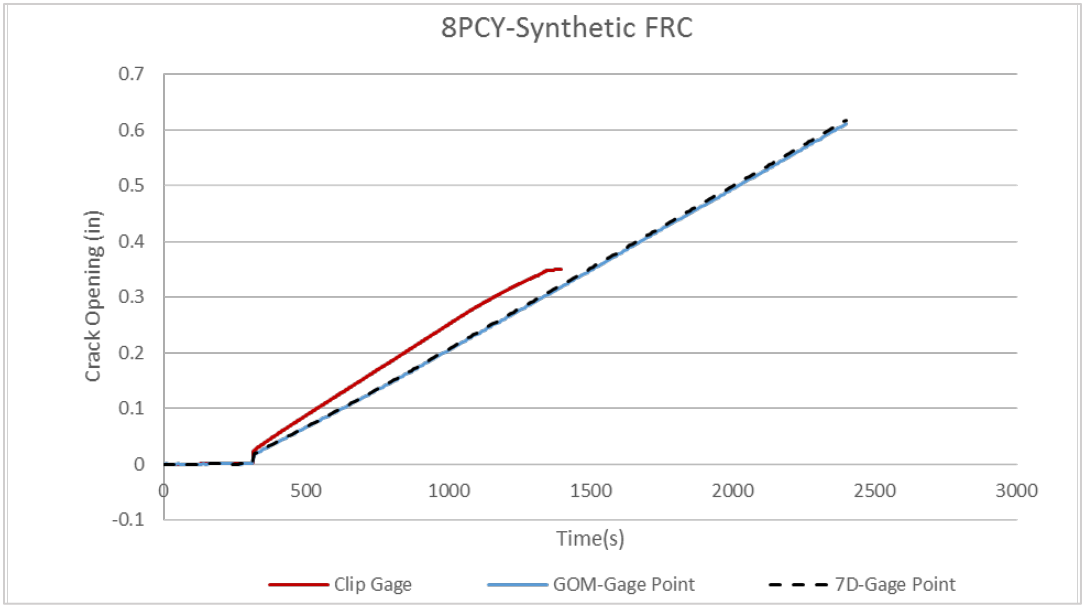

Figure 2-37 Crack Width by 2D DIC vs Clip Gauge, Synthetic FRC VF=0.54%

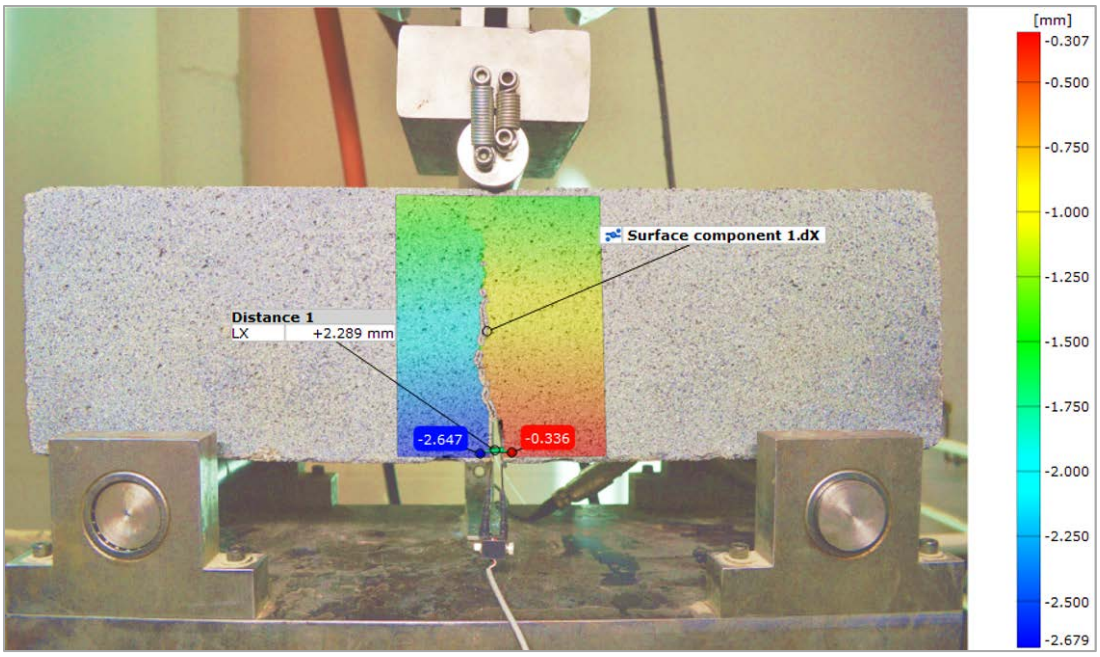

Figure 2-38 Crack Width Obtained by 2D DIC Analysis, Geopolymer RC VF=20% (t=1400s)

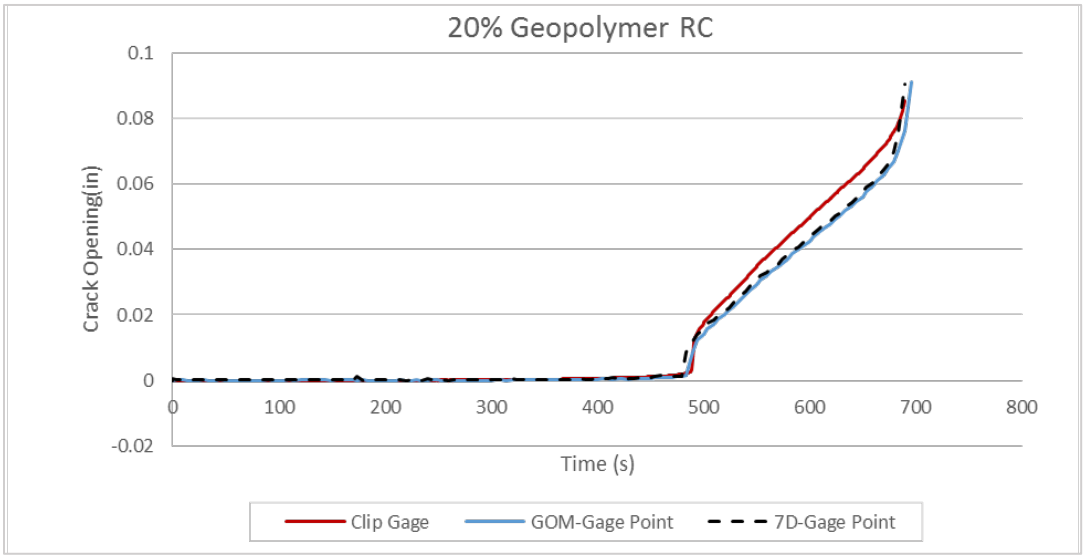

Figure 2-39 Crack Width by 2D DIC vs Clip Gauge, Geopolymer RC VF=20%

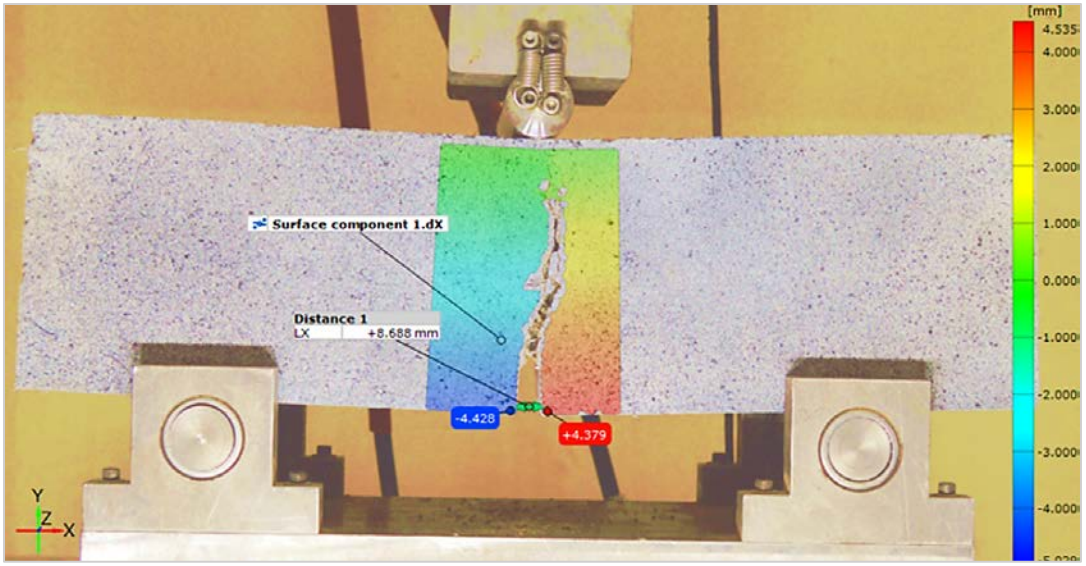

Figure 2-40 Crack Width Obtained by 2D DIC Analysis, Steel FRC VF=0.33% (t=1450s)

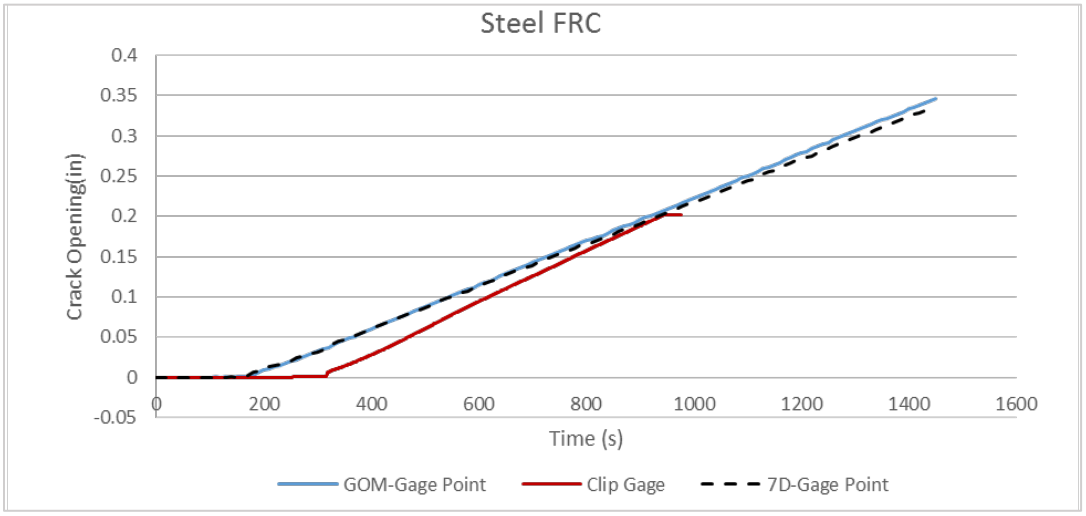

Figure 2-41 Crack Width by 2D DIC Compared with Clip Gauge, Steel FRC RC VF=20%

Crack mouth opening displacements (CMOD) calculated by 2D DIC, when compared to the clip gauge results, showed a good compatibility with the trend and rate of the crack opening. Values of CMOD obtained for the steel FRC beam (Figure 2-41) showed that the 2D DIC is capable

of earlier detection of the cracks. Neither software used for the 2D DIC analysis showed major variations in the CMOD results.

In addition to verification of the 2D DIC crack width by comparing it with clip gauge transducer, for some of the tests, crack width was also measured with a crack ruler. There was good agreement between the 2D DIC method and manual measurement. Figure 2-42 shows an example of the comparison of the manual measurement and the 2D DIC method for the 4-point bending test.

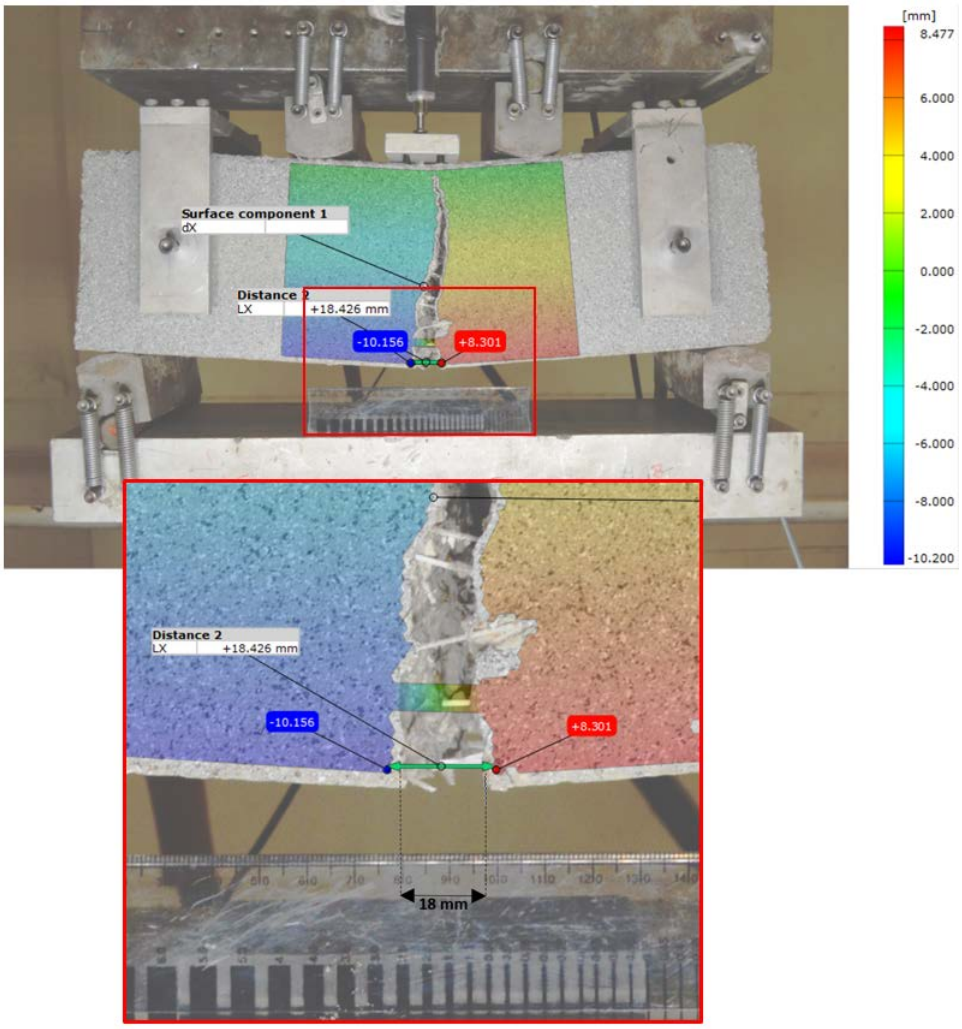

Figure 2-42 Crack Width: DIC vs Crack Ruler

2.8.2 Two-Dimensional DIC Crack Width Analysis for Flexural Tests

As was presented in the validation section, application of 2D DIC for crack width measurement can increase some of the limitations of crack measurement by transducers. With the 2D DIC technique, crack width data can be obtained up to total failure. The standard test method of RILEM [88] recommends a final CMOD of 3.5 mm (0.14 in). In the current study, the test results for the load CMOD responses were reported up to a CMOD of 0.2 in.

2.8.2.1 Crack Width Analysis of 3-Point Bending Tests

Due to the existence of notches, all tests presented a single crack starting from the tip of the notch (Figure 2-43 and 2-44). Load–CMOD responses for 3-point bending tests for two volume fraction (VF) of synthetic FRC were calculated using the 2D DIC method and GOM correlate [101] software (Figures 2-45 and 2-46).

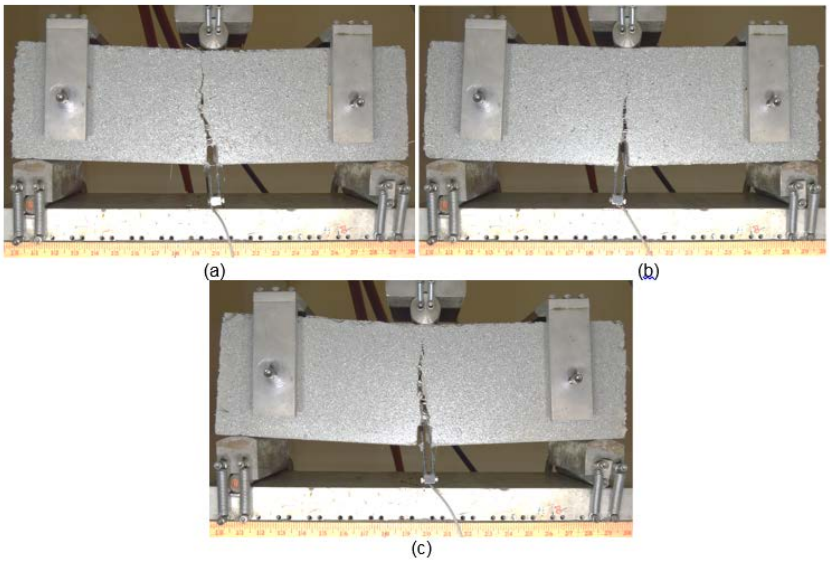

Figure 2-43 Crack Propagation in 3-Point Bending Test of VF=0.54%: (a) Test 1 (b) Test 2 (c) Test 3

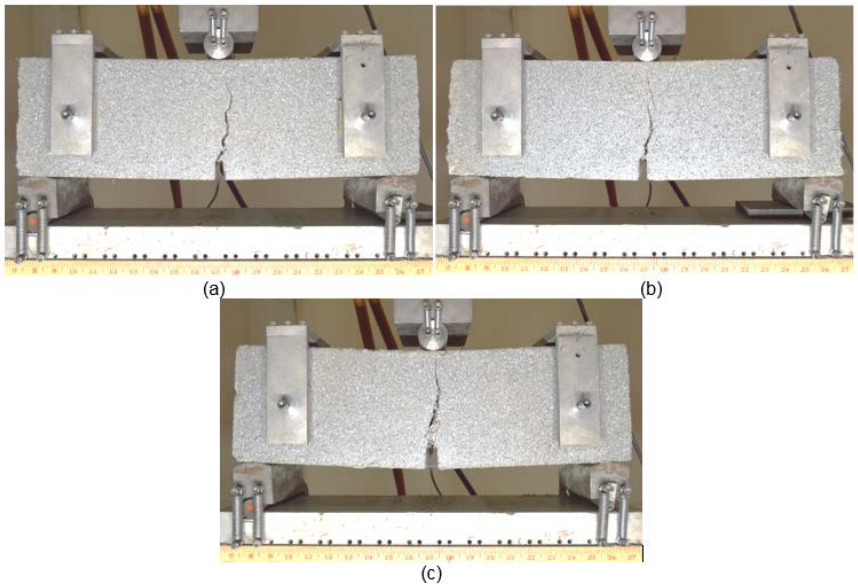

Figure 2-44 Crack Propagation in 3-Point Bending Test of VF=1.04%: (a) Test 1 (b) Test 2 (c) Test 3

Two points across the cracks were selected at the same height (0.3 in from the bottom of the beam). This selection was done to make sure that the maximum value of CMOD was obtained and to avoid calculation errors at the edges of the analysis region. As is presented in the curves, the notch opening was almost zero at the elastic part. After the initiation of the first crack, a sudden crack displacement occurred simultaneously with a drop of the load bearing capacity. This initial drop was less in the case of the1.04% fiber volume fraction compared to the 0.54%. This suggests earlier interaction of fibers in higher fiber volume fractions.

After the initiation of the crack and first drop, both fiber volume fractions presented a hardening state. All three tests for each volume fraction presented the same initial crack displacement, but the hardening state varied. This hardening variation can be explained by the effect of fiber orientation. In the case of the 3-point bending test, the location of the crack was predefined; however, random fiber orientation in the crack surface section leads to a different level of residual hardening.

The residual load bearing was again clearer in the case of the 1.04 fiber volume fraction. The same crack opening requires more force in the case of 1.04% synthetic fiber volume fraction compared to the 0.54%. By considering the random distribution of fibers in the mixture, this phenomenon can be explained by a higher probability of the fibers orienting perpendicular to the crack surface and more fibers bridging the crack.

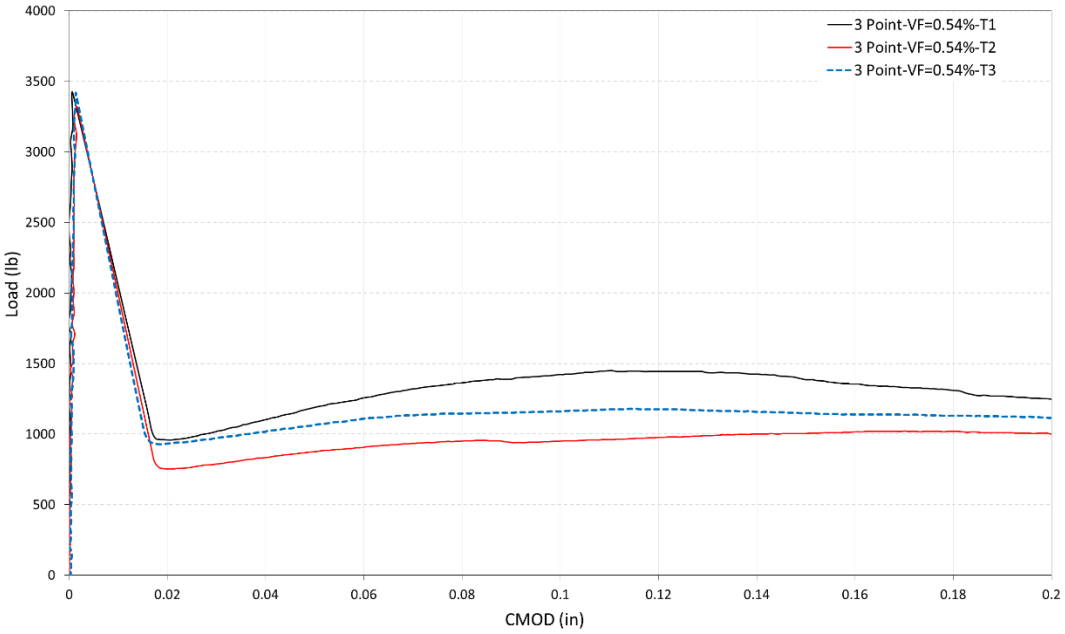

Figure 2-45 Load vs CMOD for 3-Point Bending – VF=0.54%

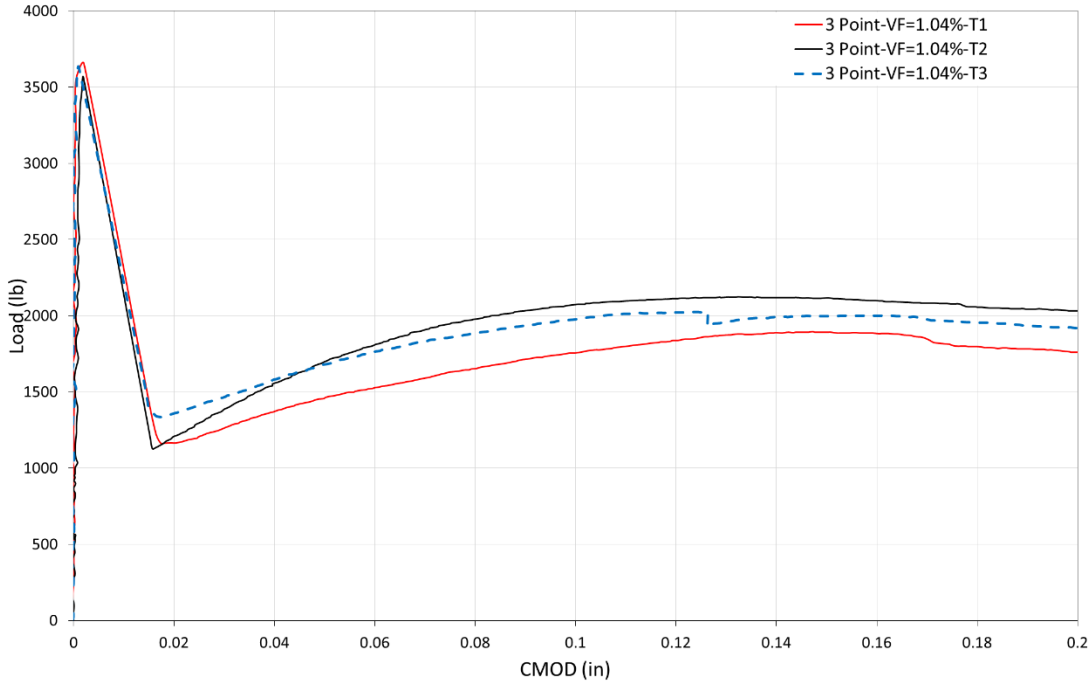

Figure 2-46 Load vs CMOD for 3-Point Bending – VF=1.04%

Figure 2-47 and 2-48 shows the analysis result for two of the 3-point bending tests at CMOD=0.2 in.

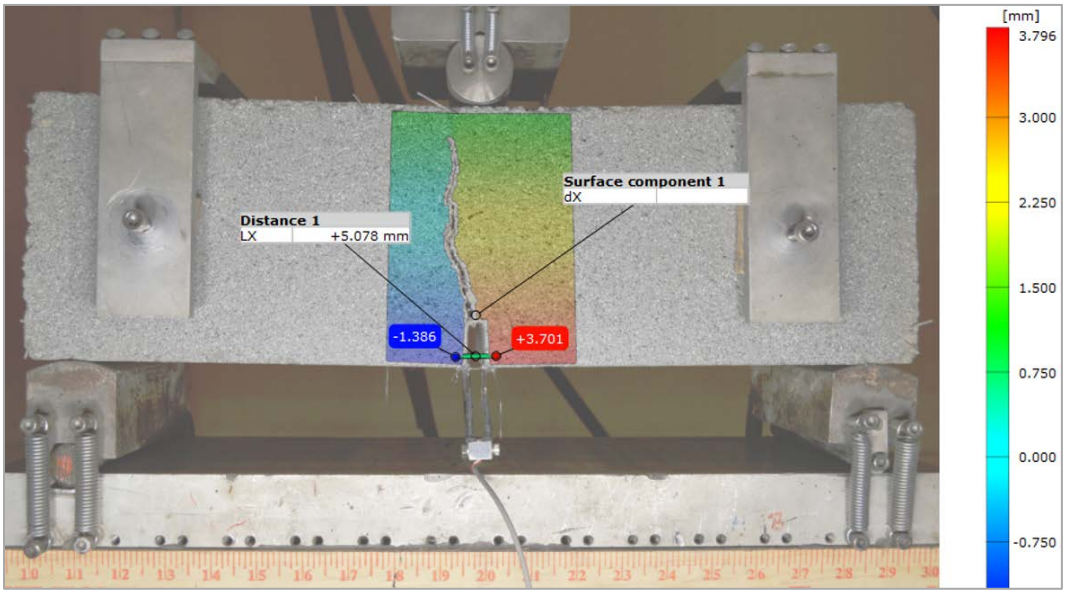

Figure 2-47 Three-Point Bending –VF= 0.54% - T1 - CMOD=0.2 in

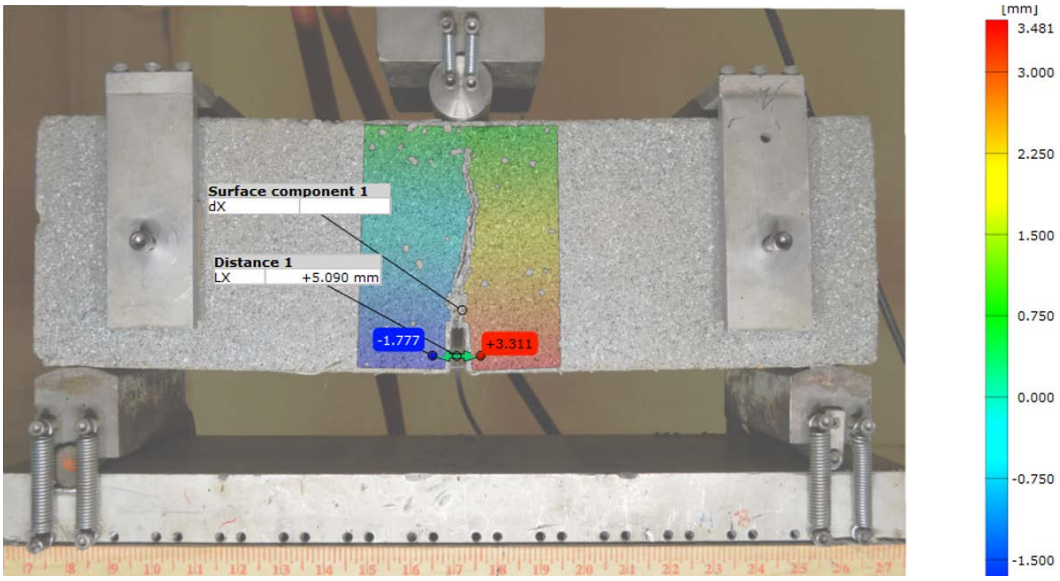

Figure 2-48 Three-Point Bending –VF=1.04% - T3 - CMOD=0.2 in

2.8.2.2 Crack Width Analysis of 4-Point Bending Tests

The load/CMOD response for 4-point bending tests of two volume fractions (VF) of synthetic FRC was calculated using 2D DIC method and GOM correlate [101] software. In all cases, only a single macro crack was propagated toward the top of the beam specimens. However, since there was no notch in the case of 4-point bending, the location of the crack was unknown (Figures 2-49 and 2-50). The post-processing capability of the 2D DIC method makes it possible to find the location of the crack from the last image and then calculate the deformation of the points across the crack section from the beginning of the test. In order to be consistent, the CMOD measurement points across the cracks were selected at the same height (0.3 in from the bottom of the beam) as was selected for the notched beams for 3-point bending tests. Figures 2-51 and 2-52 show the analysis results for crack width in 4-point bending tests versus total loading.

As was mentioned for the load-deflection test results of beams under 4-point bending, uniform stress distribution in the middle one-third of the beam leads to crack initiation at the weakest

section. In all the tests performed for 0.54% fiber volume fraction, one macro crack was formed and propagated to the top of the beams (Figure 2-49)

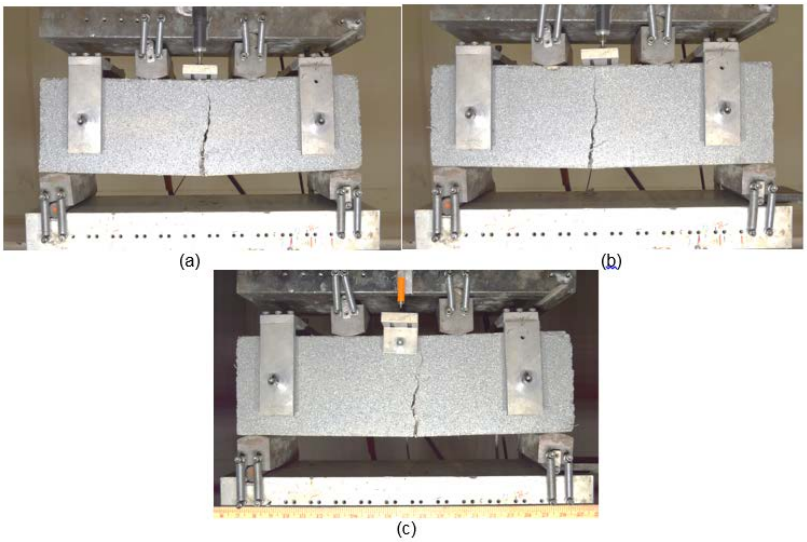

Figure 2-49 Crack Propagation in 4-Point Bending Test of VF=0.54%: (a) Test 1 (b) Test 2 (c) Test 3

Cracking was more complicated in the case of 1.04% fiber volume fraction. In two of the tests, one macro crack was initiated, but in one test, it propagated into multiple cracks. In one case, two major macro cracks were observed (Test #2). One macro crack started, but merged into another crack initiated a few seconds later and formed a final macro crack (Figure 2-50 [b]). Crack measurement for this section was in the form of maximum crack opening. For the case of the beams which presented multiple cracking, total crack displacement or the sum of the both crack widths was calculated as the CMOD.

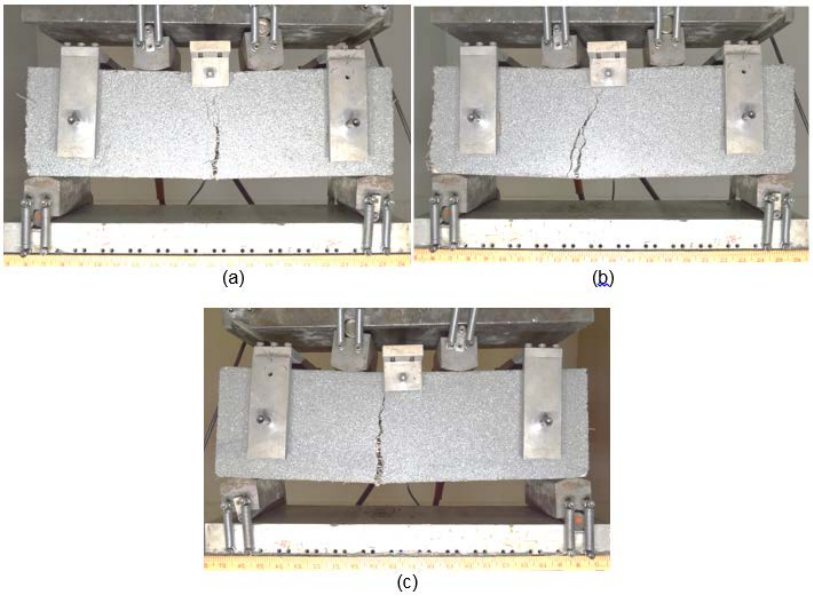

Figure 2-50 Crack Propagation in 4-Point Bending Test of VF=1.04 %: (a) Test 1 (b) Test 2 (c) Test 3

The crack width opening was almost zero until the maximum load was reached. After the initiation of the crack, a sudden crack displacement occurred alongside a drop of the load-bearing capacity. As in the case of the 3-point bending, the initial drop was less for the 1.04% fiber volume fraction than for the 0.54%. The difference in drop was much higher in the 4-point bending results compared to the 3-point bending test results. This again suggests the earlier interaction of fibers in higher volume fraction of fibers.

After the initiation of the crack and first drop, both fiber volume fractions presented a hardening state. This residual load bearing was clearer in the case of the 1.04 fiber volume fraction. For volume fraction of 0.54%, fibers acted mainly by controlling the crack opening with an almost constant state of load. In the case of 1.04% fiber volume fraction, curves presented a clear hardening state, at which the load capacity tended to increase almost up to the first peak load, while the crack width increased.

As for the 3-point bending tests, the crack width opening requires more force in the case of 1.04% synthetic fiber volume fraction compared to the 0.54%. The extra number of fibers increases the probability of the fibers orienting perpendicular to the crack surface, and the fiber bridging is more resonant.

Unlike the notched beams under 3-point bending, in 4-point bending tests the location of crack is not predefined. Before the crack initiation, the region between the loading points have the same amount of bending stress distribution. This uniform distribution of tensile stress causes the crack to initiate at the weakest section of the middle one-third of span.

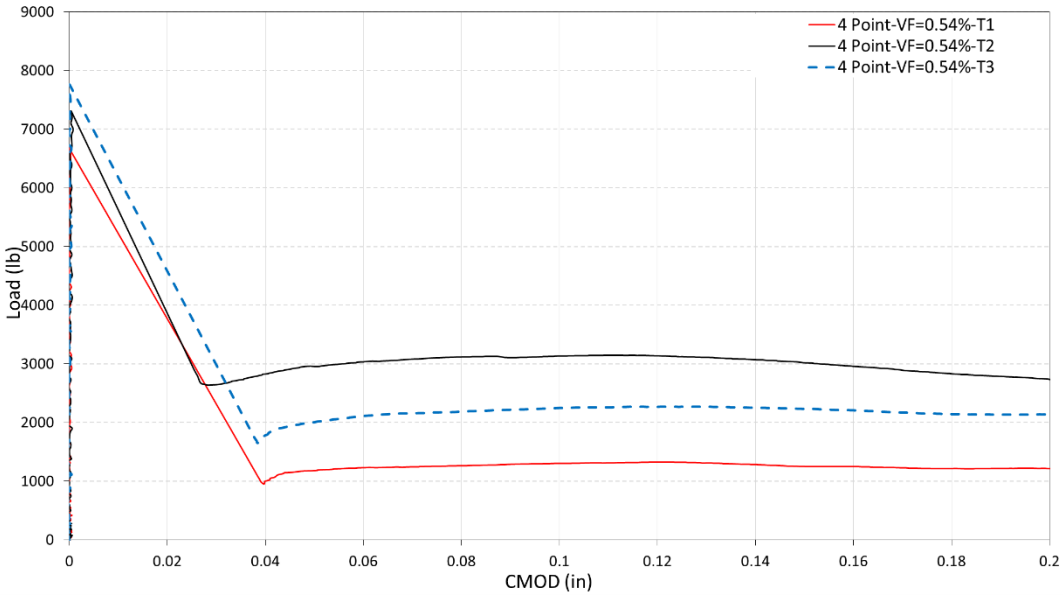

Figure 2-51 Load vs CMOD for 4-Point Bending –VF= 0.54%

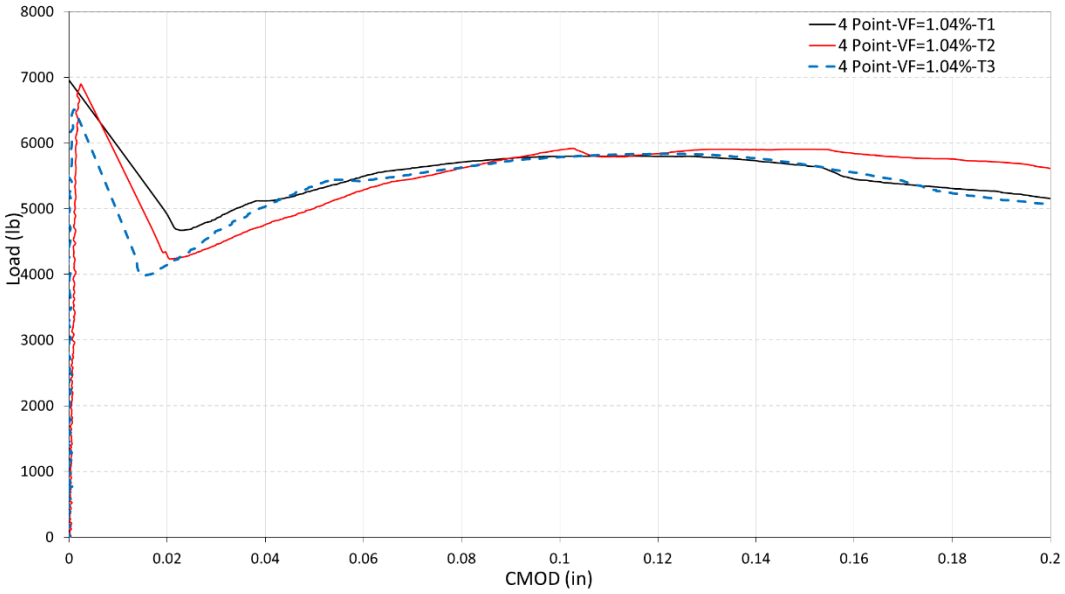

Figure 2-52 Load vs CMOD for 4-Point Bending –VF= 1.04%

Figure 2-53 and 2-54 shows the analysis result for two of the 3-point bending tests at CMOD=0.2 in.

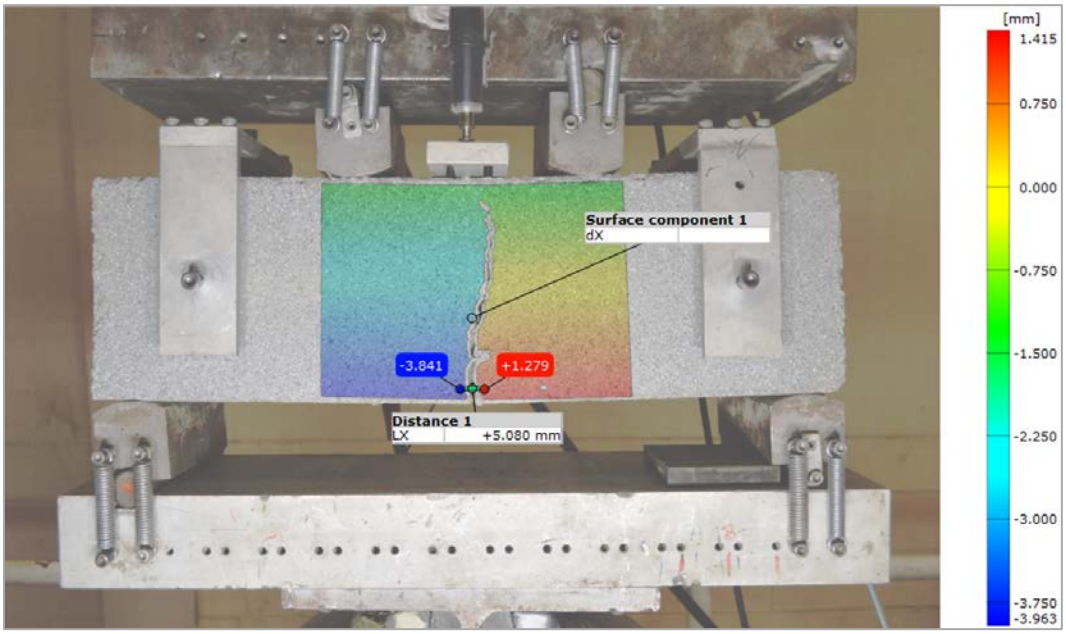

Figure 2-53 Four-Point – VF=0.54% - T1 - CMOD=0.2 in

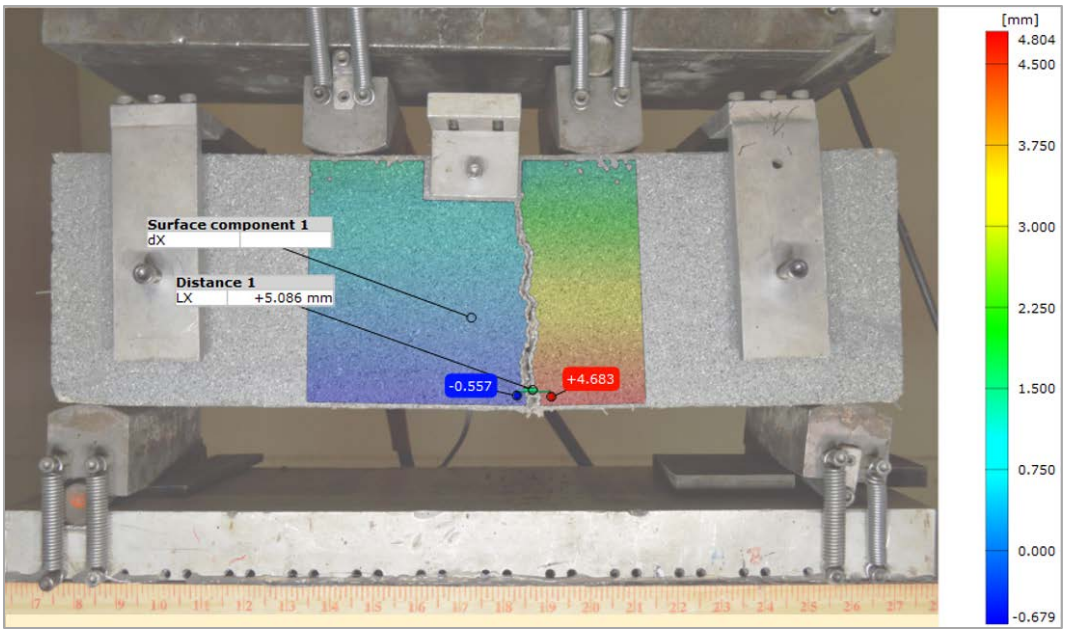

Figure 2-54 Four-Point – VF=0.54% - T3 - CMOD=0.2 in

2.8.3 Crack Propagation

The two-dimensional DIC method has the capability of calculating the surface deformation at any point of the region of interest. Consequently, by using 2D DIC, it is possible to obtain crack data at any point of the specimen's surface. Thus it is possible to investigate the crack propagation during the test.

Figure 2-55 shows the average crack width data along the specimen's height for three tests performed for each load condition and fiber volume fraction. Crack width data is presented at various mid-span deflections and their corresponding loadings. The first curve with the smallest deflection in each figure represents the value of crack width immediately after the crack is initiated.

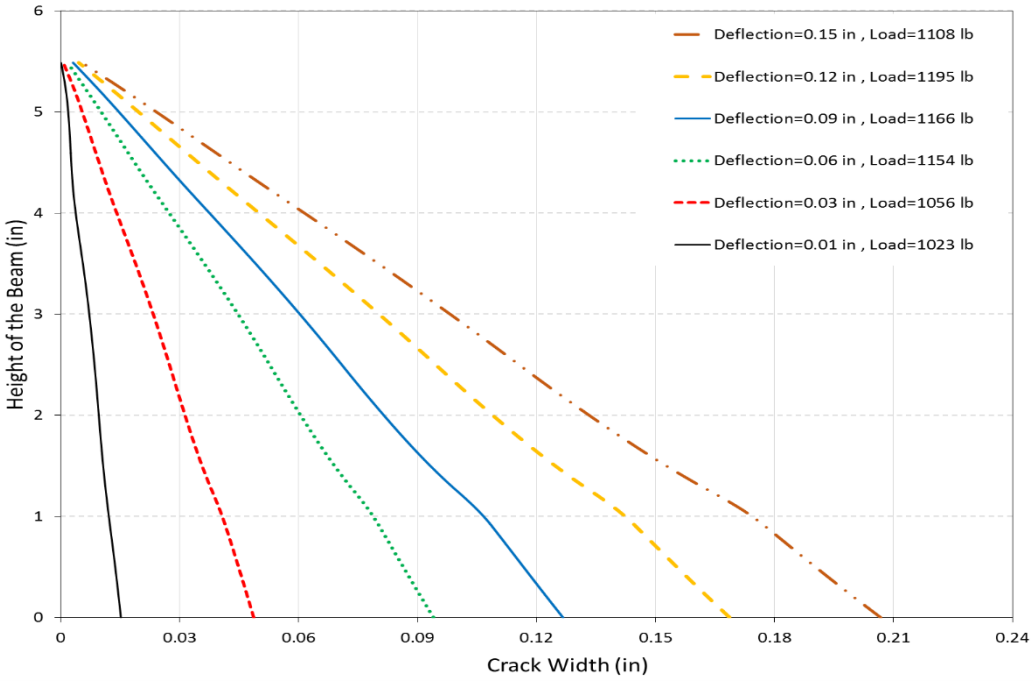

Figure 2-55 Crack Propagation: 3-Point-VF=0.54%-Average

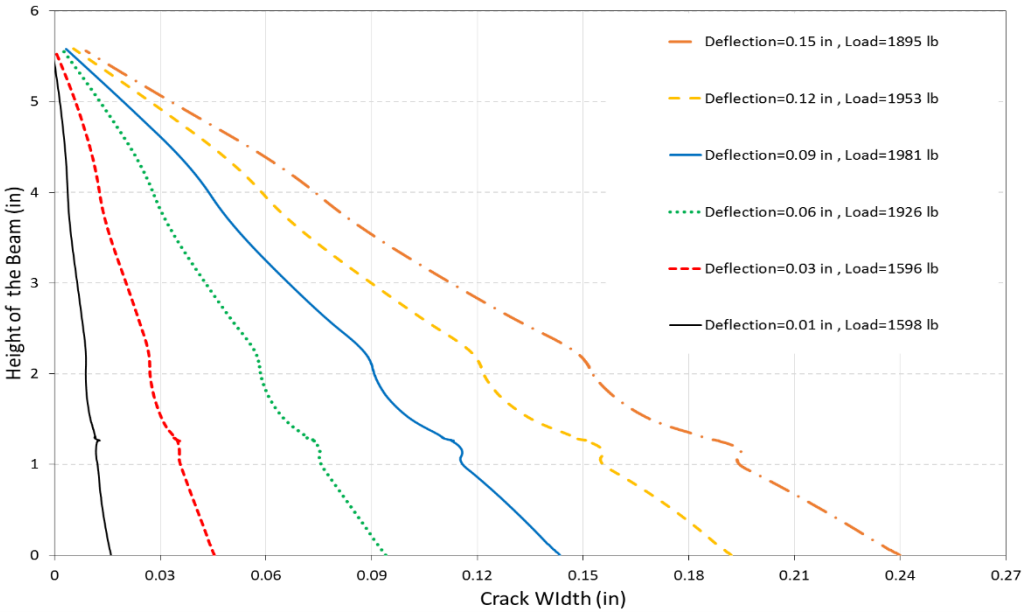

Figure 2-56 Crack Propagation: 3-Point-VF=1.04 %-Average

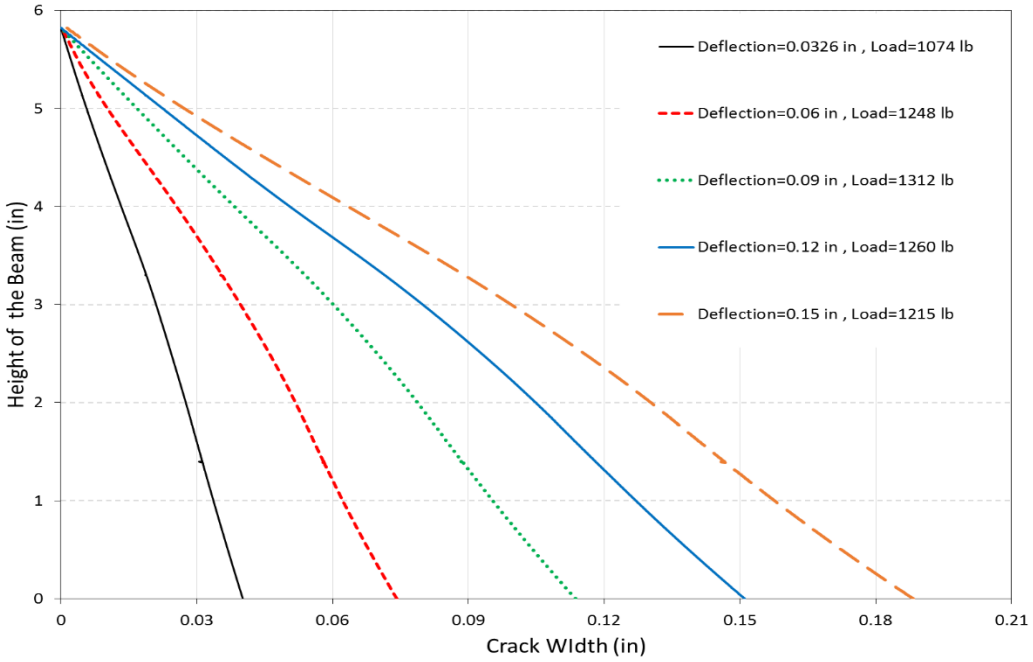

Figure 2-57 Crack Propagation: 4-Point-VF=0.54 %-Average

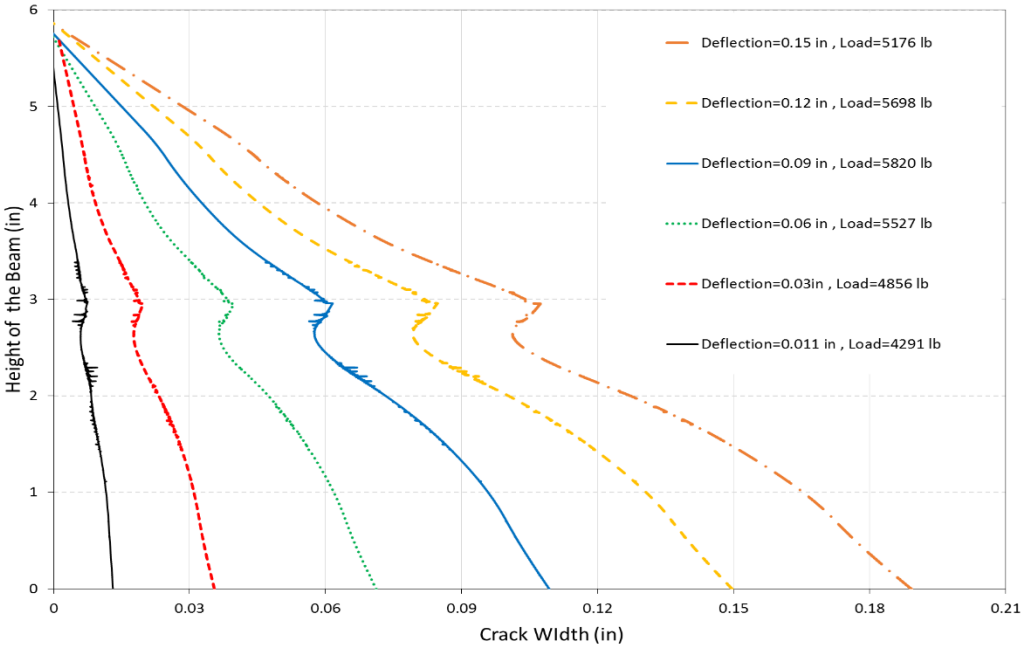

Figure 2-58 Crack Propagation: 4-Point-VF= 1.04 %-Average

Investigation of Figures 2-55 to 2-58 suggests that the crack width propagation occurs at an almost constant rate based on the crack opening at the consecutive deflection values. This observation suggests that after the fibers are engaged, the crack opening will be controlled by the fibers.

Comparison of crack openings for 0.54% and 1.04% fiber volume fractions shows the effect of higher fiber dosage. Higher fiber volume fraction presents smaller values obtained for the crack width at the same mid-span deflections. This observation is more obvious in the case of 4-point bending compared to the case of 3-point bending test. For example, in the case of 4-point bending test, crack width values for 0.54% fiber volume fraction are almost twice that of the 1.04% for the same value of deflection.

Using the same deformation results, it is possible to obtain the crack tip locations with regard to the mid-span deflection. The crack propagates to the top of the beams almost immediately after the crack is initiated. This behavior was observed for both test conditions; therefore, it was not possible to consider the crack tip as the point with a crack width equal to zero. In order to have sufficient data points to obtain the crack tip response, a constant value of the crack width as the criteria representing the critical crack opening was considered. For this purpose, the crack width value of 0.01, as the representative value for the visible crack, was chosen. By this assumption, the crack tip movement was obtained in regard to the deflection (Figure 2-59).

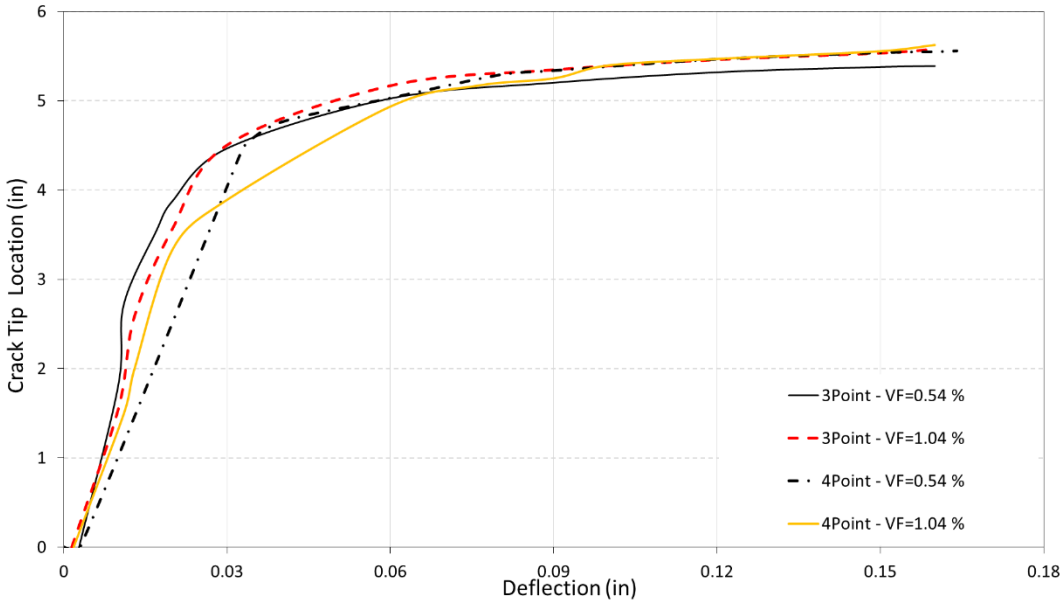

Figure 2-59 Crack Tip Propagation Vs Deflection - Average

As is presented in the Figure 2-59, location for crack width of 0.01inch moves toward the top of the beam as the deflection increases. Initially, the crack tip moves with a steep slope, then slows down as more fibers engage and beams enter the hardening state. This causes the crack tip to move at a lower rate compared to the first stage; hence, the curves continue with lower slopes. Crack tip propagation continues with a small slope until it reaches a plateau state and continues up to the total failure of the beam. This behavior can be observed for both load conditions and fiber volume fractions.

Beams with larger amounts of fibers represent the lower initial slope of crack tip propagation. For example, for the case of beams under 4-point bending, the crack tip reaches the height of 5 inches at a deflection of 0.06 for1.04% fiber volume fraction. The same crack tip location is reached at a deflection of 0.03 in the case of 0.54% volume fraction.

For the case of fiber volume fraction of 1.04% under 4-point bending, crack tip movement starts to slow down as the slope decreases at a relatively smaller deflection values compared to the

0.54%. This behavior suggests that the beam with higher fiber volume fraction represents better crack control that results in a smaller cracked section. This slower crack tip propagation means that at any point during the tests, beams with higher fiber volume fraction have higher cracked moment of inertia (Icr), which increases the moment capacity of the section.

3 Finite Element Method

3.1 Introduction

Numerical investigation of post-crack behavior of synthetic fiber-reinforced concrete was of great interest for this study. One of the main objectives of numerical simulation was to obtain crack width data from the Finite Element Method (FEM) and compare it with the 2D DIC analysis results. For this purpose, accurate FEM modeling of the post-crack behavior was vital. Post-cracking behavior of FRC materials under flexural loading is directly dependent on their tensile behavior. As was extensively discussed in the literature review chapter, post-crack behavior in tension or tension softening of FRC is usually obtained through an indirect method. This indirect method generally provides the tension softening by utilizing the flexural beam test results and performing a numerical iterative method known as inverse analysis. In order to obtain the tension softening curve for two volume fraction of fiber used in this study, the inverse analysis procedure was performed on all 12 beams tested. A concrete damage plasticity model (CDP) in ABAQUS FEM software was utilized to model the beam specimens under 3-point and 4-point bending. A piecewise function was suggested for softening the curve in tension, and a fitting procedure of load-displacement response was performed. Load-CMOD responses of the optimized models were obtained and compared with the experimental load-CMOD obtained through the 2D DIC analysis.

3.2 Finite Element Method Simulation of Post-Cracking Behavior

Fiber reinforced concrete post-crack behavior can be introduced into finite element analysis by different approaches. Smeared crack, cohesive crack [103] or fictitious crack models [104] can be used. The cohesive crack approach requires the crack path to be predefined, and the softening curve directly represents the cohesive force-displacement relationship between the boundary elements of the crack path. The cohesive crack model has more precision when dealing with local cracking behavior, but is not preferable for more practical applications. The smeared crack uses

stress-strain relation and was first introduced by Rashid [105]. In this method, cracks are smeared over the element, and instead of considering a discrete macro crack, the presence of cracks affects the calculation of stresses and material stiffness. The main disadvantage of this approach is mesh sensitivity in the absence of flexural reinforcement [92]. The fictitious crack model, first introduced by Hillerborg [103], provided an energy criterion based on fracture energy concepts. Fictitious crack model material has a linear elastic behavior up to initiation of the crack. After crack initiation, the model assumes a virtual or fictitious crack which the stresses still can transfer across it. These "bridging stresses" are functions of a softening stress-crack opening relation.

In cases of low dosages of fiber, σ-w is most preferable for modeling steel-fiber-reinforced concrete [12]. Also, as mentioned earlier, when there is small flexural reinforcement in the critical regions, the use of the stress-strain softening relationship leads to unreasonable mesh sensitivity [39]. As stresses localize in a few elements, other parts of the structure begin to unload, and further refinement of mesh leads to localization of crack in one element width, eventually resulting in the model failing to converge to a unique answer [106], [107]. Using fracture energy cracking model or σ-w relation is recommended to avoid this problem [130,131]. Hillerborg [103], based on the brittle fracture concepts, defined the fracture energy (Gf) as the energy required to open a unit area of crack. Hillerborg considered fracture energy as a material property, and based on this concept, brittle behavior of concrete is characterized by post failure stress cracking displacement instead of stress strain [108].

Defining the tension softening in the form of stress-displacement assumes that the fracture energy is a material property. Assuming Gf as a material property implies that the relationship between the inelastic part of displacement and stress is fixed. In a case of single crack due to tensile displacement, uck is the displacement normal to crack and does not depend on the specimen length

as long as it is significantly longer than the crack band. Generally, it is about the size of an aggregate [108] (Figure 3-1 and Equation 3-1).

$$u_n^{ck} = u_n - u_n^{el}$$

Equation 3-1

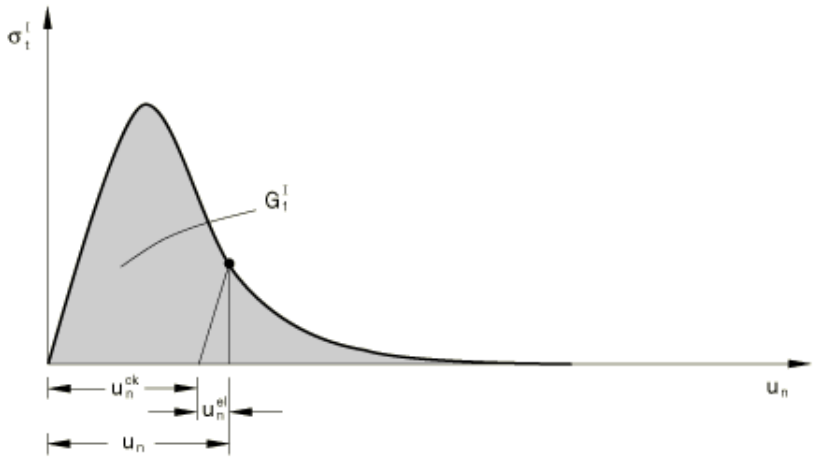

Figure 3-1 Mode I Cracking Behavior based on Fracture Energy [108]

Fracture energy can be calculated as the area under the stress-crack displacement curve (Equation 3-2).

$$G_f = \int \sigma_t \, du_n$$

Equation 3-2

It is worth mentioning that avoiding the mesh sensitivity requires the adoption of a reference length, known as characteristic length (L). This parameter needs to be determined based on the element geometry and integration scheme [108].

In the case of plain concrete simulation with fictitious model, it is often assumed that the stress-crack displacement relationship has a linear function (Figure 3-2).

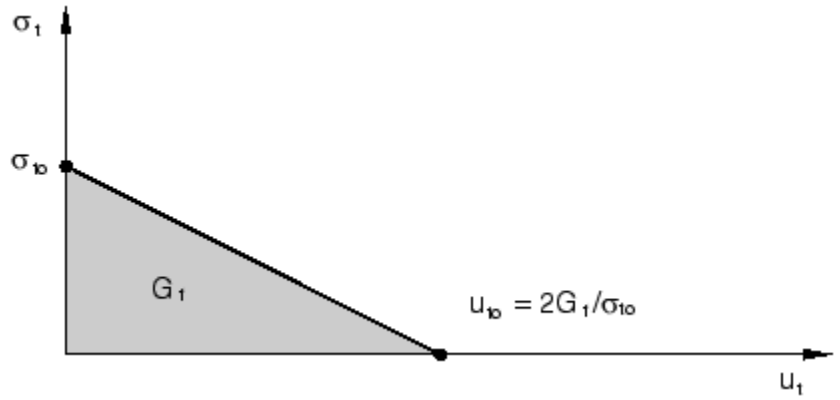

Figure 3-2 Stress-Crack Width and Fracture Energy for Plain Concrete [108]

On the other hand, FRC material behaves differently in tension than plain concrete, and assuming a linear relation for σ-w is inaccurate. FRC stress-crack displacement can be defined with various curves, including bilinear, tetra linear, exponential, etc. (Figure 3-3) [107].

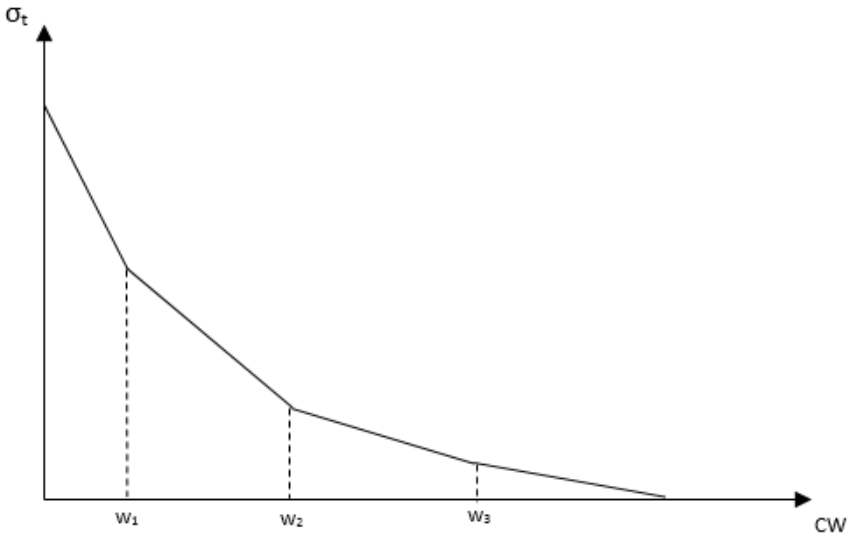

Figure 3-3 Example of Multilinear Post-Failure Stress-Displacement Curve

In this study, it was desirable to simulate the beam tests up to the peak point after the crack was initiated. ABAQUS/CAE software, which was used for this study, allows the definition of tension softening in a tabular form, in as many stages as required. Tensile behavior can be introduced

to the constitutive model by either stress-strain relationship, stress-crack displacement, or yield stress and fracture energy.

The ABAQUS program was utilized for the nonlinear, 3D modeling of flexural beam tests described in the experimental study section. The primary goal of FEM simulation was to obtain the tension softening behavior of synthetic FRC through inverse analysis, and comparison of FEM crack width results with experimental results obtained from 2D DIC analysis.

Among the constitutive models available in ABAQUS, concrete damage plasticity (CDP) and concrete-smeared cracking (CSC) models are capable of simulating concrete materials. Concrete-smeared cracking modeling of monotonic loading is suitable for situations where the confining pressure is less than four or five times the maximum uniaxial compression. In addition, CSC, has some problems with numerical convergence after the concrete cracking point is reached [109], specifically in cases where the whole system starts to unload after the initiation of the crack.

Concrete damage plasticity is a plasticity-based model. Simulation of the inelastic behavior of concrete in CDP is performed by incorporating the isotropic-damaged elasticity with tensile and compressive plasticity. Unfortunately, there is no specific model for simulating the FRC materials. However, the material property of an existing model can be modified to represent the material of interest. Modeling material behavior in CDP is fairly flexible. Tensile and compressive behavior of the concrete material can be introduced to a CDP model in as many stages as required.

Finite element modeling of post-crack behavior for synthetic FRC beams under monotonic loading was of great interest to this research. Due to the limitations of the smeared cracking model in the post-crack region, the use of this approach was not suitable. Thus, the CDP model was chosen to represent the concrete constitutive material

3.3 Concrete Constitutive Model

The concrete damage plasticity model was used for this study and was coupled with a fictitious crack model. Concrete damage plasticity was first introduced by Lubliner et.al [110] to simulate the inelastic tensile and compressive behavior of concrete with the concept of isotropic damage elasticity and plasticity. A concrete damage plasticity model does not have the concept of crack at material integration points. This characteristic of the CDP model is in contrast to models based on the smeared crack approach. The concrete damage plasticity model assumes that the cracking starts at points where the maximum principal strain is positive and the plastic strain is greater than zero [108].

The concrete damage plasticity model is a modification of the Ducker-Prager model. Lubliner et al [110] proposed the yield function to represent the failure state of the concrete materials. In general, the yield function forms a surface in the effective stress space and can represent failure criteria. Yield function in CDP was modified by Lee and Fenves [111]. Equation 3-3 is the definition of yield function in CDP.

$$F = \frac{1}{1-\alpha}(\bar{q} - 3\alpha\bar{p} + \beta(\tilde{\epsilon}^{pl})\langle\hat{\bar{\sigma}}_{max}\rangle - \gamma\langle\hat{\bar{\sigma}}_{max}\rangle) - \bar{\sigma}_c(\epsilon_c^{pl})$$

Equation 3-3

Where $\bar{p}$ and $\bar{q}$ are the hydrostatic pressure stress and von Mises equivalent effective stress respectively. Parameter α is calculated according to the Equation 3-4:

$$\alpha = \frac{\left(\frac{\sigma_{b0}}{\sigma_{c0}}\right) - 1}{2\left(\frac{\sigma_{b0}}{\sigma_{c0}}\right) - 1} \quad and\ 0 \le \alpha \le 0.5$$

Equation 3-4

Where σ_{b0} is the biaxial compressive stress and σ_{c0} is the uniaxial compressive strength.

In the yield function formulation, $\hat{\bar{\sigma}}_{max}$ represent the maximum principal effective stress. Since $\hat{\bar{\sigma}}_{max}$ is in Macauley bracket ($\langle\hat{\bar{\sigma}}_{max}\rangle$) when $\hat{\bar{\sigma}}_{max}$is positive $\beta(\tilde{\epsilon}^{pl})$ appears in the function ($\langle\hat{\bar{\sigma}}_{max}\rangle = \frac{1}{2}(|\hat{\bar{\sigma}}_{max}| + \hat{\bar{\sigma}}_{max})$). β Is obtained according to the Equation 3-5:

$$\beta = \frac{\bar{\sigma}_c(\epsilon_c^{pl})}{\bar{\sigma}_t(\epsilon_t^{pl})}(1-\alpha) - (1+\alpha)$$

Equation 3-5

In the above equation $\bar{\sigma}_c(\epsilon_c^{pl})$ and $\bar{\sigma}_t(\epsilon_t^{pl})$ are the effective compressive and tensile cohesive stresses respectively. In the case of biaxial compression where $\hat{\bar{\sigma}}_{max} = 0$, β is ineffective.

In case of tri-axial compression where $\hat{\bar{\sigma}}_{max}$ is negative, γ appears in the yield function according to the Equation 3-6:

$$\gamma = \frac{3(1-k_c)}{2k_c - 1}$$

Equation 3-6

When the hydrostatic axis is in the deviatory cross section, kk_{ff} is the ratio between the compressive meridian and tensile meridian. This parameter defines the shape of the yield function in the deviatory plane (Figure 3-4).

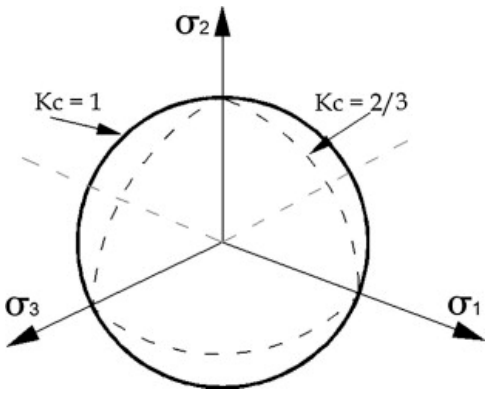

Figure 3-4 Yield Surfaces in the Deviatory Plane (Kc = 2/3 based the Rankine formulation and Kc = 1 based on the Drucker–Prager Criterion). [107]

Figure 3-5 present yield surface under biaxial stress used in the concrete damage plasticity model.

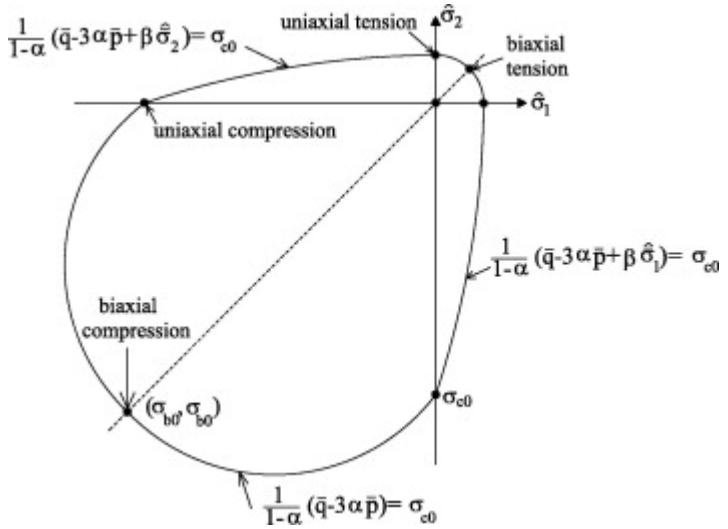

Figure 3-5 Yield Surface under Biaxial Stress used in the Concrete Damage Plasticity Model [11]

A concrete damage plasticity model utilizes the same plastic flow potential surface, G (σ), as the non-associative Ducker-Prager hyperbolic function (Equation 3-8).

$$G(\sigma) = \sqrt{\left(\epsilon \sigma_{t_0} \tan\psi\right)^2 + \bar{q}^2} - \bar{p}\tan\psi$$

Equation 3-7

Where $_\epsilon$ is the eccentricity of the potential surface and is the rate at which the asymptote is approximated for the potential function, and σ_{t0} is the uniaxial tensile stress. ϵ is determined by the ratio of uniaxial tension (σ_{t0}) and uniaxial compression (σ_{c0}) (Figure 3-6).

The potential surface is defined in the p-q plane or meridian plane. Dilation angle or ψ is measured at high confining pressure and is in the same p-q plane as the potential surface. The dilation angle represents the direction of the plastic strain increment vector. Using a non-associative flow rule leads to the plastic strain increment being normal to the potential surface (Figure 3-7).

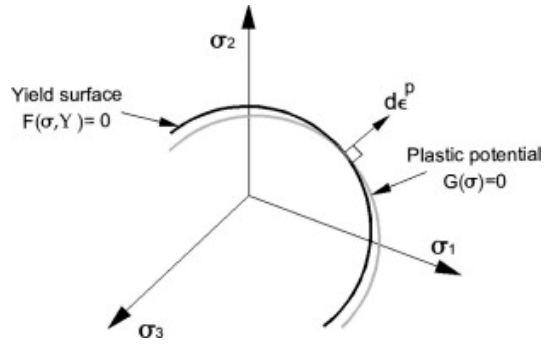

Figure 3-6 Plastic Potential Surface and Yield Surface in the Deviatory Plane [107]

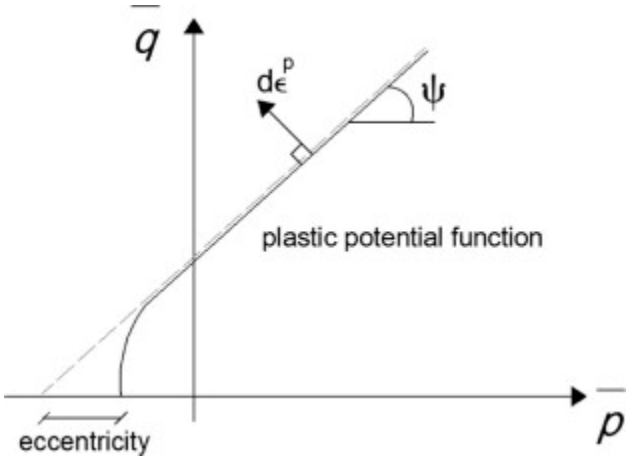

Figure 3-7 Dilation Angle and Eccentricity in Meridian Plane [107]

The degradation of concrete after cracking is incorporated into the CDP model by the damage parameter. The damage parameter, in terms of compression (d_c) and tension ($dt_)$, affects the stress tensor by Equation 3-8:

$$\sigma = (1-d)\bar{\sigma} = (1-d)E_0(\epsilon - \epsilon^{pl})$$

Equation 3-8

Damage parameter is defined with Equation 3-9

$$(1-d) = (1-s_t d_c)(1-s_c d_t)$$

Equation 3-9

Where s_t and s_c are the stiffness recovery in tension and compression.

Parameter μ represents the viscosity, and based on Devaut-Lions' approach can be introduced to incorporate the viscoelastic behavior. Introduction of the μ upgrades the plastic tensor, and damaged parts are removed by adding extra relaxation time. The viscoelastic strain rate can be obtained by the Equation 3-10:

$$\epsilon_v^{pl} = \frac{1}{\mu}(\epsilon^{pl} - \epsilon_v^{pl})$$

Equation 3-10

By the same method dame increment considering the viscoelastic regulation (d_v) is determined by Equation 3-11

$$d_v = \frac{1}{\mu}(d - d_v)$$

Equation 3-11

Stress tensor per viscoelastic model is described with Equation 3-12

$$\sigma = (1 - d_v)E_0(\epsilon - \epsilon_v^{pl})$$

Equation 3-12

3.4 Material Modeling

Synthetic FRC material property was modeled as an isotropic homogenous material. By this approach, the effect of fibers is integrated with the concrete material properties.

3.4.1 Plasticity Parameters for CDP model

Material parameters, including density, modulus of elasticity E0, and the Poisson ratio ν, in addition to the CDP plasticity parameters described in the last section, need to be introduced to the CDP model. The concrete damage plasticity model considers the Poisson's ratio with a constant value for crack and un-cracked concrete. This value was considered as 0.2.

According to [108], the default value of eccentricity is 0.1 ($\epsilon\epsilon$ = 0.1).

Wu et al. [112] and Voyiadjis and Taqieddin [113] recommend 31 to 42 degrees as the range of dilation angle. Based on their recommendation, a dilation angle of 40 was chosen for this study.

Kc is recommended to be more than 0.5, but less than or equal to 1 ($0.5 < Kff \leq 1$). The default value should be 0.667 [108].

Damage parameters were set to zero for both compression and tension behavior. They are more suitable for cases of brittle cracking behavior, whereas synthetic FRC presents a more ductile behavior than plain concrete. A zero damage parameter leads to the consideration of both plastic and inelastic parameters as one. By this assumption, all the inelastic strains would be considered as cracking strain. In dynamic or cyclic loadings, it has been seen that the damage parameters are more important in cases where the unloading needs to be defined by plastic strains [107].

Ratio of biaxial to uniaxial compression ($\frac{\sigma_{c0}}{\sigma_{b0}}$) is recommended to be equal to 1.16 [108].

The ABAQUS manual [108] recommends a value close to zero for concrete viscosity (μ). A value of $\mu = 5 \times 10^{-16}$ was chosen for this study.

Table 3-1 shows a summary of the plasticity parameters used for the CDP model.

Table 3-1 Plasticity Parameters for CDP model

Dilation Angle ψ	Eccentricity ϵ	$\frac{\sigma_{c0}}{\sigma_{b0}}$	K_c	Viscosity v
40	0.1	0.667	1.16	5×10^{-16}

3.4.2 Compression behavior

In a CDP model, compression behavior begins a softening phase after the compressive stress (σc) reaches the failure compressive strength (σcu=fcm) (Figure 3-8). The total compressive strain of a uniaxial compressive test is modeled in CDP by the summation of elastic strain and inelastic strain (Equation 3-13).

$$\tilde{\epsilon}_c^{in} = \epsilon_c - \tilde{\epsilon}_{0c}^{el}$$
$$\tilde{\epsilon}_{0c}^{el} = \frac{\sigma_c}{E_0}$$

Equation 3-13

Where E_0 is the initial modulus of elasticity. In the unloading stage, the CDP model uses the damage parameters in compression, d_c, and they would be used to calculate the stiffness of the damage material. Plastic strain in compression is then calculated by Equation 3-14:

$$\tilde{\epsilon}_c^{pl} = \tilde{\epsilon}_c^{el} - \frac{d_c}{1 - d_c}\frac{\sigma_c}{E_0}$$

Equation 3-14

Plastic strain then can be used to determine the compressive stress (Equation 3-15):

$$\sigma = (1 - d)E_0(\epsilon_c - \tilde{\epsilon}_c^{pl})$$

Equation 3-15

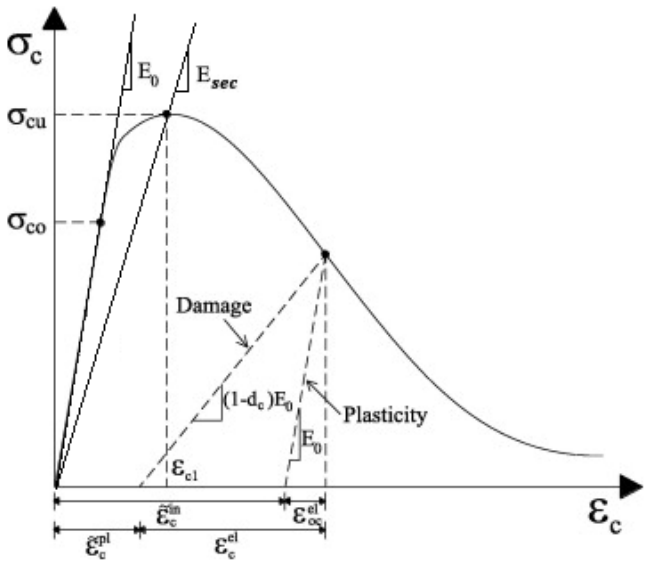

Figure 3-8 Uniaxial Compressive Behavior and Inelastic Compressive Strain in CDP Model [11]

The Hognestad parabola was used as the compression model to introduce the compression behavior into the CDP model. Genikomsou and Polak [107] suggested using the Hognestad parabola for simulation of the steel FRC compressive behavior in ABAQUS.

The stress-strain relationship of the concrete in uniaxial compression can be defined in three stages. The linear elastic part of the model with initial modulus of elasticity of $E_0 = 57000\sqrt{f_c'}$ ends at the stress level of σ_{c0}; this value was assumed to be $0.4f'_c$ [107]. The stress-strain curve is then continued with a nonlinear ascending branch up to maximum compressive load ($\sigma_{cu}=f'_c$) which correspond to the strain of ϵ_0 (Equation 3-16)

$$\epsilon_0 = \frac{1.8f_c'}{E_{sec}}$$

Equation 3-16

Where $f_c' = 0.9f_{cm}'$, rather than the cylinder test, is used to decrease the specimen compressive strength because of compaction, shrinkage, curing, and placement. The secant modulus of elasticity can be calculated as $E_{sec} = 50000\sqrt{f_c'}$. The last part of the stress strain relationship represents the softening behavior after the peak load is reached and continues up to the ultimate strain ofϵ_u.

Hognestad parabola is given by Equation 3-17:

$$\sigma_c = f_c' \left[\frac{2\epsilon_c}{\epsilon_0} - \left(\frac{\epsilon_c}{\epsilon_0} \right)^2 \right]$$

Equation 3-17

Damage parameters affect the model after the maximum compressive strength is reached. The compressive stress in the 3-point and 4-point bending tests modeled in this study was not expected to reach the peak value, so no damage parameter in compression was needed.

3.4.3 Tensile Behavior

Stress-strain in uniaxial tension follows a linear elastic relationship until the tensile strength (σ_c) is reached. After the tensile strength is reached, synthetic FRC material enters into a softening phase, and the stress decreases due to an increase of strain values. In synthetic-fiber-reinforced concrete, tension softening is mainly controlled by the fiber bridging effect. Because of the exclusion of damage parameters in tension (d_t), all of the inelastic strain can be regarded as cracking strain (Figure 3-9). Softening can then be expressed as a function of cracking strain (Equation 3-19).

$$\tilde{\epsilon}_t^{ck} = \epsilon_t - \tilde{\epsilon}_{0t}^{el}$$
$$\tilde{\epsilon}_{0c}^{el} = \frac{\sigma_c}{E_0}$$

Equation 3-18

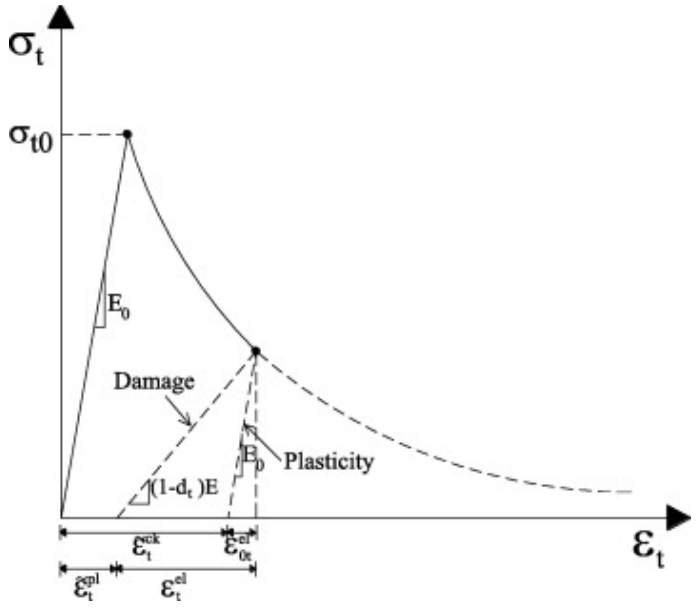

Figure 3-9 Uniaxial Tensile Behavior and Inelastic Tensile Strain in CDP Model [11]

ABAQUS uses the stress-cracking strain ($\tilde{\epsilon}_t^{ck}$) and initial modulus of elasticity, defined by the user, to obtain the stress strain (σ-ϵ_t) and calculate the corresponding stresses.

Tensile behavior of concrete material can be defined in the CDP model by means of stress strain (σ-ϵ), stress-crack width displacement (σ-w), or fracture energy criteria. It is preferable to utilize the σ-w law, rather than σ-ϵ relationship, to decrease the mesh dependency of the model. Therefore, the stress-crack displacement relationship was used for this study.

3.5 Loading and Boundary Conditions

Notched beams under 3-point bending and unnotched beams under 4-point loadings were assembled with the same dimensions as the test specimens in ABAQUS (Figure 3-10). Supports were modeled as a plate of 1-inch width, 6-inch length, and 0.2-inch depth. Support plates were modeled to have a contact interaction with the beam model. Plates were modeled as a rigid body to ensure all the stresses were taken by the beam. Uniform displacement control loading was used to

simulate the test loading condition. Boundary conditions were introduced to simulate the same boundary conditions as the real roller supports in the experiment.

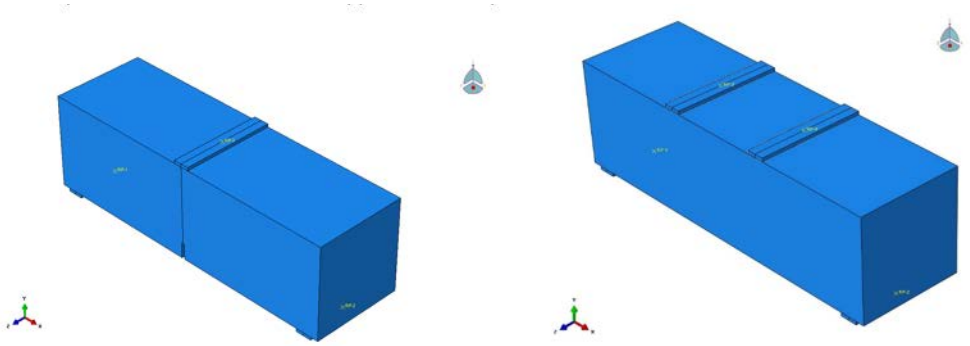

Figure 3-10 Geometry and Assembly of Beam Models

3.6 Mesh Development

Material property is programmed within the mesh element, and the interaction of all elements defines the structural response as a whole system.

Mesh dependency is one of the main problems when using the stress strain law to define the softening behavior of the FRC material in tension. Application of the fracture energy criterion in the form of stress crack width law is recommended in literature to avoid the mesh sensitivity problem [107], [108]. The type of the element, size, and arrangement have a significant effect on the numerical simulation.

Loading response of a finite element analysis depends significantly on the cracking displacement and propagation. Utilizing mesh that is too coarse in the cracking zone may result in a stiffer response than reality. On the other hand, the use of extra fine mesh may result in a softer response.

An inverse analysis method can be utilized to overcome these mesh dependency issues. This inverse analysis can be performed in two ways. One approach is to obtain the ideal mesh size

by assuming an appropriate material behavior model and refining the mesh size until the numerical results fit the experimental test [113]–[115]. The second approach is based on considering an appropriate mesh size and approximating the material property, adjusting it until the numerical result fits the experimental data. The second approach was utilized in the current study [93]–[95].

An 8-noded linear hexahedral brick element with reduced integration and hourglass control (C3D8R) was used to model the beams in this study. This type of element has the capability of high convergence and reduces the computation time.

Defining the softening behavior with a stress-crack width law is based on the assumption that fracture energy is a material property. In fracture-energy-based modeling of the materials in finite element, it is recommended that the element size used be similar to the aggregate size [107]. The largest dimension of aggregate size used in the synthetic FRC mixture was 3/8 inch, or about 0.3 inch. Existence of the notch on the 3-point bending tests limits the size of the mesh to less than or equal to the smallest dimension of the beam geometry or the notch width (0.2 in). This approach guarantees that all of the stresses concentrate on only one element, and smoother results can be obtained.

Considering the limitation of the mesh size based on the geometry of the notched beams, two types of FEM mesh size were used for modeling notched and unnotched beams.

The existence of the notch on the tension surface of the beam guarantees that the crack starts from the location of the notch. In order to have a sufficient number of elements based on the dimension of the notch and also decrease the commutation time, a bias type of meshing was considered for the notched beams. In order to have at least two elements in any dimension of the notched beam, a mesh size of 0.1 was used in the vicinity of the notch. Mesh size was gradually increased up to a size of 0.3 at the sides of the beam surface (Figure 3-11).

By performing a mesh convergence analysis, 4-point bending models of unnotched beams were meshed with a uniform 0.3 size mesh (Figure 3-12).

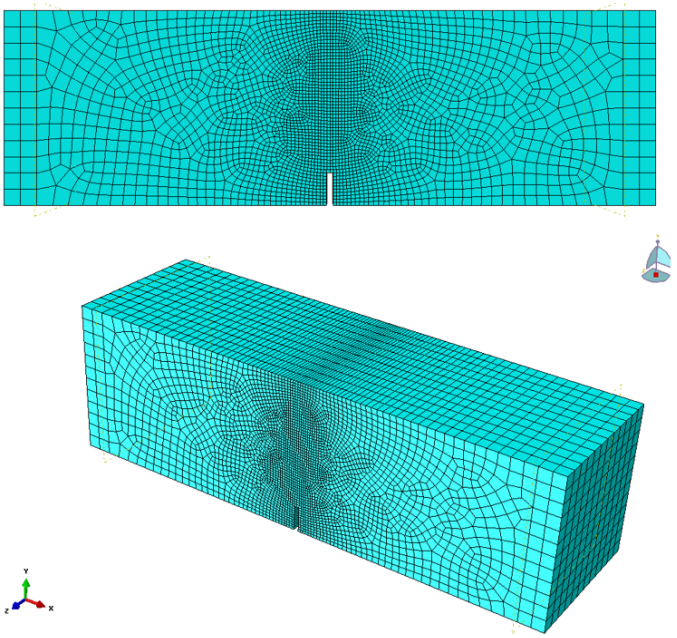

Figure 3-11 Typical mesh configuration in notched beam model

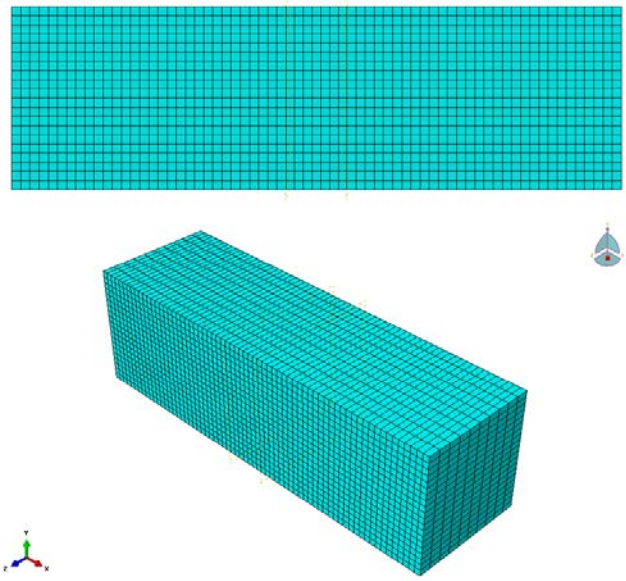

Figure 3-12 Typical mesh configuration in un-notched beam model

3.7 Tensile Stress-Crack Width Approximation

Accurate simulation of post-failure behavior of FRC material requires a method of approximating the tension-softening property. To avoid mesh sensitivity issues, the stress-crack width displacement relationship was utilized to model the tensile behavior of synthetic FRC beams. Difficulties associated with direct methods of obtaining the uniaxial tensile σ-w relation have led many researchers to use flexural tests to approximate the σ-w relation. This approximation can be performed by means of a numerical iterative procedure known as inverse analysis. Inverse analysis is performed based on assuming a softening curve and performing the numerical analysis. Obtained FEM results of load-deflection or load-CMOD is then compared to the experimental test data. This procedure repeats until the numerical results match the experimental test data. Figure 3-13 shows the algorithm of the inverse analysis method used in this study.

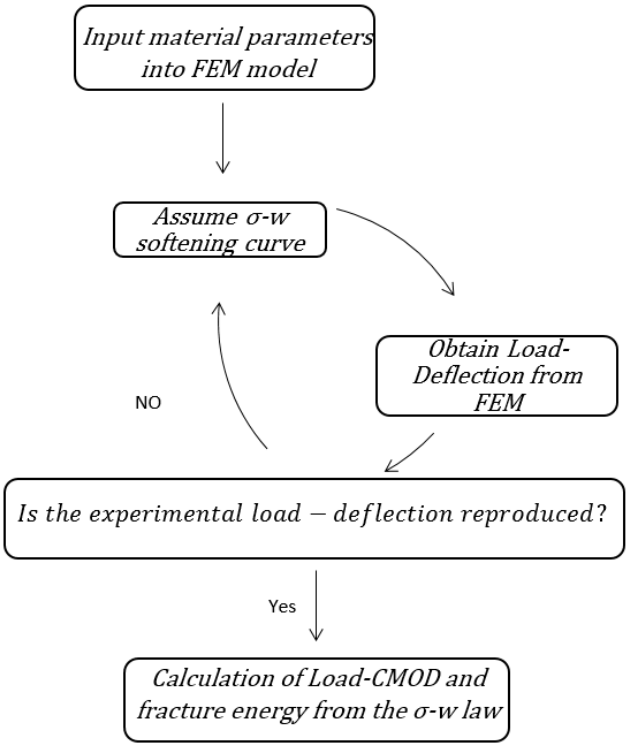

Figure 3-13 Flow Chart of Numerical Procedure for Inverse Analysis

In the current study, tensile behavior of the synthetic FRC was introduced into the CDP model as stress-crack displacement. Tension behavior in CDP is defined by introducing the values of crack displacement and their corresponding stresses. Inverse analysis requires the user to assume a softening curve to start the procedure. The fitting procedure and FEM load response are directly influenced by the type of the curve that is being used. As synthetic FRC exhibits more ductile and nonlinear softening response in post-crack regions compared to the plain concrete, the linear softening relation is not sufficient. Stress-crack displacement can be defined with various curves, including bilinear, tetra linear, exponential, etc. m [107].

Generally, researchers prefer the multilinear definition of σ-w curve to approximate the softening behavior of steel FRC in inverse analysis applications (Figure 3-14) [11], [107]. Linearity of the model decreases the number of parameters that define the σ-w curve. In this case, only a few parameters need to be changed to significantly expedite the fitting procedure but limit the flexibility of the model to simulate various material behaviors.

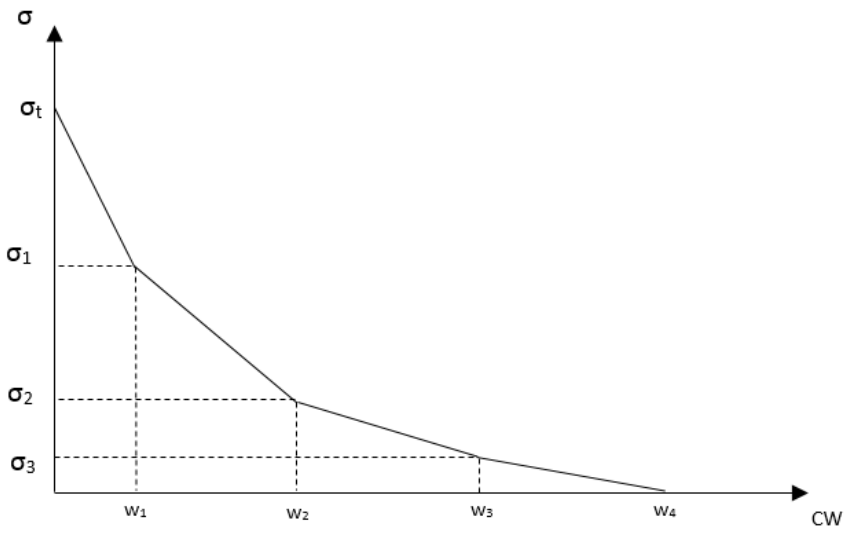

Figure 3-14 Multilinear definition of σ-w curve

Figure 3-15 shows an example of the load-displacement curve obtained using ABAQUS CDP for a 4-point bending beam test of steel FRC with three different mesh sizes. Tension behavior was modeled using a bilinear softening curve [116].

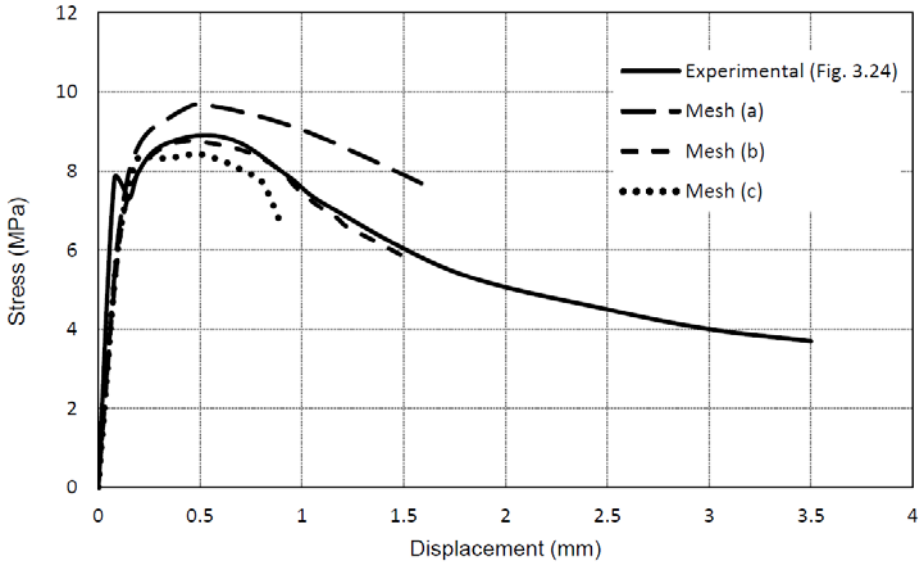

Figure 3-15 Example of Load Displacement Curve Obtained using ABAQUS CDP for a 4-Point Bending Beam Test of Steel FRC, Using a Bilinear Softening Curve. [116]

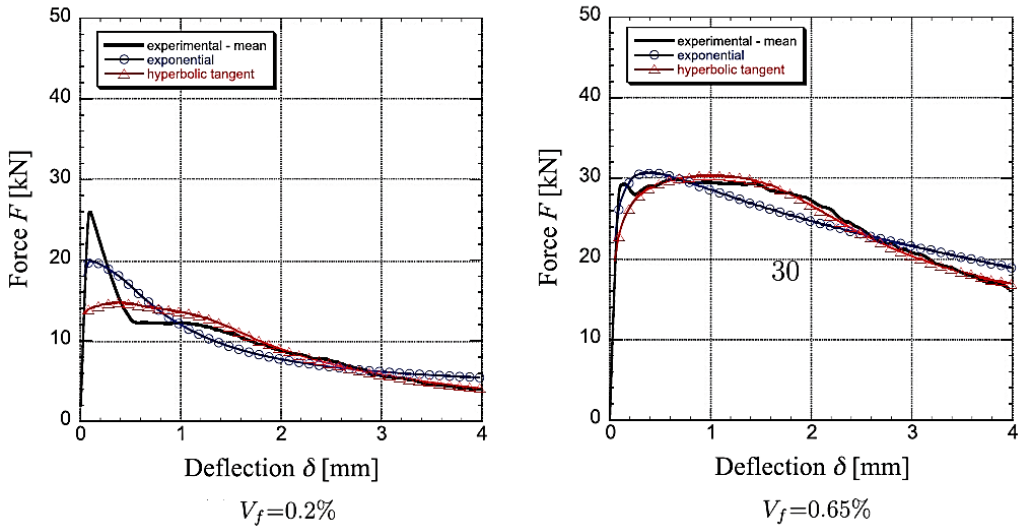

Figure 3-16 Numerical Approximation and Experimental Result for Different Fiber Volume Fractions (VF) under 4-point Bending [26]

Michel et al [26] used two types of exponential and tangent hyperbolic stress-crack widths to model 4-point bending tests performed on various dosages of steel fibers. Their study concluded that the exponential curve offers higher precision at the small deflection, but the hyperbolic curve provides a more accurate overall approximation. Figure 3-16 shows the study results for two dosages of steel fibers [26].

A low volume fraction of fiber material tends to show a greater initial decrease of load capacity after the peak load is reached. As can be seen in both Figure 3-15 and Figure 3-16, none of the study's approximations could obtain the behavior up to the peak point and post-crack at the same time in cases of small fiber dosages (Figure 3-16).

The load deflection response of the synthetic FRC beams in this study showed a drop in the loading value after the crack was initiated. This behavior was observed for both 3-point bending and 4-point bending tests and both fiber volume fractions. The initial drop was more significant in the case of 0.54% volume fraction (8.3 PCY). Test results also presented a hardening behavior after the initiation of the crack. FEM simulation is desired to accurately approximate the test results, especially by means of failure load, initial drop, and hardening load. This accuracy was of great interest to this study to make it possible to compare the 2D DIC crack width measurement with the FEM results.

Several curve types, including multilinear, exponential, and tangent hyperbolic, were attempted to model the beam test in ABAQUS CDP. All of the models showed the capability to obtain the first peak and initial drop, but none of them could obtain the hardening region of the load displacement curves.

Post-crack behavior of the synthetic FRC directly depends on the fiber bridging effect. Some studies suggest that the bridging phase can be approximated by considering a constant stress state as the crack displacement increases [117]. However, linear definition of post-crack hardening,

in a form of ascending branch after a softening phase or a plateau stress state as the crack displacement increased, did not result in a desirable load response.

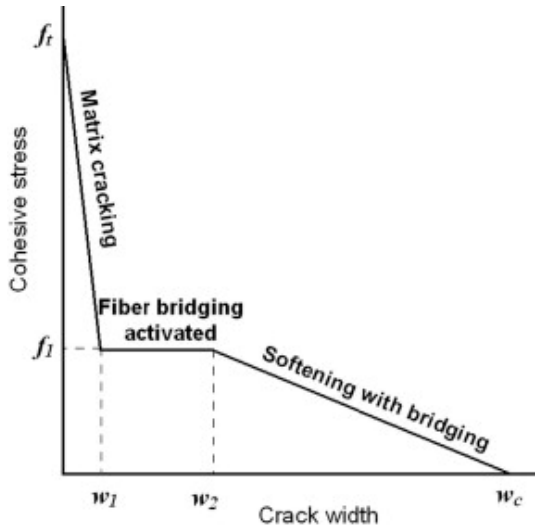

Figure 3-17 Trilinear Softening Curve with a Plateau State for Fiber Bridging [117]

Michel et al [26] concluded that the exponential curve offers good precision for small displacement levels. In the current research, based on the study performed by Michel et al [26] and the overall shape of the load-CMOD response of the tests obtained through the 2D DIC technique, a piecewise function was suggested for stress-crack displacement approximation. The softening curve can be formulated with Equation 3-19.

$$\sigma(w) = \begin{cases} \sigma_1 = (f_1 - f_2)\, e^{-\alpha w} + f_2 & , \quad w \le w_1 \\ \sigma_2 = (f_4 - f_3)\, sin\left[\frac{\pi}{d}(w - w_1)\right] + f_3 & , \quad w_1 < w \le w_2 \\ \sigma_3 = c(\frac{d\sigma_2}{dw})(w - w_2) + \sigma_2(w_2) & , \quad w > w_2 \end{cases}$$

Equation 3-19

If the derivation is performed and the value for the functions is inputted, Equation 4-19 can be rewritten as Equation 3-20:

$$\sigma(w) = \begin{cases} (f_1 - f_2)\, e^{-\alpha w} + f_2 & , \quad w \le w_1 \\ (f_4 - f_3)\, sin\left[\frac{\pi}{d}(w - w_1)\right] + f_3 & , \quad w_1 < w \le w_2 \\ c\frac{\pi}{d}(f_4 - f_3)\cos\left[\frac{\pi}{d}(w_2 - w_1)\right](w - w_2) + (f_4 - f_3)\, sin\left[\frac{\pi}{d}(w_2 - w_1)\right] + f_3 \ , & w > w_2 \end{cases}$$

Equation 3-20

The analysis for the value of the w_2 was calculated with Equation 3-21:

$$w_2 = w_1 + d$$

Equation 3-21

Based on the recommendation of Michel et al [26], behavior up to the beginning of the hardening phase was modeled with an exponential curve. The hardening phase (crack bridging) was modeled with a sine function, and the fiber pull-out or the final softening phase was modeled as a linear tangent to the descending branch of the hardening curve. Nonlinearity and the number of parameters allowed the user to widely adjust the softening curve and minimize the relative errors.

Inverse analysis procedure starts with an initial assumption for the $\sigma\sigma - ww$ curve. Based on the proposed formulation, the softening curve can be approximated by adjusting eight parameters that define the shape of the curve in Equation 3-20. Figure 3-18 shows a typical presentation of the tension-softening curve in Equation 3-20, used for experimental curve fitting.

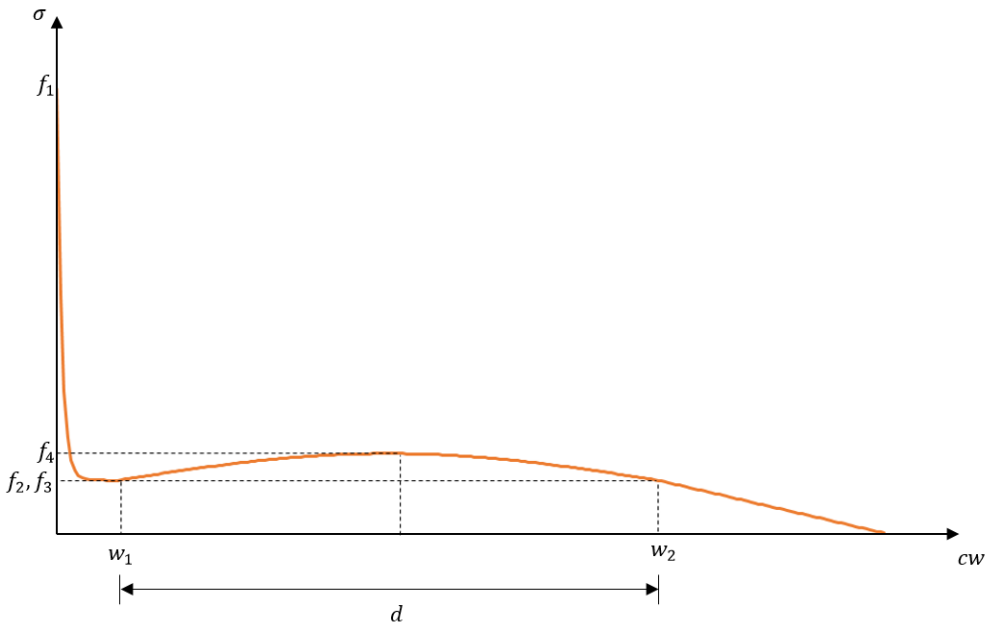

Figure 3-18 Tension Softening Equation for Experimental Curve Fitting

To prevent possible numerical errors, limitation of minimum stress equal to one-hundredth of initial cracking stress ($\sigma(w) \geq 0.01\ f_1$) was considered when introducing the $\sigma\sigma - ww$ softening data into the CDP [108].

3.8 Numerical Results

Inverse analysis, based on the piecewise function presented earlier, was performed for all the flexural beam tests. In the experimental test results section, it was observed that load-deflection responses of the beam specimens for each fiber volume fraction presented different results. These variations were in peak loads, initial drop of load capacity immediately after the crack, and the hardening behavior. It was suggested that these variations were mainly due to the effect of fiber orientations. Consequently, consideration of an average response is not a good representation for the flexural responses of the synthetic FRC specimens. Therefore, each of the experimental load-deflection responses was fitted individually through a fitting procedure, as explained in the last section. Corresponding tension-softening parameters (σ-w curve) were obtained for each specimen,

and the final results were compared in terms of fracture energy or the area under the stress-crack width curve.

3.8.1 Notched synthetic FRC beams under 3-Point bending

Fitted curves for 3-point flexural load-deflection responses are presented in the figures 3-19 to 3-24. As depicted, there was good agreement between all the fitted curves obtained from the FEM results and experimental responses. The main variation was in the unloading region, immediately after the crack was initiated. Experimental data for both load-deflection and load-crack width response, between the first peak load and initial load drop, is only consist of two data points. Sudden deformation of the specimen due to cracking caused a displacement/crack width jump; consequently, the test method and data accusation system used for this study could not record the specimens' unloading behavior in this region. For simplification, this behavior was considered linear in the test results. The exact behavior in this region is unknown, and the difference between the numerical and experimental results in this region was neglected. Exact behavior in the unloading region, immediately after the crack, can be obtained by means of a CMOD controlled testing.

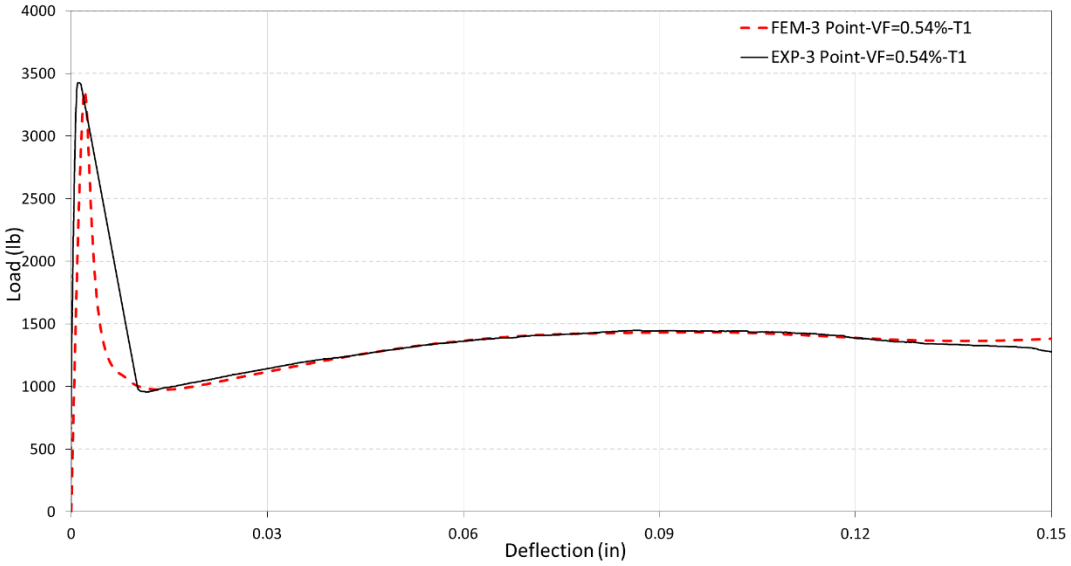

Figure 3-19 Experimental vs FEM Load- Deflection for 3-Point Bending - Synthetic FRC VF=0.54% - Test 1

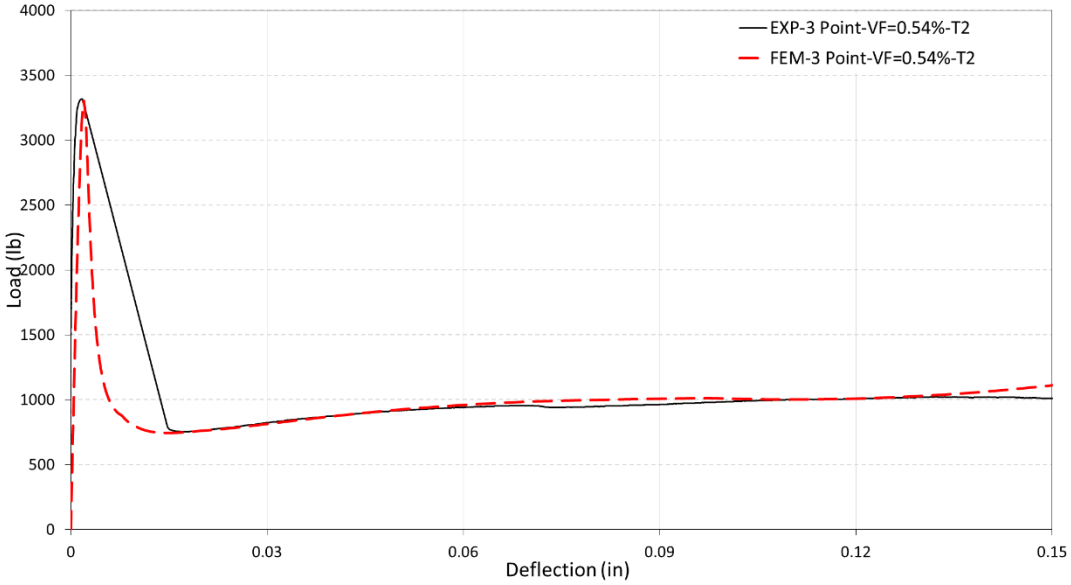

Figure 3-20 Experimental vs FEM, Load- Deflection for 3-point bending - Synthetic FRC VF= 0.54% - Test 2

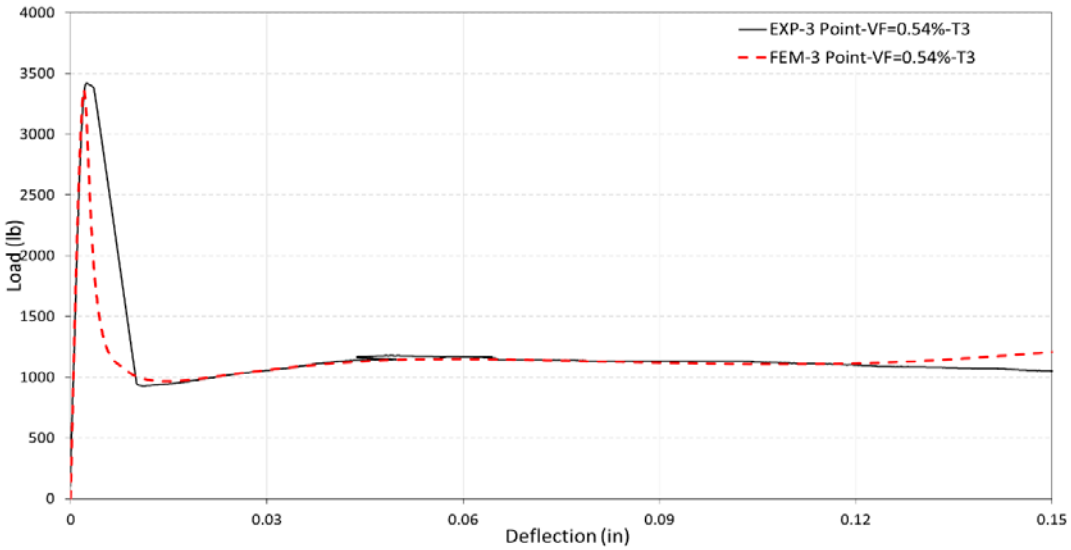

Figure 3-21 Experimental vs FEM, Load- Deflection for 3-Point Bending - Synthetic FRC VF= 0.54% - Test 3

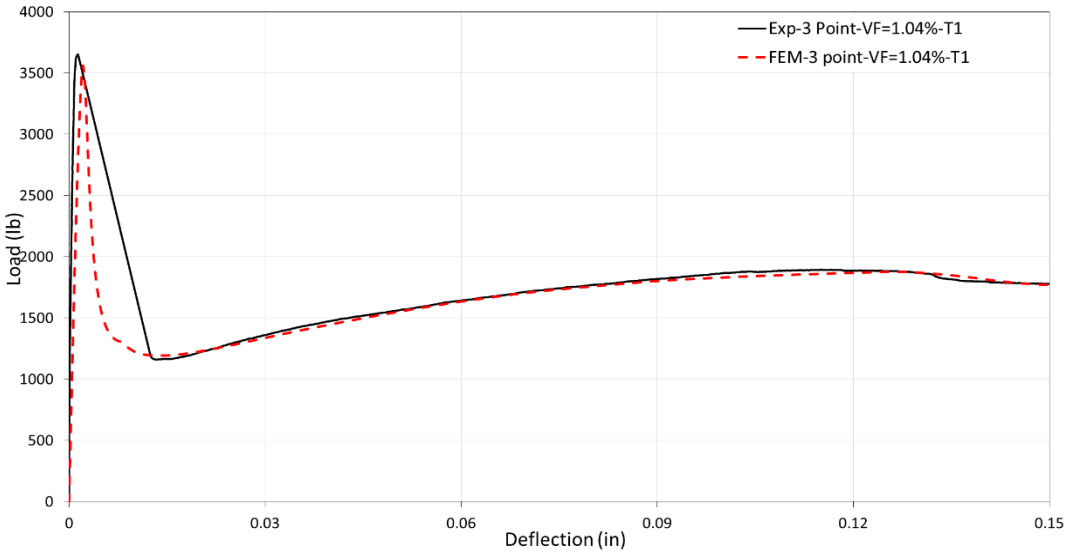

Figure 3-22 Experimental vs FEM Load- Deflection for 3-Point Bending - Synthetic FRC VF= 1.04% - Test 1

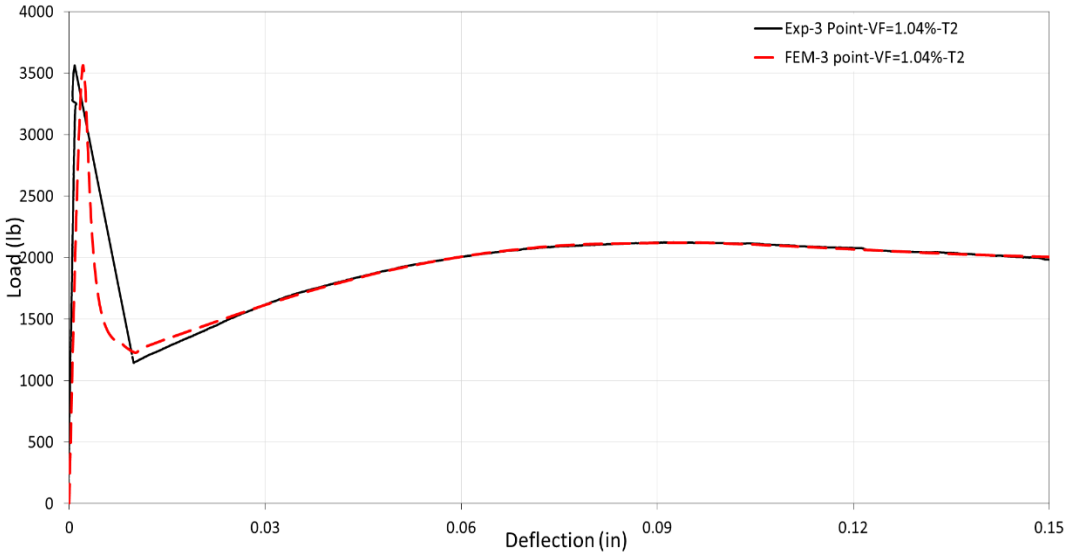

Figure 3-23 Experimental vs FEM Load- Deflection for 3-Point Bending - Synthetic FRC VF= 1.04% - Test 2

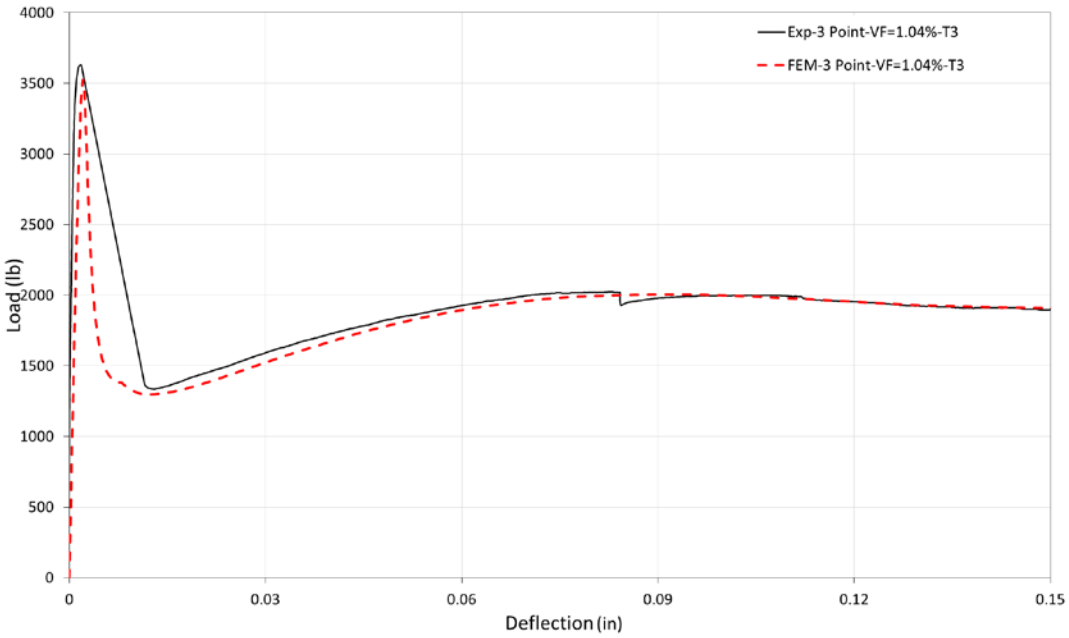

Figure 3-24 Experimental vs FEM Load- Deflection for 3-Point Bending - Synthetic FRC VF= 1.04% - Test 3

Table 3-2 shows a summary of the obtained parameters for the tension models used for the fitting procedure.

Table 3-2 Fitted parameters for the softening stress-crack displacement law using notched beam under 3 point bending

VF (%) –Test#	f_1	f_2	α	f_3	f_4	d	w_1	w_2	c
0.54-T1	332.5	40	740	40	60	0.15	0.017	0.15	1
0.54-T2	332.5	30	740	30	40	0.13	0.017	0.147	2
0.54-T3	332.5	40	740	40	50	0.1	0.017	0.117	1
1.04-T1	359	50	800	50	74	0.185	0.017	0.202	3.5
1.04-T2	359	50	800	60	91	0.165	0.017	0.182	1
1.04-T3	359	55	880	55	86	0.165	0.017	0.182	1

FEM crack width was calculated based on the obtained model through the inverse analysis. FEM modeling, based on the CDP model, was performed considering all inelastic strains as cracking strain. By this assumption, all of the displacement outside of the region that undergoes plastic deformation is due to the crack displacement.

All of the notched beams presented the concentration of plastic strains in a region above the notch tip. The area undergoing plastic deformation can be translated as a single crack observed in the experimental study (Figure 3-25).

Isosurface distribution of plastic strain can provide a visual representation of crack propagation in a simulation of synthetic FRC notched beams undergoing a 3-point flexural loading (Figure 3-26).

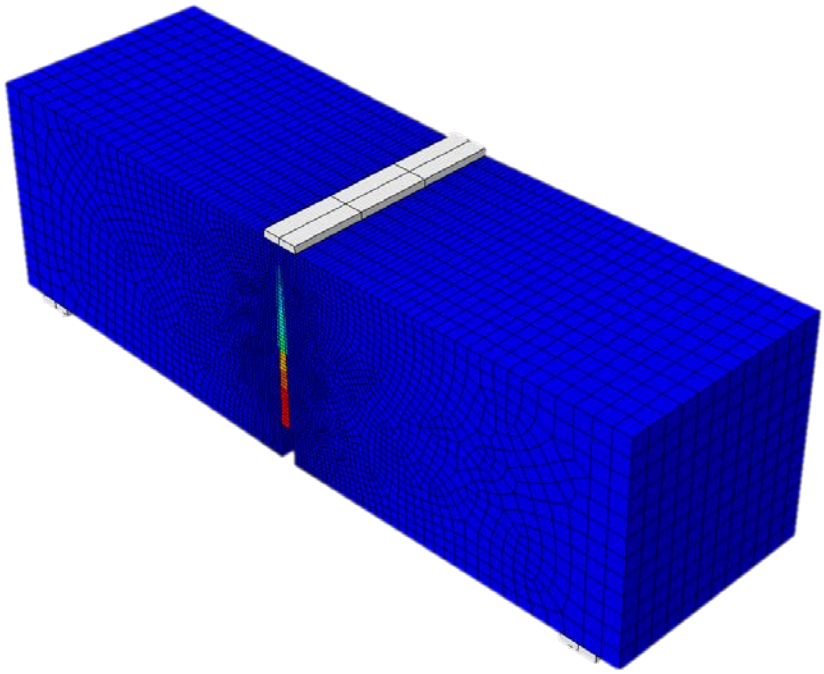

Figure 3-25 Typical Plastic Strain Distribution in a 3-Point Bending Model

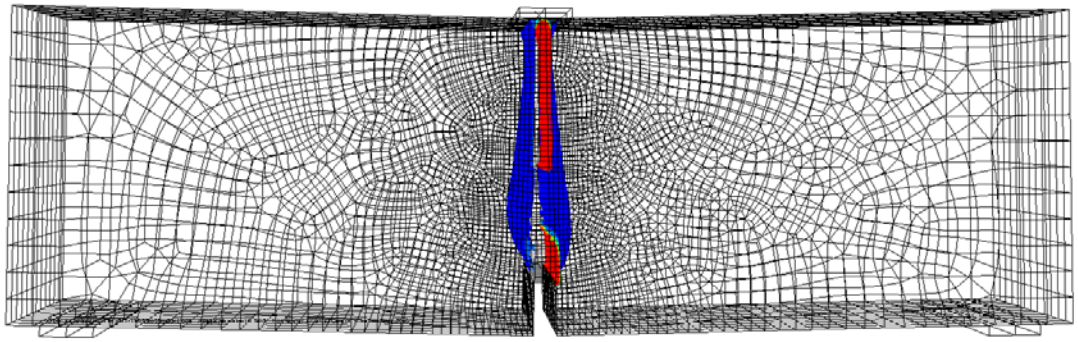

Figure 3-26 Typical Isosurface Distribution of Maximum Principal Plastic Strain at the end of a 3-Point Bending Simulation

By assuming the plastic strain region as the cracked region, the crack width can be obtained by calculating the relative horizontal displacement (U1) of the two nodes adjacent and across the plastic zone (Figure 3-27). The same method was used for calculation of the experimental crack width with the DIC method. A more detailed explanation of considering crack width as horizontal displacement can be found in the next section.

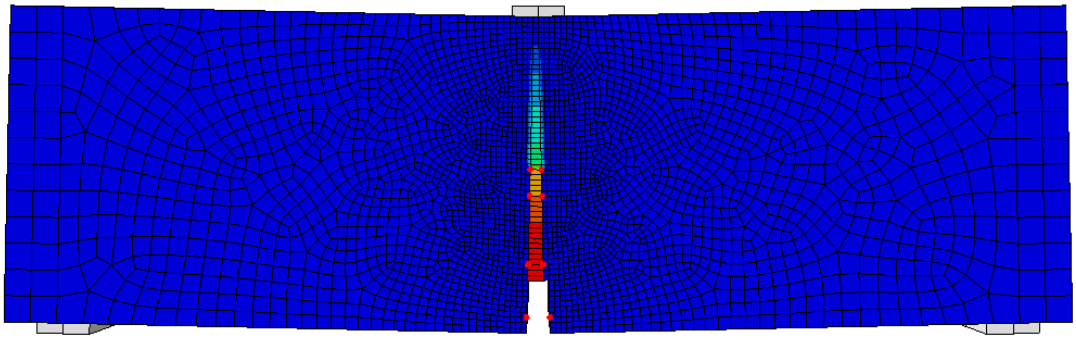

Figure 3-27 Crack Width Calculation based on the Relative Horizontal Displacement of the Nodes across the Plastic Strain Band

Numerical crack widths were obtained through the FEM analysis of notched beams under 3-point bending tests, with the tensile property obtained through the inverse analysis of fitting the load deflection. The FEM load-CMOD responses were calculated from the models and compared with experimental load-CMOD results for both 0.54% and 1.04% fiber volume fractions. Crack width was obtained at the same beam height as was calculated in the 2D DIC analysis (0.3 inch from the bottom surface of the beam = 3 element height) (Figures 3-28 to 3-33).

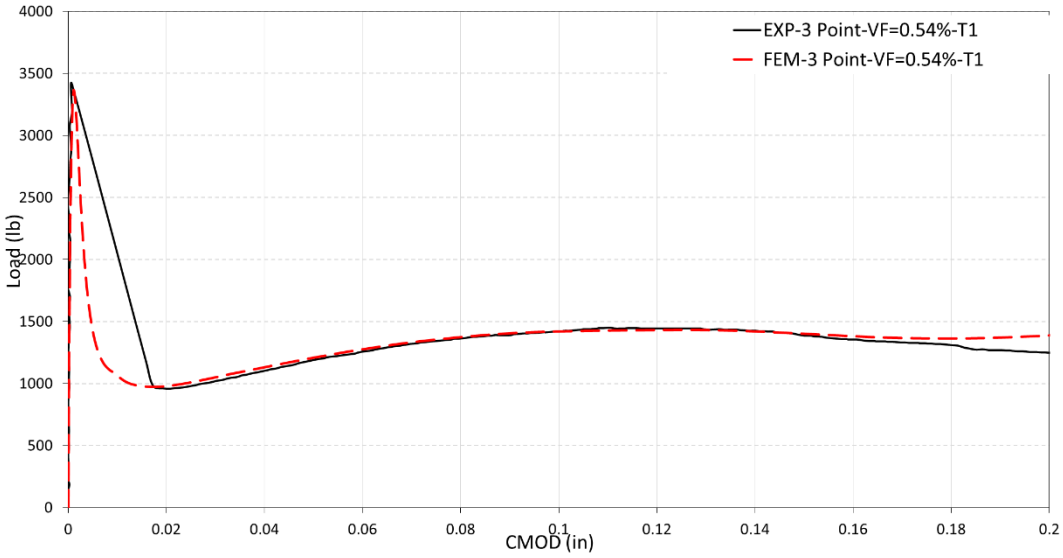

Figure 3-28 Experimental vs FEM Load-CMOD for 3-Point Bending – Synthetic FRC VF= 0.54% - Test 1

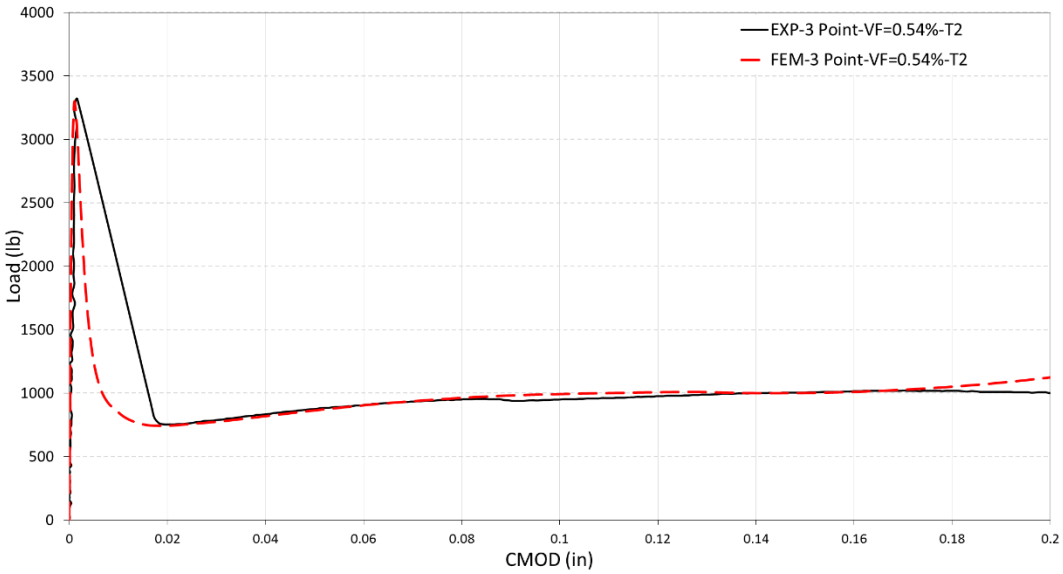

Figure 3-29 Experimental vs FEM Load-CMOD for 3-Point Bending – Synthetic FRC VF=0.54% - Test 2

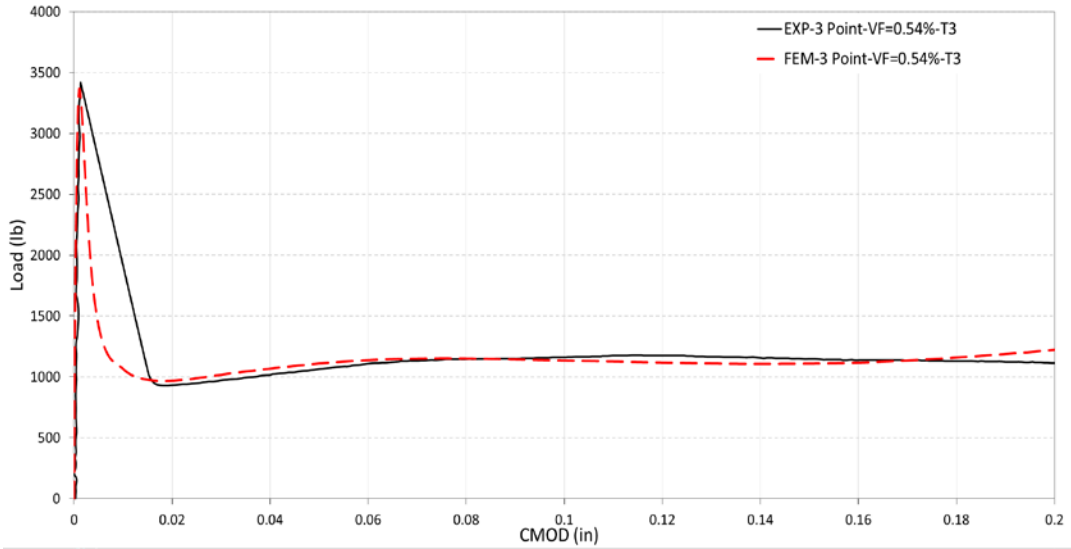

Figure 3-30 Experimental vs FEM Load-CMOD for 3-Point Bending – Synthetic FRC VF= 0.54% - Test 3

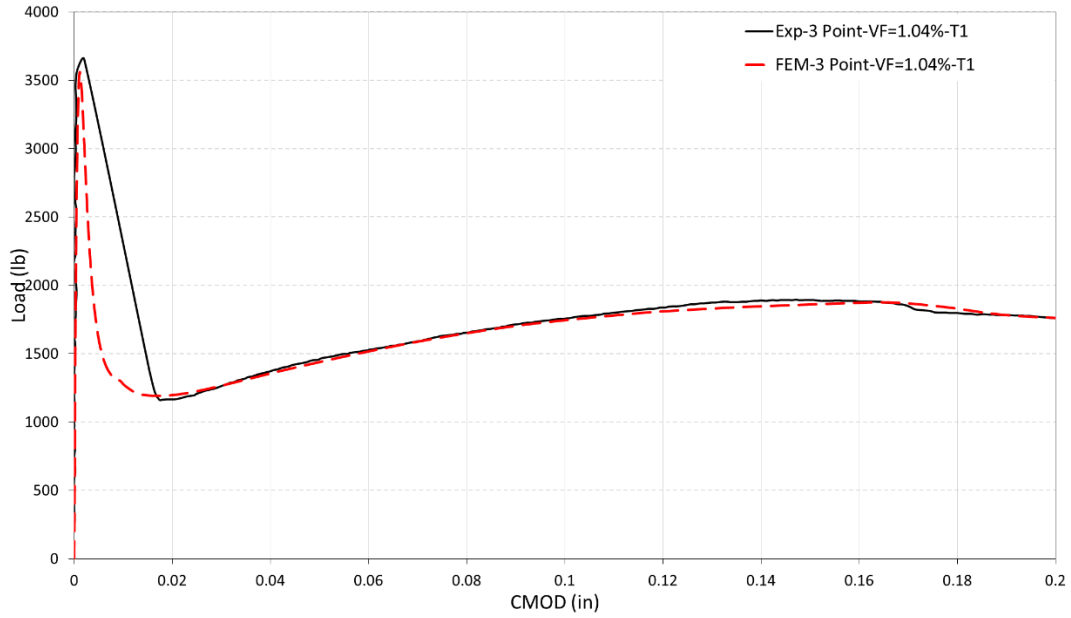

Figure 3-31 Experimental vs FEM Load-CMOD for 3-Point Bending – Synthetic FRC VF=1.04% - Test 1

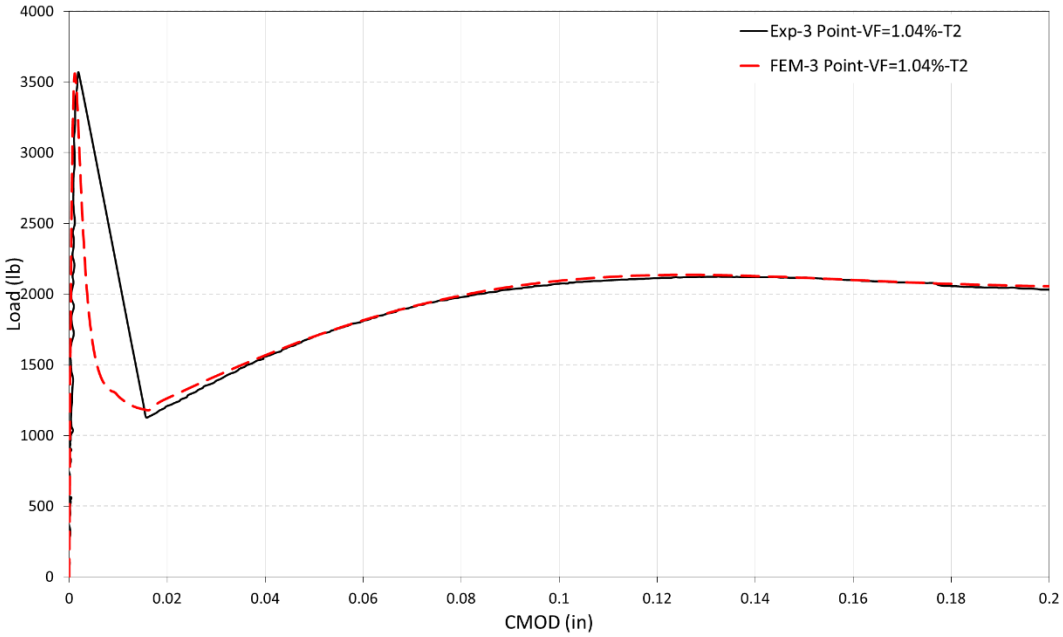

Figure 3-32 Experimental vs FEM Load-CMOD for 3-Point Bending – Synthetic FRC VF= 1.04% - Test 2

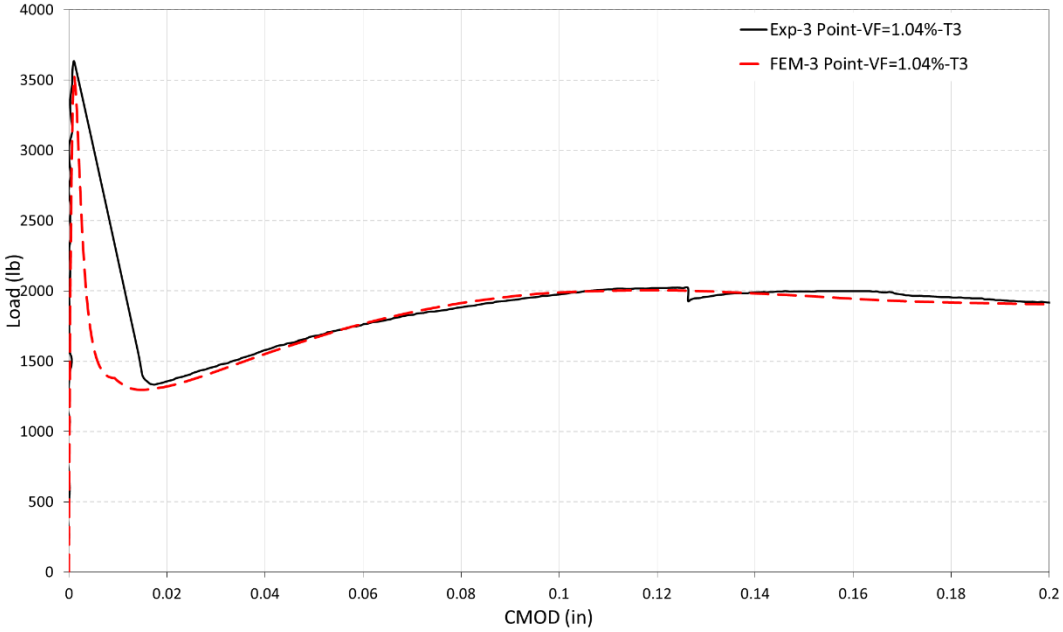

Figure 3-33 Experimental vs FEM Load-CMOD for 3-point bending – Synthetic FRC VF= 1.04% - Test 3

As presented in the Figures 3-28 to 3-33, the FEM Load-CMOD results showed a very good agreement with the experimental results obtained through the 2D DIC method. The main variation of the numerical and experimental results was in the area between the peak load and load drop, immediately after the crack. The same variation was observed in the load- deflection responses. The load-crack width data for this region was not recorded due to the sudden deformation imposed on the specimen immediately after the crack. This deformation happened in a fraction of a second, and the data accusation system used for the experimental study was not able to record the data.

Overall, the FEM result, using the CDP model and the proposed softening law, shows the capability for simulation of dry-cast synthetic FRC beams under flexural loading. The fitted FEM model can be used for the investigation of crack specifications. In addition, the FEM model, optimized by the load deflection data, can provide the crack width by means of relative nodal displacement.

3.8.2 Synthetic FRC Beams under 4-Point Bending

Fitted curves for flexural load-deflection responses under 4-point bending are presented in Figures 3-34 to 3-39. Unlike the notched beams, beams under 4-point bending did not have a predefined crack location, and no concentration of stress was imposed on the model. This situation led to higher peak load, higher energy absorption, and unknown cracking location. Due to this characteristic of the beams and loading condition, the FEM model became very sensitive to tension model parameters.

Fitted curves presented an overall good agreement with the experimental results. The only major variations were observed for higher deflection values in the case of the 1.04% fiber volume fraction. During the fitting process, it is important to make sure that the model presents single cracking. These difficulties are more severe in the case of higher fiber dosages (1.04%),

which present a smaller load capacity decrease immediately after crack initiation, compared to the 0.54%. During the fitting process for beams with 1.04% fiber volume fraction, the FEM models presented greater sensitivity to tension, and with a small variation in the parameter, the models presented multiple cracking behavior. There was only one major macro cracking and the effect of fibers bridging in this macro crack was the governing agent in the post-cracking behavior. These difficulties caused the FEM results to have some variations in the post-crack hardening stage for the higher fiber volume fraction.

As was observed in the FEM models of notched beams under 3-point bending, the behavior in the unloading region, immediately after the crack initiation and prior to the hardening state, was not in good agreement with the experimental data. The experimental data for this region was not available due to the test procedure used for this study, and the region was considered linear, decreasing in all the experimental test results. However, different fitted parameters presented various possible behaviors for this region (e.g. Figure 3-34 and 3-35). This variation suggests the capability of the model to fit various possible behaviors for this region. More advanced optimization methods, such as neural networks or genetic algorithms, can be utilized to provide better-fitted curves for this region.

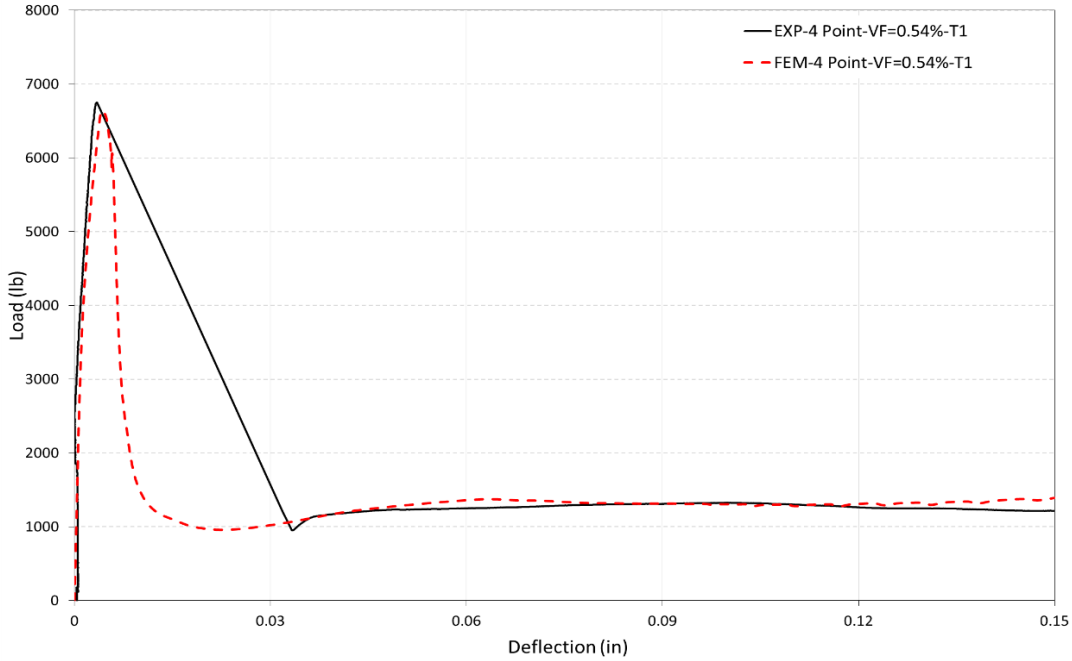

Figure 3-34 Experimental vs FEM Load- Deflection for 4-Point Bending - Synthetic FRC VF=0.54% -Test 1

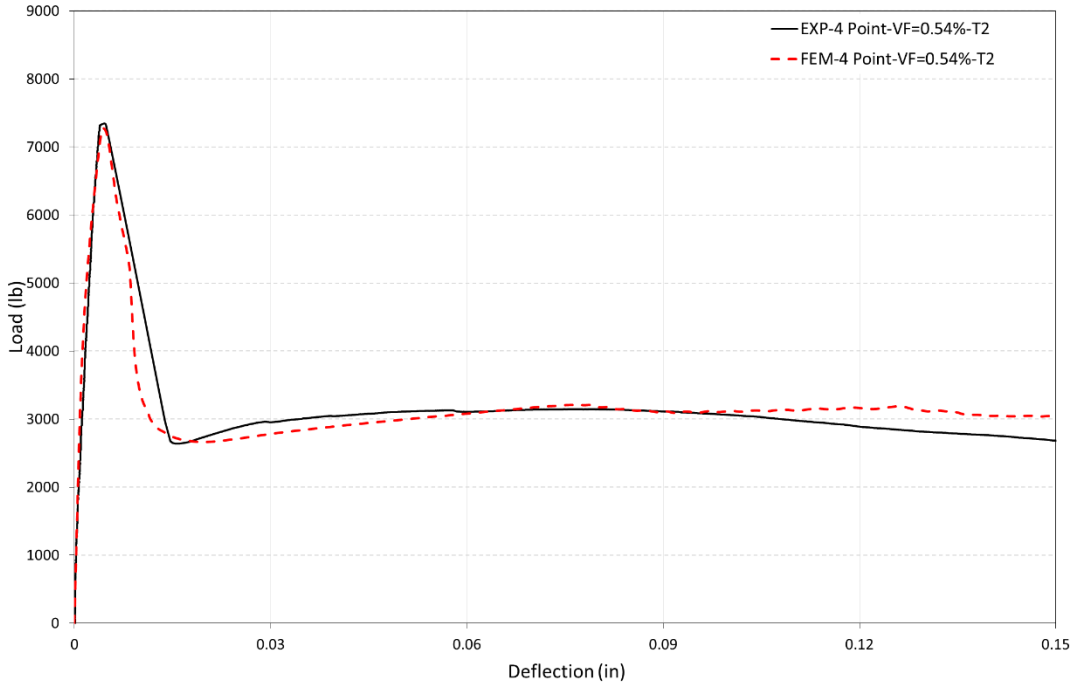

Figure 3-35 Experimental vs FEM Load- Deflection for 4-Point Bending - Synthetic FRC VF=0.54% -Test 2

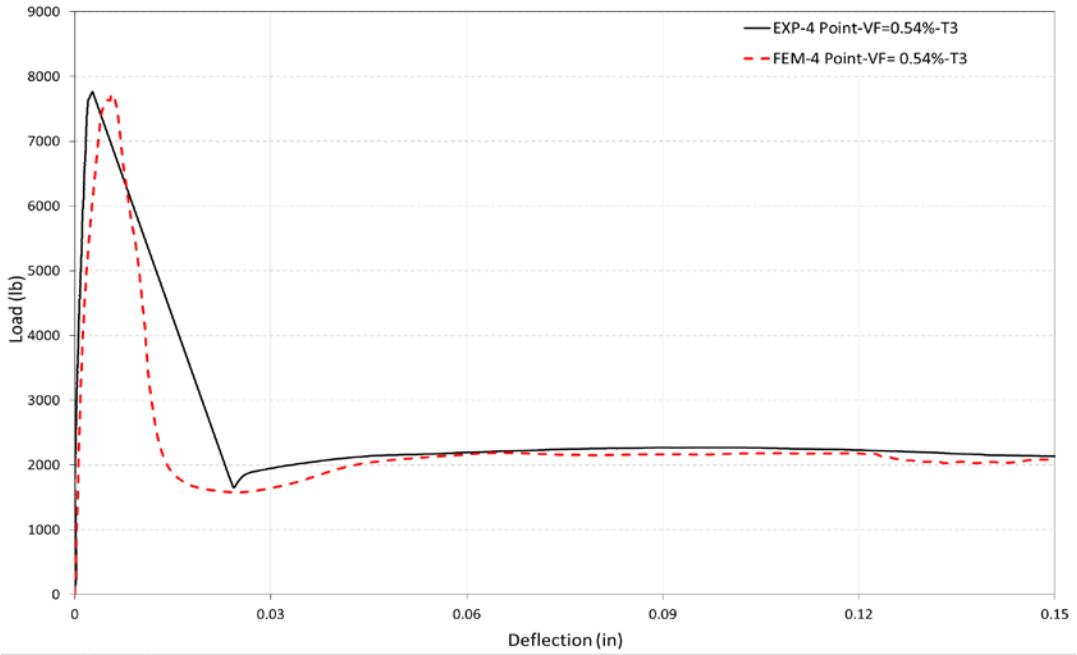

Figure 3-36 Experimental vs FEM Load- Deflection for 4-Point Bending - Synthetic FRC VF= 0.54% -Test 3

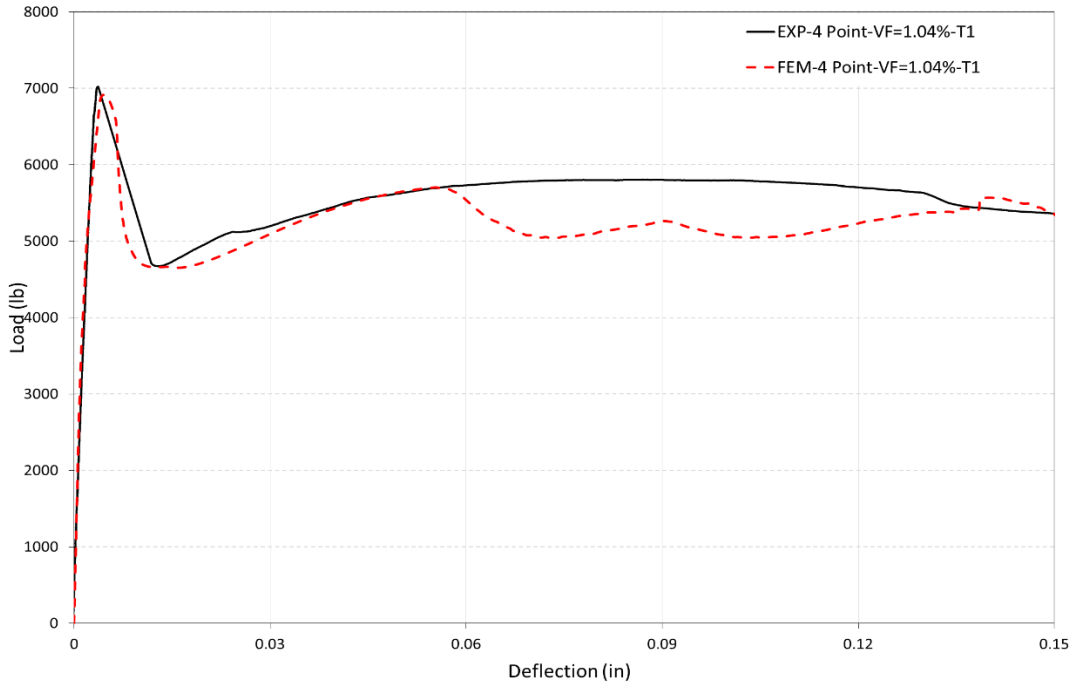

Figure 3-37 Experimental vs FEM Load- Deflection for 4-Point Bending - Synthetic FRC VF= 1.04%- Test 1

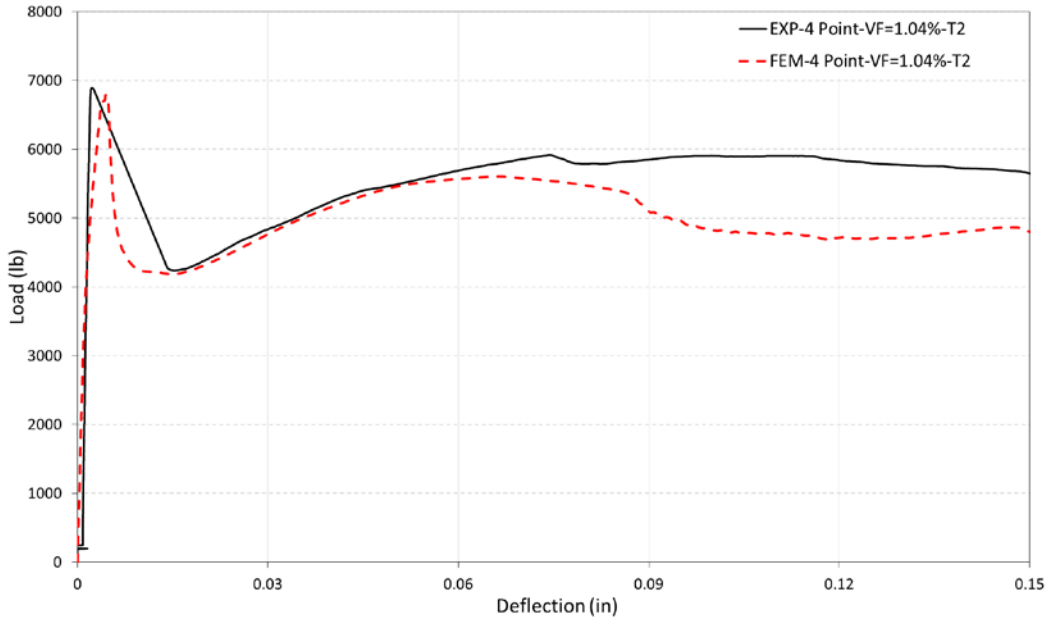

Figure 3-38 Experimental vs FEM Load- Deflection for 4-Point Bending - Synthetic FRC VF= 1.04% -Test 2

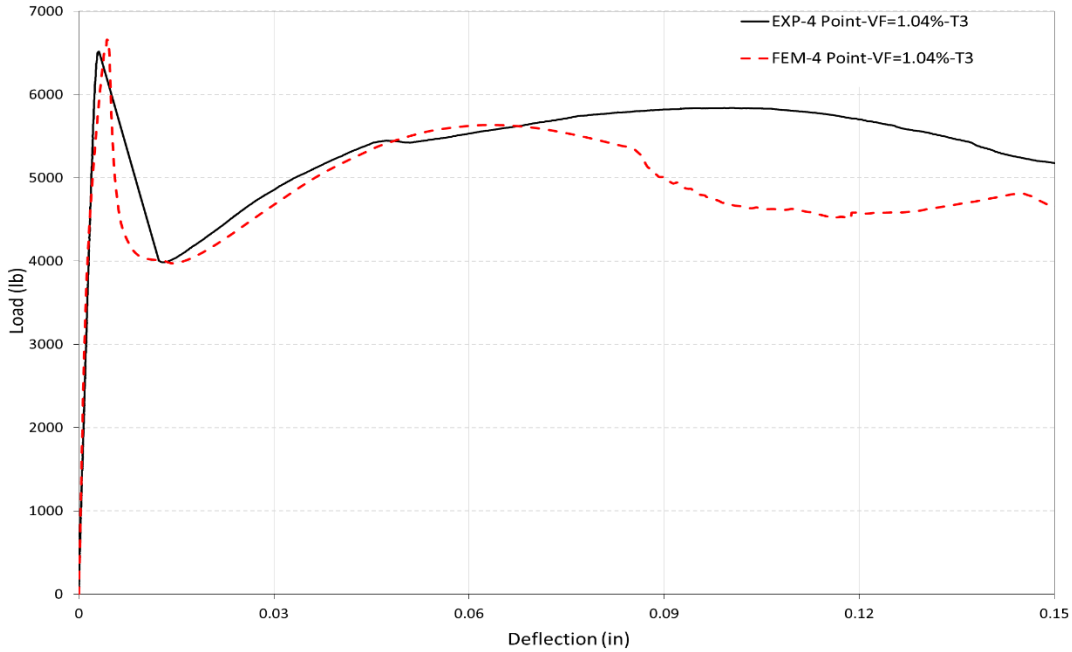

Figure 3-39 Experimental vs FEM Load- Deflection for 4-Point Bending - Synthetic FRC VF= 1.04%- Test 3

Table 3-3 3 shows a summary of the obtained parameters for the tension models used for the fitting procedure.

Table 3-3 Fitted parameters for the softening stress-crack displacement law of synthetic FRC, using beam under 4 point bending

VF (%) –Test#	f_1	f_2	α	f_3	f_4	d	w_1	w_2	c
0.54-T1	180	15	500	19	20	0.039	0.039	0.078	5
0.54-T2	201	47	700	50	51	0.09	0.025	0.115	2
0.54-T3	205	26	440	37	38	0.015	0.039	0.054	1
1.04-T1	183	87	878	87	106	0.1	0.022	0.122	1
1.04-T2	186	78	881	78	105	0.1	0.019	0.119	0.5
1.04-T3	183	74	880	74	106	0.1	0.016	0.116	0.5

The FEM crack width was calculated based on the softening models obtained through the inverse analysis. The FEM modeling, based on the CDP model, was performed considering all inelastic strains as cracking strain. By this assumption, all of the displacement outside of the region that undergoes plastic deformation is due to crack displacement.

All the beams presented a single plastic strain band in the middle section. As was explained for the 3-point bending case, the region undergoing plastic deformation can be translated as the single crack observed in the experimental study (Figure 3-25).

By assuming the plastic strain region as the cracked region, the crack width can be obtained by calculating the relative horizontal displacement (U1) of the two nodes adjacent and across the plastic zone (Figures 3-40).

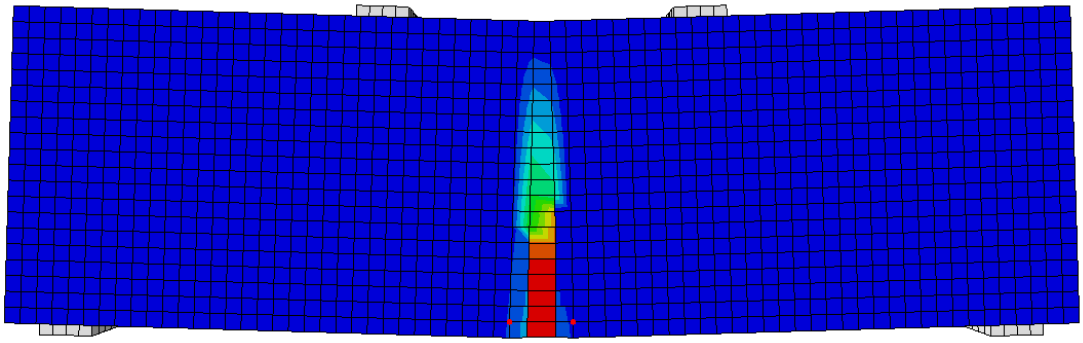

Figure 3-40 Typical Plastic Strain Distribution in a 4-Point Bending Model

The horizontal deformation field, obtained from the FEM model, can also provide a better understanding of beam deformation due to cracking. Figure 3-41 presents an example of a horizontal deformation field for a beam under 4-point bending. The points at which the crack width was calculated, based on their displacement, are marked with white circles. The same points are marked in the Figure 3-40. Figures 3-41 and 3-40 present the deformation field and maximum principal plastic strain distribution of the same model and at the same stages. Figure 3-40 shows that the plastic strain is presented in three element bands in the middle of the beam. If all the post-crack deformation in the synthetic FRC is considered to be due to the crack displacement, the crack displacement needs to be calculated at the nearest point adjacent to the crack zone (zone with zero displacement) at nodes which are not undergoing plastic deformation. Hence, calculation of the crack width at a height of one element size was performed at the edge of the regions shown in dark blue and red. This region represents the maximum deformation at the nodes adjacent to the cracked zone (green band) (Figure 3-41).

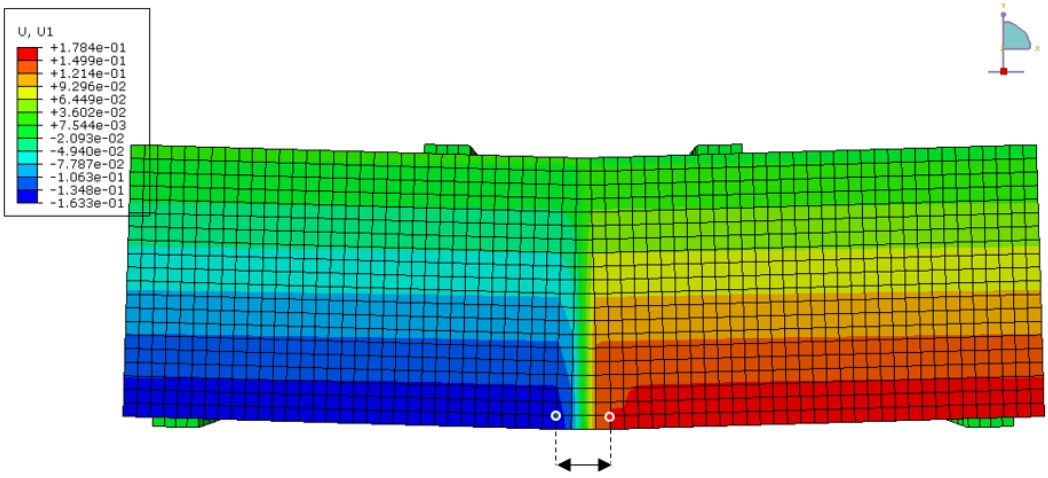

Figure 3-41 Example of the Horizontal Deformation Field in a 4-Point Bending Model at Final Stage and Crack Width Calculation

Numerical crack widths were obtained through the FEM analysis of beams under 4-point bending, using the tensile property obtained through inverse analysis of load-deflection curves. The FEM load-CMOD response was calculated from the models and compared with experimental load CMOD results for both 0.54% and 1.04% fiber volume fractions. Crack width was obtained at the same beam height as was used in the 2D DIC analysis (0.3 in from the bottom surface of the beam=1 element height) (Figure 3-40).

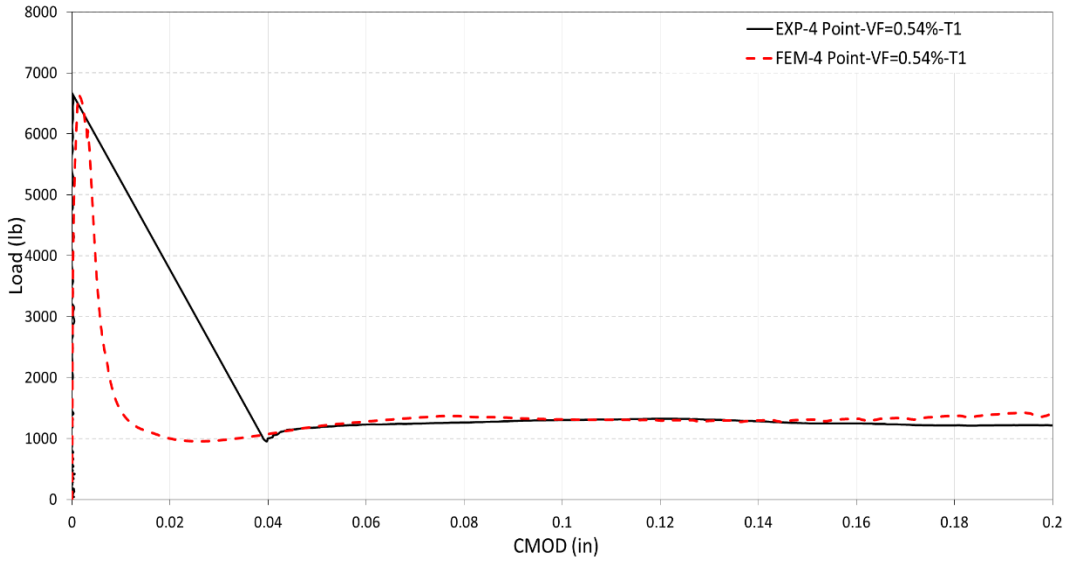

Figure 3-42 Experimental vs FEM Load-CMOD for 4-Point Bending – Synthetic FRC VF=0.54% - Test 1

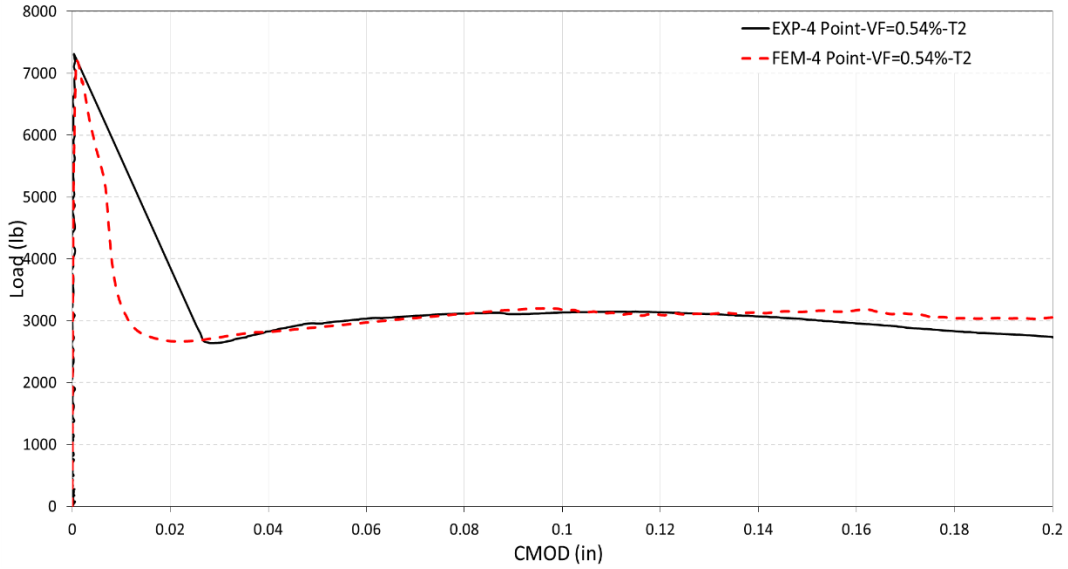

Figure 3-43 Experimental vs FEM Load-CMOD for 4-Point Bending – Synthetic FRC VF=0.54% - Test 2

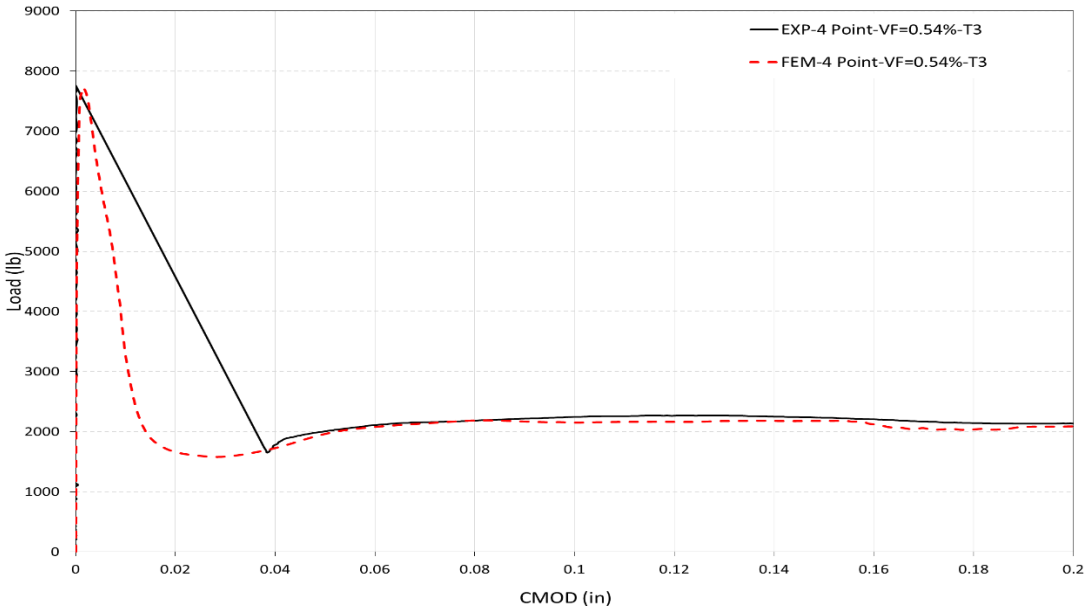

Figure 3-44 Experimental vs FEM Load-CMOD for 4-Point Bending – Synthetic FRC VF=0.54% - Test 3

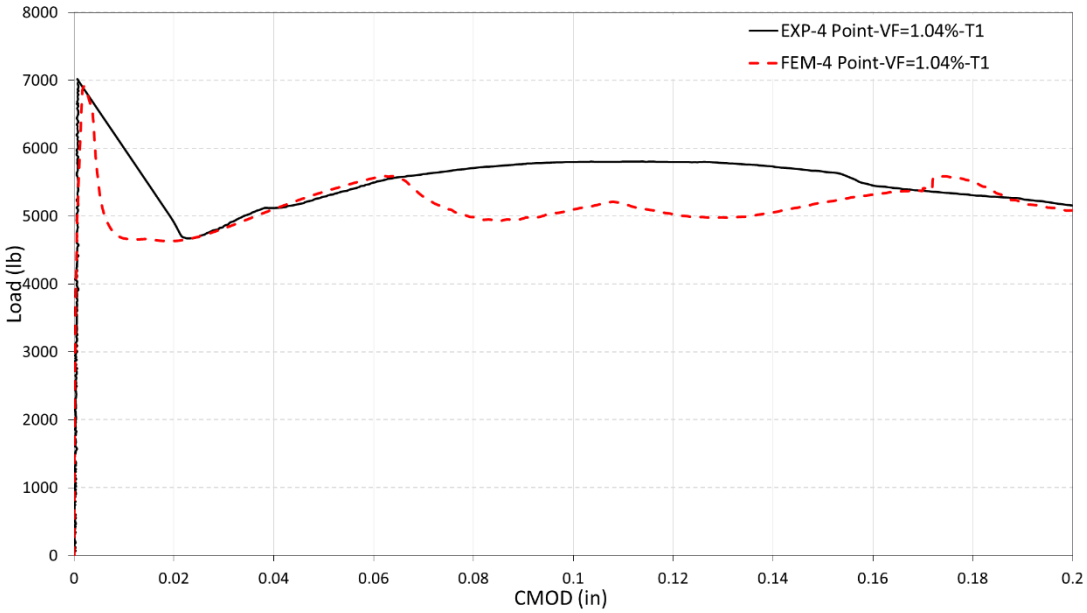

Figure 3-45 Experimental vs FEM Load-CMOD for 4-Point Bending – Synthetic FRC VF=1.04% - Test 1

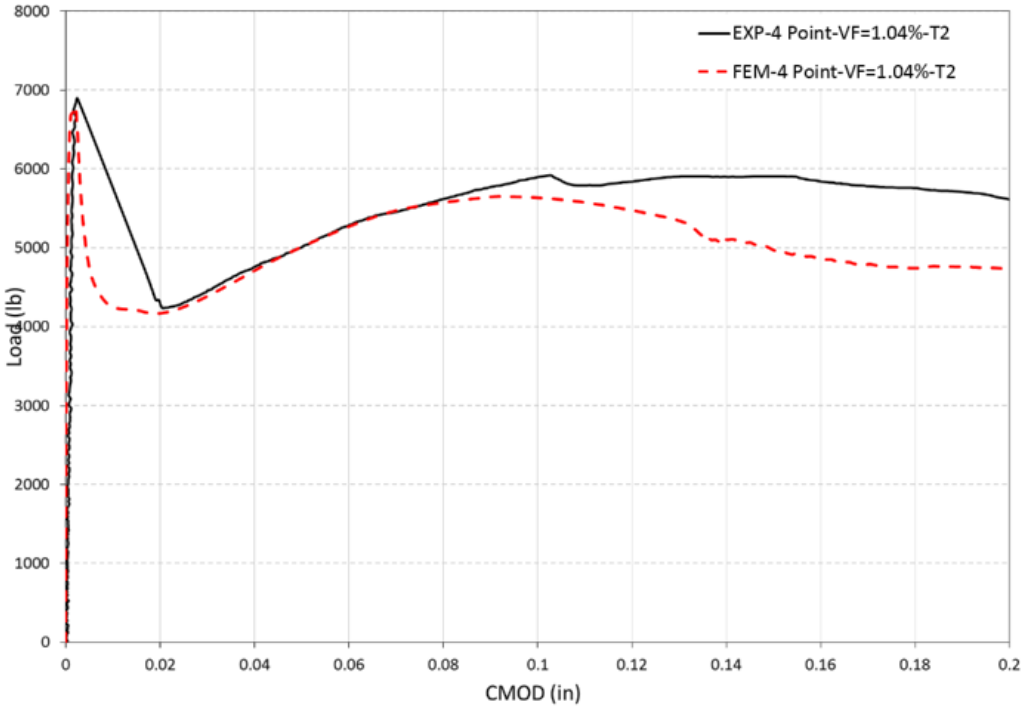

Figure 3-46 Experimental vs FEM Load-CMOD for 4-Point Bending – Synthetic FRC VF=1.04% - Test 2

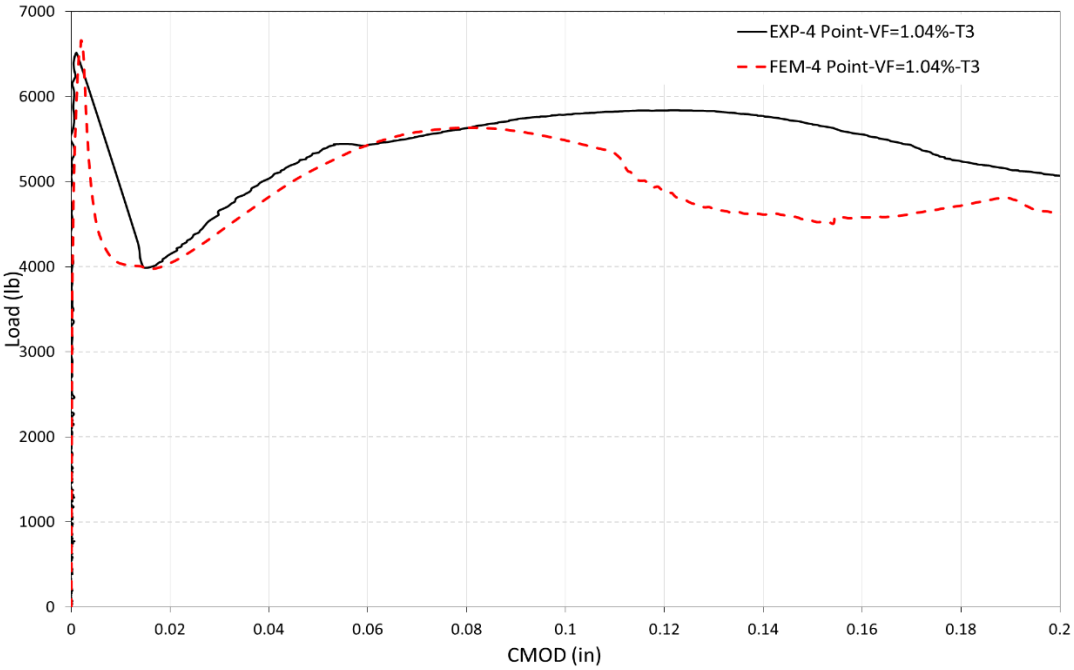

Figure 3-47 Experimental vs FEM Load-CMOD for 4-Point Bending – Synthetic FRC VF= 1.04% - Test 3

As presented in the Figures 3-42 to 3-47, the FEM load-CMOD results showed a very good agreement with the experimental results in case of 0.54% fiber volume fraction. For the case of 1.04% volume fraction, results were in good agreement with experimental data up to a CMOD value of 0.1in. The main difference of numerical and experimental results was in the area between the peak load and load drop, immediately after the crack. The same variation was observed in the load-deflection responses. As in the load-displacement response, the load-crack width data for this region was not recorded due to the sudden deformation imposed on the specimen immediately after the crack. This deformation happened in a fraction of a second, and the data accusation system used for the experimental study was not able to record the data. The FEM results in the case of the 4-point bending presented more variations in 1.04% fiber volume fraction compared to the experimental results. Overall, the FEM results, based on using the CDP model and the proposed softening law, were able to simulate the cracking behavior of synthetic FRC.

3.9 Fracture Energy evaluation

Hillerborg [103], based on the brittle fracture concepts, defined fracture energy as energy required to open a unit area of crack (Gf). This energy can be obtained as the area under the stress-crack width relationship. In the last section, the tension softening law was obtained through a fitting procedure for both notched beams under 3-point bending and unnotched beams under 4-point bending, with fiber volume fractions of 0.54% and 1.04%. Tables 3-4 and 3-5 present a summary of all the parameters obtained and the corresponding fracture energy criteria for cases of 3-point bending and 4-point bending, respectively. In order to be consistent with previous sections, the fracture energy was calculated up to a crack width of 0.2 inches.

Table 3-4 Tensile softening law parameter and fracture energy in case of notched beams under 3-point bending tests

VF (%) –Test#	f_1	f_2	α	f_3	f_4	d	w_1	w_2	c	$G_{f,cw=0.2\ in}$ (psi. in)	$Average\ G_{f,cw=0.2\ in}$ (psi. in)
0.54-T1	332.5	40	740	40	60	0.15	0.017	0.15	1	10.1	8.2
0.54-T2	332.5	30	740	30	40	0.13	0.017	0.147	2	6.56	
0.54-T3	332.5	40	740	40	50	0.1	0.017	0.117	1	7.95	
1.04-T1	359	50	800	50	74	0.185	0.017	0.202	3.5	13.21	14.4
1.04-T2	359	50	800	60	91	0.165	0.017	0.182	1	15.38	
1.04-T3	359	55	880	55	86	0.165	0.017	0.182	1	14.51	

Table 3-5 Tensile softening law parameter and fracture energy in case of beams under 4-point bending tests

VF (%)– Test#	f_1	f_2	α	f_3	f_4	d	w_1	w_2	c	$G_{f,cw=0.2\ in}$ (psi/in)	$Average\ G_{f,cw=0.2\ in}$ (psi. in)
4P-0.54-T1	180	15	500	19	20	0.039	0.039	0.078	5	1.1	5.4
4P-0.54-T2	201	47	700	50	51	0.09	0.025	0.115	2	9.95	
4P-0.54-T3	205	26	440	37	38	0.015	0.039	0.054	1	5.16	
4P-1.04-T1	183	87	878	87	106	0.1	0.022	0.122	1	16.9	16.05
4P-1.04-T2	186	78	881	78	105	0.1	0.019	0.119	0.5	16.05	
4P-1.04-T3	183	74	880	74	106	0.1	0.016	0.116	0.5	15.19	

Tables 3-4 and 3-5 show that dry-cast synthetic FRC with 1.04% fiber volume fraction has a higher average fracture energy than the 0.54% fiber percentage. In the case of notched beams under 3-point bending, the fracture energy increased by 76.6 %, as the fiber volume fraction increased from 0.54% to 1.04%. For the case of unnotched beams under 4-point bending, the fiber percentage of 1.04% presented a fracture energy of 2.97 times higher than 0.54% fiber volume fraction.

4 Conclusion

The scope of this study was to investigate the cracking behavior of dry-cast-synthetic-fiber-reinforced concrete by means of experimental and numerical methods. A total of 12 beams and 6 cylinders were casted, using two dosages of polypropylene synthetic fiber. Notched and unnotched beams with fiber fractions of 0.54 % (8.3 PCY) and 1.04% (16PCY) were tested under flexural loading, as recommended by ASTM C1609 [96] and RILEM 162-TDF [88]. The cracking profile, in terms of crack width and crack propagation, was obtained with the 2D digital image correlation technique. Two-dimensional digital image correlation provided the surface deformation field of the beam specimens during the test.

Numerical investigation was performed by obtaining a softening law in tension for synthetic FRC. Softening stress-crack width law was obtained through a numerical fitting procedure (inverse analysis) by assuming a piecewise function for post-cracking softening behavior in tension. Load-crack width responses were extracted from the FEM model based on the softening laws obtained in the inverse analysis section. Finally, the fraction energy of the synthetic FRC was calculated based on the obtained softening law in tension for every test and each fiber volume fraction under 3-point bending and 4-point bending. Based on the numerical and experimental tests performed in this study, the following conclusions can be made.

- The addition of synthetic fibers to the dry-cast concrete mixture increases the ductility and energy absorption of the synthetic FRC beams under flexural loading. Both fiber volume fractions presented a hardening stage after an initial drop in load capacity due to the crack initiation. Synthetic FRC with higher fiber volume fraction presented a smaller load capacity drop than the lower fiber volume fraction. This suggests the earlier interaction of fibers after the crack is initiated. The hardening state is due to the stitching effect of the fibers crossing the crack surface, known as fiber bridging. Load capacity undergoes a

softening phase after the peak in the hardening state is reached. Beams with the fiber volume fraction of 1.04% presented significantly higher post-cracking strength compared to those with a volume fraction of 0.54%. The softening stage of the load bearing under flexure was mainly due to the fiber pull out.

- A comparison of the classical crack width measurement technique and the 2D DIC method suggests a good compatibility between the results of both techniques. The two-dimensional DIC method can provide full field deformation with high accuracy, which can be used to investigate the cracking behavior of concrete materials.
- The DIC full field deformation analysis can provide the crack development and crack tip propagation. Both volume fractions of synthetic fibers presented crack control after the macro crack was initiated. In comparison, the 1.04% fiber volume fraction presented much better crack control and crack propagation. This behavior suggests that synthetic FRC with higher fiber volume faction has a smaller cracked section at any stage of the loading; therefore, it would have larger moment of inertia, which consequently provides more flexural strength.
- Load-crack width responses of the beams under flexural loading suggest that the required flexural loading for the same crack displacement is higher in the case of synthetic FRC with a high fiber dosage. This variation is more resonant in the case of unnotched beams under 4-point bending.
- The softening curve in tension was assumed as a piecewise function of crack displacement. Softening parameters were found by a numerical fitting procedure, using 3D nonlinear FEM and a concrete damage plasticity model. Softening curves were obtained for every specimen tested in this study. Finite element models were able to accurately follow the experimental load-deflection curve. Fitted load-deflection curves showed a significant agreement with experimental data in the elastic and hardening states of the curves for both

cases of beams under 3-point and 4-point bending. For large deflection values for the case of 4-point bending, models for the 1.04% volume fraction presented high sensitivity to the material parameters and tended to present multiple cracking behavior. Overall, they were in good agreement with the experimental results. The largest variation from the experimental results was observed in the region immediately after the first peak load and before the hardening state. Due to the lack of experimental data for this region, the numerical fitting procedure was not able to fully recalculate this region.

- Implementation of the suggested tensile-softening behavior, in terms of stress-crack width into 3D nonlinear FEM modeling based on the concrete damage plasticity, provided a good approximation of the synthetic FRC material behavior. Numerical crack width was calculated, considering the relative displacement of the nodes across the plastic strain band. This band was assumed to correspond to the crack surface. The FEM results were in good agreement with the experimental results of load-crack width for beams under 3-point and 4-point bending.
- Average fracture energy, calculated based on the softening stress-crack width relationship, suggests that increasing the volume fraction of fibers in dry-cast synthetic FRC increases the fracture energy. This increase in the fracture energy is significantly higher in the case of unnotched beams under 4-point bending.

5 References

[1] J. P. Romualdi and G. Batson, “Behavior of Reinforced Concrete Beams with Closely Spaced Reinforcement,” *ACI J. Proc.*, vol. 60, no. 6, pp. 775–789, 1963.

[2] S. P. S. and B. V. Rangan, “Fiber Reinforced Concrete Properties,” *J. Proc.*, vol. 68, no. 2.

[3] H. Falkner and V. Henke, “Application of steel fibre concrete for underwater concrete slabs,” *Cem. Concr. Compos.*, vol. 20, no. 5, pp. 377–385, 1998.

[4] A. Wilson and A. Abolmaali, “Performance of Steel Fiber-Reinforced Concrete Pipes,” *J. Pipeline Syst. Eng. Pract.*, vol. 5, no. 3, pp. 168–177, 2014.

[5] H. Dinh, G. J. Parra-Montesinos, M. ASCE, J. K. Wight, and ASCE, “Shear strength model for steel fiber reinforced concrete beams without stirrup reinforcement,” *J. Struct. …*, vol. 137, no. October, pp. 1039–1051, 2010.

[6] B. Mobasher and X. Destrée, “Design and construction aspects of steel fiber-reinforced concrete elevated slabs,” in *American Concrete Institute, ACI Special Publication*, 2010, no. 274 SP, pp. 95–107.

[7] J. Michels, D. Waldmann, S. Maas, and A. Zürbes, “Steel fibers as only reinforcement for flat slab construction – Experimental investigation and design,” *Constr. Build. Mater.*, vol. 26, no. 1, pp. 145–155, 2012.

[8] L. Gödde and P. Mark, “Umlagerungsverhalten von Plattentragwerken aus Stahlfaserbeton,” *Beton- und Stahlbetonbau*, vol. 106, no. 6, pp. 350–363, Jun. 2011.

[9] A. Wilson and A. Abolmaali, “Comparison of Material Behavior of Steel and Synthetic Fibers in Dry-Cast Application,” *Transp. Res. Rec. J. Transp. Res. Board*, vol. 2332, no. 1, pp. 23–28, 2013.

[10] A. Carpinteri and R. MassabÓ, “Continuous vs discontinuous bridged-crack model for fiber-reinforced materials in flexure,” *Int. J. Solids Struct.*, vol. 34, no. 18, pp. 2321–2338, 1997.

[11] A. Abrishambaf, J. A. O. Barros, and V. M. C. F. Cunha, “Tensile stress–crack width law for steel fibre reinforced self-compacting concrete obtained from indirect (splitting) tensile tests,” *Cem. Concr. Compos.*, vol. 57, pp. 153–165, 2015.

[12] R. de Montaignac, B. Massicotte, J.-P. Charron, and A. Nour, “Design of SFRC structural elements: post-cracking tensile strength measurement,” *Mater. Struct.*, vol. 45, no. 4, pp. 609–622, 2011.

[13] F. P. Zhou, “Some aspects of tensile fracture behaviour and structural response of cementitious materials.” ARRAY(0x8f9f018), p. 76, 1988.

[14] ASTM C496/C496M, “Standard Test Method for Splitting Tensile Strength of Cylindrical Concrete Specimens,” *Am. Soc. Test. Mater.*, pp. 1–5, 2011.

[15] B. I. G. Barr *et al.*, “Round-robin analysis of the RILEM TC 162-TDF beam-bending test: Part 2—Approximation of δ from the CMOD response,” *Mater. Struct.*, vol. 36, no. 9, pp. 621–630, 2003.

[16] B. I. G. Barr *et al.*, “Round-robin analysis of the RILEM TC 162-TDF beam-bending test: Part 1---Test method evaluation,” *Mater. Struct.*, vol. 36, no. 9, pp. 609–620, 2003.

[17] B. I. G. Barr *et al.*, “Round-robin analysis of the RILEM TC 162-TDF beam-bending test: Part 3—Fibre distribution,” *Mater. Struct.*, vol. 36, no. 9, pp. 631–635, 2003.

[18] B. Statements and B. Statements, “Flexural Toughness of Fiber Reinforced Concrete (Using Centrally Loaded Round Panel) 1,” *Annu. B. ASTM Stand.*, vol. 4, no. May, pp. 1–9, 2003.

[19] S. H. Kwon, Z. Zhao, and S. P. Shah, “Effect of specimen size on fracture energy and softening curve of concrete: Part II. Inverse analysis and softening curve,” *Cem. Concr. Res.*, vol. 38, no. 8, pp. 1061–1069, 2008.

[20] J. A. O. Barros, V. M. C. F. Cunha, A. F. Ribeiro, and J. A. B. Antunes, “Post-cracking behaviour of steel fibre reinforced concrete,” *Mater. Struct.*, vol. 38, no. 1, pp. 47–56, 2005.

[21] P. Rossi, “Mechanical behaviour of metal-fibre reinforced concretes,” *Cem. Concr. Compos.*, vol. 14, no. 1, pp. 3–16, 1992.

[22] D. Soulioti, N. M. Barkoula, A. Paipetis, T. E. Matikas, T. Shiotani, and D. G. Aggelis, “Acoustic emission behavior of steel fibre reinforced concrete under bending,” *Constr. Build. Mater.*, vol. 23, no. 12, pp. 3532–3536, 2009.

[23] D. V. Soulioti, N. M. Barkoula, A. Paipetis, and T. E. Matikas, “Effects of fibre geometry and volume fraction on the flexural behaviour of steel-fibre reinforced concrete,” *Strain*, vol. 47, no. SUPPL. 1, pp. 535–541, 2011.

[24] F. Bencardino, L. Rizzuti, G. Spadea, and R. N. Swamy, “Experimental evaluation of fiber reinforced concrete fracture properties,” *Compos. Part B Eng.*, vol. 41, no. 1, pp. 17–24, 2010.

[25] H. Krenchel, “Fibre reinforcement; theoretical and practical investigations of the elasticity and strength of fibre-reinforced materials,” Technical University of Denmark, 1964.

[26] J. Michels, R. Christen, and D. Waldmann, “Experimental and numerical investigation on postcracking behavior of steel fiber reinforced concrete,” *Eng. Fract. Mech.*, vol. 98, pp. 326–349, 2013.

[27] S. Y. Alam, J. Saliba, and A. Loukili, “Study of evolution of fracture process zone in concrete by simultaneous application of digital image correlation and acoustic emission,” *VIII Int. Conf. Fract. Mech. Concr. Concr. Struct.*, no. FraMCoS-8, pp. 1–9, 2012.

[28] N. McCormick and J. Lord, “Digital image correlation for structural measurements,” *Proc. Inst. Civ. Eng. - Civ. Eng.*, vol. 165, no. 4, pp. 185–190, 2012.

[29] B. Pan, K. Qian, H. Xie, and A. Asundi, “Two-dimensional digital image correlation for in-plane displacement and strain measurement: a review,” *Meas. Sci. Technol.*, vol. 20, no. 6, p. 62001, 2009.

[30] A. M. Alhozaimy, P. Soroushian, and F. Mirza, “Mechanical properties of polypropylene

fiber reinforced concrete and the effects of pozzolanic materials," *Cem. Concr. Compos.*, vol. 18, no. 2, pp. 85–92, 1996.

[31] P. S. Song, S. Hwang, and B. C. Sheu, "Strength properties of nylon- and polypropylene-fiber-reinforced concretes," *Cem. Concr. Res.*, vol. 35, no. 8, pp. 1546–1550, 2005.

[32] S. Kurtz and P. Balaguru, "Postcrack creep of polymeric fiber-reinforced concrete in flexure," *Cem. Concr. Res.*, vol. 30, no. 2, pp. 183–190, 2000.

[33] K. Ari, O. Karahan, C. D. Atis, C. Bilim, and Ö. C. Sola, "Relation between Strength Properties (Flexural and Compressive) and Abrasion Resistance of Fiber (Steel and Polypropylene)-Reinforced Fly Ash Concrete," Aug. 2009.

[34] J. R. Roesler, D. a. Lange, S. a. Altoubat, K.-A. Rieder, and G. R. Ulreich, "Fracture of Plain and Fiber-Reinforced Concrete Slabs under Monotonic Loading," *J. Mater. Civ. Eng.*, vol. 16, no. 5, pp. 452–460, 2004.

[35] N. Van Chanh, "Steel fiber reinforced concrete," *Construction*, vol. 25, no. 1, pp. 108–116, 2004.

[36] A. Birgitta and E. Klausen, *Steel fibres in load – carrying con- crete structures . Guideline survey and practical examples*. 2009.

[37] A. M. Olimb, "Testing of Fibre Reinforced Concrete Structures Ane Marte Olimb," 2012.

[38] I. Löfgren, "Fibre-reinforced Concrete for Industrial Construction--a fracture mechanics approach to material testing and structural analysis," 2005.

[39] H. Tlemat, K. Pilakoutas, and K. Neocleous, "Modelling of SFRC using inverse finite element analysis," *Mater. Struct.*, vol. 39, no. May 2005, pp. 221–233, 2006.

[40] Y. Seo, Y. Kim, M. Witczak, and R. Bonaquist, "Application of Digital Image Correlation Method to Mechanical Testing of Asphalt-Aggregate Mixtures," *Transp. Res. Rec. J. Transp. Res. Board*, vol. 1789, pp. 162–172, Jan. 2002.

[41] A. Rechenmacher and R. Finno, "Digital Image Correlation to Evaluate Shear Banding in Dilative Sands BT - Digital Image Correlation to Evaluate Shear Banding in Dilative Sands," 2004.

[42] Y. Seo, G. R. Chehab, and Y. R. Kim, "Viscoelastoplastic Damage Characterization of Asphalt–Aggregate Mixtures Using Digital Image Correlation," Mar. 2007.

[43] S. Choi and S. P. Shah, "Measurement of deformations on concrete subjected to compression using image correlation," *Exp. Mech.*, vol. 37, no. 3, pp. 307–313, 1997.

[44] B. Wattrisse, A. Chrysochoos, J.-M. Muracciole, and M. Némoz-Gaillard, "Analysis of strain localization during tensile tests by digital image correlation," *Exp. Mech.*, vol. 41, no. 1, pp. 29–39, 2001.

[45] D. Corr, M. Accardi, L. Graham-Brady, and S. Shah, "Digital image correlation analysis of interfacial debonding properties and fracture behavior in concrete," *Eng. Fract. Mech.*, vol. 74, no. 1, pp. 109–121, 2007.

[46] S. Yoneyama, Y. Morimoto, and M. Takashi, "Automatic Evaluation of Mixed-mode Stress

Intensity Factors Utilizing Digital Image Correlation," *Strain*, vol. 42, no. 1, pp. 21–29, Feb. 2006.

[47] J. Kozicki and J. Tejchman, "Experimental Investigations of Strain Localization in Concrete using Digital Image Correlation (DIC) Technique," *Arch. Hydro-Engineering Enviromental Mech.*, vol. 54, no. 1, pp. 3–24, 2007.

[48] Ł. Skarżyński, E. Syroka, and J. Tejchman, "Measurements and Calculations of the Width of the Fracture Process Zones on the Surface of Notched Concrete Beams," *Strain*, vol. 47, pp. e319–e332, Jun. 2011.

[49] Z. Wu, H. Rong, J. Zheng, F. Xu, and W. Dong, "An experimental investigation on the FPZ properties in concrete using digital image correlation technique," *Eng. Fract. Mech.*, vol. 78, no. 17, pp. 2978–2990, 2011.

[50] B. Wan, M. A. Sutton, M. F. Petrou, K. A. Harries, and N. Li, "Investigation of Bond between Fiber Reinforced Polymer and Concrete Undergoing Global Mixed Mode I/II Loading," *J. Eng. Mech.*, vol. 130, no. 12, pp. 1467–1475, 2004.

[51] Y. H. Huang, L. Liu, F. C. Sham, Y. S. Chan, and S. P. Ng, "Optical strain gauge vs. traditional strain gauges for concrete elasticity modulus determination," *Opt. - Int. J. Light Electron Opt.*, vol. 121, no. 18, pp. 1635–1641, 2010.

[52] T. M. Fayyad and J. M. Lees, "Application of Digital Image Correlation to Reinforced Concrete Fracture," *Procedia Mater. Sci.*, vol. 3, pp. 1585–1590, 2014.

[53] J.-F. Destrebecq, E. Toussaint, and E. Ferrier, "Analysis of Cracks and Deformations in a Full Scale Reinforced Concrete Beam Using a Digital Image Correlation Technique," *Exp. Mech.*, vol. 51, no. 6, pp. 879–890, 2011.

[54] M. D. C. Ferreira, W. S. Venturini, and F. Hild, "On the analysis of notched concrete beams: From measurement with digital image correlation to identification with boundary element method of a cohesive model," *Eng. Fract. Mech.*, vol. 78, no. 1, pp. 71–84, 2011.

[55] Rastogi, *Photomechanics*, vol. 77. 2000.

[56] J. S. Sirkis and T. J. Lim, "Displacement and strain measurement with automated grid methods," *Exp. Mech.*, vol. 31, no. 4, pp. 382–388, 1991.

[57] H. T. Goldrein, S. J. P. Palmer, and J. M. Huntley, "Automated fine grid technique for measurement of large-strain deformation maps," *Opt. Lasers Eng.*, vol. 23, no. 5, pp. 305–318, 1995.

[58] W. H. Peters and W. F. Ranson, "Digital imaging techniques in experimental stress analysis," *Opt. Eng.*, vol. 21, no. 3, pp. 427–431, 1982.

[59] T. C. Chu, W. F. Ranson, M. A. Sutton, and W. H. Peters, "Applications of Digital-Image Correlation techniques to experimental mechanics," *Exp. Mech.*, vol. 25, no. 3, pp. 232–244, 1985.

[60] W. H. Peters, W. F. Ransom, M. A. Sutton, T. C. Chu, and J. Anderson, "Application of digital correlation methods to rigid body mechanics," *Opt. Eng.*, vol. 22, no. 6, pp. 738–742, 1983.

[61] M. Sutton, C. Mingqi, W. Peters, Y. Chao, and S. McNeill, “Application of an optimized digital correlation method to planar deformation analysis,” *Image Vis. Comput.*, vol. 4, no. 3, pp. 143–150, 1986.

[62] P. F. Luo, Y. J. Chao, M. A. Sutton, and W. H. Peters, “Accurate measurement of three-dimensional deformations in deformable and rigid bodies using computer vision,” *Exp. Mech.*, vol. 33, no. 2, pp. 123–132, 1993.

[63] J. D. Helm, S. R. McNeill, and M. A. Sutton, “Improved three-dimensional image correlation for surface displacement measurement,” *Opt. Eng.*, vol. 35, no. 7, pp. 1911–1920, 1996.

[64] D. Garcia, J. . Orteu, and L. Penazzi, “A combined temporal tracking and stereo-correlation technique for accurate measurement of 3D displacements: application to sheet metal forming,” *J. Mater. Process. Technol.*, vol. 125, pp. 736–742, 2002.

[65] B. Pan, H. Xie, L. Yang, and Z. Wang, “Accurate Measurement of Satellite Antenna Surface Using 3D Digital Image Correlation Technique,” *Strain*, vol. 45, no. 2, pp. 194–200, 2009.

[66] D. J. Chen, F. P. Chiang, Y. S. Tan, and H. S. Don, “Digital speckle-displacement measurement using a complex spectrum method,” *Appl. Opt.*, vol. 32, no. 11, pp. 1839–1849, Apr. 1993.

[67] M. Sjödahl and L. R. Benckert, “Electronic speckle photography: analysis of an algorithm giving the displacement with subpixel accuracy,” *Appl. Opt.*, vol. 32, no. 13, pp. 2278–2284, May 1993.

[68] M. Sjödahl, “Electronic speckle photography: increased accuracy by nonintegral pixel shifting,” *Appl. Opt.*, vol. 33, no. 28, pp. 6667–6673, Oct. 1994.

[69] I. Yamaguchi, “Speckle Displacement and Decorrelation in the Diffraction and Image Fields for Small Object Deformation,” *Opt. Acta Int. J. Opt.*, vol. 28, no. 10, pp. 1359–1376, Oct. 1981.

[70] J. Brillaud and F. Lagattu, “Limits and possibilities of laser speckle and white-light image-correlation methods: theory and experiments,” *Appl. Opt.*, vol. 41, no. 31, pp. 6603–6613, Nov. 2002.

[71] L. Felipe-Sesé, P. Siegmann, F. A. Díaz, and E. A. Patterson, “Integrating fringe projection and digital image correlation for high-quality measurements of shape changes,” *Opt. Eng.*, vol. 53, no. 4, p. 44106, 2014.

[72] Z. Sun, J. S. Lyons, and S. R. McNeill, “Measuring Microscopic Deformations with Digital Image Correlation,” *Opt. Lasers Eng.*, vol. 27, no. 4, pp. 409–428, 1997.

[73] M. C. Pitter, C. W. See, J. Y. L. Goh, and M. G. Somekh, “Focus errors and their correction in microscopic deformation analysis using correlation,” *Opt. Express*, vol. 10, no. 23, pp. 1361–1367, Nov. 2002.

[74] D. Zhang, M. Luo, and D. D. Arola, “Displacement/strain measurements using an optical microscope and digital image correlation,” *Opt. Eng.*, vol. 45, no. 3, p. 33605, 2006.

[75] T. A. Berfield, J. K. Patel, R. G. Shimmin, P. V Braun, J. Lambros, and N. R. Sottos, “Fluorescent Image Correlation for Nanoscale Deformation Measurements,” *Small*, vol. 2,

no. 5, pp. 631–635, 2006.

[76] C. Franck, S. Hong, S. A. Maskarinec, D. A. Tirrell, and G. Ravichandran, “Three-dimensional Full-field Measurements of Large Deformations in Soft Materials Using Confocal Microscopy and Digital Volume Correlation,” *Exp. Mech.*, vol. 47, no. 3, pp. 427–438, 2007.

[77] N. Sabaté *et al.*, “Measurement of residual stresses in micromachined structures in a microregion,” *Appl. Phys. Lett.*, vol. 88, no. 7, p. 71910, Feb. 2006.

[78] J. Keller *et al.*, “FibDAC - Residual Stress Determination by Combination of Focused Ion Beam Technique and Digital Image Correlation ,” *Mater. Sci. Forum*, vol. 524–525, pp. 121–126, 2006.

[79] I. Chasiotis and W. G. Knauss, “A new microtensile tester for the study of MEMS materials with the aid of atomic force microscopy,” *Exp. Mech.*, vol. 42, no. 1, pp. 51–57, 2002.

[80] W. G. Knauss, I. Chasiotis, and Y. Huang, “Mechanical measurements at the micron and nanometer scales,” *Mech. Mater.*, vol. 35, no. 3–6, pp. 217–231, 2003.

[81] G. Vendroux and W. G. Knauss, “Submicron deformation field measurements: Part 1. Developing a digital scanning tunneling microscope,” *Exp. Mech.*, vol. 38, no. 1, pp. 18–23, 1998.

[82] G. Vendroux and W. G. Knauss, “Submicron deformation field measurements: Part 2. Improved digital image correlation,” *Exp. Mech.*, vol. 38, no. 2, pp. 86–92, 1998.

[83] G. Vendnroux, N. Schmidt, and W. G. Knauss, “Submicron deformation field measurements: Part 3. Demonstration of deformation determinations,” *Exp. Mech.*, vol. 38, no. 3, pp. 154–160, 1998.

[84] H. W. Schreier and M. A. Sutton, “Systematic errors in digital image correlation due to undermatched subset shape functions,” *Exp. Mech.*, vol. 42, no. 3, pp. 303–310, 2002.

[85] H. Lu and P. D. Cary, “Deformation measurements by digital image correlation: Implementation of a second-order displacement gradient,” *Exp. Mech.*, vol. 40, no. 4, pp. 393–400, 2000.

[86] A. Giachetti, “Matching techniques to compute image motion,” *Image Vis. Comput.*, vol. 18, no. 3, pp. 247–260, 2000.

[87] M. Sutton, S. McNeill, J. Helm, and Y. J. Chao, “Advances in two-dimensional and three-dimensional computer vision,” *Photomechanics*, vol. 372, pp. 323–372, 2000.

[88] RILEM TC 162-TDF, “Final recommendation of RILEM TC 162-TDF: Test and design methods for steel fibre reinforced concrete sigma-epsilon-design method,” *Mater. Struct.*, vol. 36, no. 262, pp. 560–567, 2003.

[89] RILEM TC 162-TDF, “Recommendations of RILEM TC 162-TDF: Test and design methods for steel fibre reinforced concrete: bending test,” *Mater. Struct.*, vol. 35, no. 253, pp. 579–582, 2002.

[90] B. I. G. Barr and M. K. Lee, “Interpretation in the procedure of calculating RILEMTC- 162 beam design Parameters. Definition of round robin test, preparation of specimens, execution

and evaluation of round Robin testing. Report of subtasks 2.1 and 2.2,Brite-Euram project BRPR-CT98-081," 2002.

[91] H. Tlemat, K. Pilakoutas, and K. Neocleous, "Stress-strain characteristic of SFRC using recycled fibres," *Mater. Struct.*, vol. 39, no. 3, pp. 365–377, 2006.

[92] O. Hemmy, "Recommendations for finite element analysis of FRC`, report of subtask 3.5, Brite-EuRam Project BRPR-CT98-0813: Test and design methods for steel fibre reinforced concrete, project funded by the European Community under the Industrial & Materials Technolo," 2002.

[93] D. Dupont and L. Vandewalle, "Recommendations for finite element analysis of FRC. Report of subtask 3.5, Brite-EuRam Project BRPR-CT98-0813: Test and design methods for steel fibre reinforced concrete, project funded by the European Community under the Industrial & Materials Technolog," 2002.

[94] L. Ostergaard, J. Olesen, H. Stang, and D. Lange, "A method for fast and simple interpretation and inverse analysis of the wedge splitting test. Report of subtask 3.5, Brite-EuRam Project BRPR-CT98-0813: Test and design methods for steel fibre reinforced concrete, project funded by the European Community ," 2002.

[95] H. Stang, "Finite element modelling using discrete crack elements. Report of subtask 3.5, Brite-EuRam Project BRPR-CT98-0813: Test and design methods for steel fibre reinforced concrete, project funded by the European Community under the Industrial & Materials Techn," 2002.

[96] C. C. Test, T. Drilled, C. Concrete, and S. T. Panels, "C 1609/C 1609M-05 Standard Test Method for Flexural Performance of Fiber-Reinforced Concrete (Using Beam With Third-Point Loading) 1," *Astm*, vol. i, no. C 1609/C 1609M-05, pp. 1–8, 2005.

[97] R. Concrete *et al.*, "C 1116/C 1116M-09 Standard specification for Fiber-Reinforced Concrete 1," *Astm*, vol. i, no. Reapproved, pp. 1–7, 2009.

[98] "MasterFiber MAC Matrix," *BASF the Chemical Company*, 2012. .

[99] ASTM C39, "Standard Test Method for Compressive Strength of Cylindrical Concrete Specimens," *Am. Soc. Test. Mater.*, pp. 1–7, 2016.

[100] C. C. Test, T. Drilled, and C. Concrete, "Standard Test Method for Flexural Strength of Concrete (Using Simple Beam with Third-Point Loading) 1," *Hand*, vol. C78-2, no. C, pp. 1–4, 2010.

[101] "GOM Correlate user manual v6." GOM mbH, Germany, 2016.

[102] P. Vacher, S. Dumoulin, F. Morestin, and S. Mguil-Touchal, "Bidimensional strain measurement using digital images," *Proc. Inst. Mech. Eng. Part C J. Mech. Eng. Sci.*, vol. 213, no. 8, pp. 811–817, 1999.

[103] A. Hillerborg, M. Modéer, and P.-E. Petersson, "Analysis of crack formation and crack growth in concrete by means of fracture mechanics and finite elements," *Cem. Concr. Res.*, vol. 6, no. 6, pp. 773–781, 1976.

[104] A. Hillerborg, "The theoretical basis of a method to determine the fracture energy GF of concrete," *Mater. Struct.*, vol. 18, no. 106, pp. 291–296, 1985.

[105] Y. R. Rashid, “Ultimate strength analysis of prestressed concrete pressure vessels,” *Nucl. Eng. Des.*, vol. 7, no. 4, pp. 334–344, 1968.

[106] J. F. Chen and Y. Tao, “Finite Element Modelling of FRP-to-Concrete Bond Behaviour Using the Concrete Damage Plasticity Theory Combined with a Plastic Degradation Model,” in *Advances in FRP Composites in Civil Engineering: Proceedings of the 5th International Conference on FRP Composites in Civil Engineering (CICE 2010), Sep 27--29, 2010, Beijing, China*, L. Ye, P. Feng, and Q. Yue, Eds. Berlin, Heidelberg: Springer Berlin Heidelberg, 2011, pp. 45–50.

[107] A. S. Genikomsou and M. A. Polak, “Finite element analysis of punching shear of concrete slabs using damaged plasticity model in ABAQUS,” *Eng. Struct.*, vol. 98, pp. 38–48, 2015.

[108] “ABAQUS Analysis user’s manual 6.14-EF.” Dassault Systems Simulia Corp, Providence, RI, USA, 2014.

[109] T. Ahn, “Thermal and Mechanical Studies of Thin Spray-On Liner (TSL) for Concrete Tunnel Linings,” 2011.

[110] J. Lubliner, J. Oliver, S. Oller, and E. Oñate, “A plastic-damage model for concrete,” *Int. J. Solids Struct.*, vol. 25, no. 3, pp. 299–326, 1989.

[111] J. Lee and G. L. Fenves, “Plastic-Damage Model for Cyclic Loading of Concrete Structures,” Aug. 1998.

[112] J. Y. Wu, J. Li, and R. Faria, “An energy release rate-based plastic-damage model for concrete,” *Int. J. Solids Struct.*, vol. 43, no. 3, pp. 583–612, 2006.

[113] G. Voyiadjis and Z. Taqieddin, “Elastic Plastic and Damage Model for Concrete Materials: Part I-Theoretical Formulation,” *Int. J. Struct. Chang. Solids*, vol. 1, no. 1, pp. 31–59, 2009.

[114] T. Jankowiak and T. Lodygowski, “Identification of parameters of concrete damage plasticity constitutive model,” *Found. Civ. Environ. …*, no. 6, pp. 53–69, 2005.

[115] J. Noël, S. Datoussaïd, and F. Dagrain, “Potential interest of the Barcelona Model for predicting the efficiency of a tool set configuration in geo-material cutting,” in *9th National Congress on Theoretical and Applied Mechanics*, 2012, no. May, pp. 9–10.

[116] M. Blazejowski, “Flexural Behaviour of Steel Fibre Reinforced Concrete Tunnel Linings,” 2012.

[117] S.-T. Kang, Y. Lee, Y.-D. Park, and J.-K. Kim, “Tensile fracture properties of an Ultra High Performance Fiber Reinforced Concrete (UHPFRC) with steel fiber,” *Compos. Struct.*, vol. 92, no. 1, pp. 61–71, 2010.

6 Biographical Information

Sina Abhaee graduated from the Baha'i Institute for Higher Education (BIHE), Tehran, in the fall of 2012, receiving a Bachelor of Science degree in Civil Engineering. In spring 2015, he moved to Texas to pursue a master's degree in civil engineering, with an emphasis in structural and applied mechanics, at the University of Texas at Arlington. He worked under the supervision of Dr. Ali Abolmaali. While pursuing his master's degree, he focused his studies on image-processing-based crack measurement and finite element analysis of synthetic-fiber-reinforced concrete. His research interests include fracture mechanics, finite element analysis, and image processing methods.